POLITECNICO DI TORINO

Master of Science in Mechanical Engineering

Masters's Thesis

Roving hammer EMA on electric powertrain for FE model validation

Supervisor:

Prof. Enrico Galvagno

Cosupervisors:

Prof. Marchesiello Stefano

Andi Coba

Candidate:

Ali Bahmani

Academic Year 2025-2026

Table of Contents

Tables and Figures

Declaration on the Use of Artificial Intelligence Tools

Artificial intelligence tools, including ChatGPT, were used only as supportive tools during the preparation of this thesis, mainly for language revision, improvement of clarity and structure, organization of explanations, and support in formatting or checking MATLAB-related descriptions. The experimental work, data processing, interpretation of results, numerical comparisons, figures, tables, conclusions, and final validation decisions were carried out, reviewed, and approved by the author. No experimental results, numerical results, scientific conclusions, or references were fabricated using artificial intelligence tools. The author takes full responsibility for the originality, accuracy, and integrity of the thesis.

1 Abstract

The dynamic behaviour of electric powertrains is a critical aspect of modern electric-vehicle development, especially from the perspective of Noise, Vibration and Harshness (NVH). Compared with conventional internal-combustion powertrains, electric powertrains are characterized by different excitation mechanisms, reduced masking noise, and higher sensitivity of the vehicle occupants to tonal and structural vibration phenomena. For this reason, reliable numerical models are required to predict the modal behaviour of the assembly and to support design decisions during the development process. However, a numerical model can only be considered predictive if its modal properties are validated against experimental evidence.

The objective of this thesis is to develop, validate, and apply an Experimental Modal Analysis (EMA) procedure based on roving-hammer impact testing for the modal characterization of an electric powertrain. The experimental activity is performed using an instrumented impact hammer, tri-axial accelerometers, a multi-channel acquisition system, and Simcenter Testlab software. The measured force and acceleration signals are processed to obtain Frequency Response Functions (FRFs), from which the main modal parameters are extracted: natural frequencies, damping factors, and mode shapes. The experimental results are then compared with the modal properties predicted by the available numerical model.

The work is organized in two main stages. First, the complete experimental and post-processing workflow is developed and validated on a cantilever beam. This preliminary test case provides a controlled structure with interpretable bending and torsional behaviour, allowing the acquisition setup, roving-hammer strategy, modal identification process, MATLAB post-processing routines, and FE-correlation tools to be verified. The beam study also highlights important experimental effects such as accelerometer mass loading, boundary-condition flexibility, damping estimation, and mode-shape correlation.

After this methodological validation, the same workflow is applied to the electric powertrain. Measurement nodes are defined on the mounting arms and on the powertrain body. The

powertrain is excited at selected locations and directions, while the dynamic response is measured by accelerometers installed at reference points. The experimental mode shapes and natural frequencies are compared with those obtained from the numerical model, with particular attention to the influence of mount stiffness, boundary conditions, mass distribution, and local structural flexibility.

The final outcome of the thesis is a structured experimental-numerical validation procedure for an electric powertrain. The results provide a basis for interpreting the physical origin of the identified modes and for defining possible model-updating actions aimed at improving the correlation between experimental measurements and numerical predictions.

2 Nomenclature

Symbol / acronym	Meaning
ω	angular frequency
ω_r	natural angular frequency of mode r
f_r	natural frequency of mode r
ζ_r	damping ratio of mode r
ϕ_r	mode shape vector of mode r
$[M]$	mass matrix
$[C]$	damping matrix
$[K]$	stiffness matrix
$[H(\omega)]$	Frequency Response Function matrix
$H_{ij}(\omega)$	FRF between response coordinate i and excitation coordinate j
α	mass-proportional Rayleigh damping coefficient
β	stiffness-proportional Rayleigh damping coefficient
DOF	Degree of Freedom
EMA	Experimental Modal Analysis
FE / FEM	Finite Element / Finite Element Method
FRF	Frequency Response Function
ICP	Integrated Circuit Piezoelectric
MAC	Modal Assurance Criterion
Auto-MAC	MAC matrix computed between modes of the same dataset
Cross-MAC	MAC matrix computed between experimental and numerical mode shapes
NVH	Noise, Vibration and Harshness
PSD	Power Spectral Density
SCADAS	Siemens data acquisition hardware family used for physical testing
SNR	Signal-to-Noise Ratio

3 Introduction

3.1 Background and motivation

The development of electric vehicles has increased the importance of accurate dynamic modelling and experimental validation of electric powertrain assemblies. In conventional vehicles, the internal-combustion engine is usually the dominant source of noise and vibration, and its broadband acoustic contribution can partially mask other structural and tonal phenomena. In electric vehicles, this masking effect is strongly reduced. As a consequence, vibration and noise contributions that were previously less perceptible can become more critical for passenger comfort. These include electric-machine tonal excitations, gear-mesh orders, inverter-related effects, bearing dynamics, structural resonances, and vibrations transmitted through the powertrain mounting system. This change from traditional to electrified powertrains has made NVH analysis more challenging and more important in the development of modern vehicles [1–3].

Recent studies on battery electric vehicle NVH show that the absence of combustion-engine masking noise exposes noise and vibration phenomena that were previously less evident in conventional vehicles. Hua et al. reviewed theoretical, computational, and experimental work on BEV NVH and highlighted the increasing importance of powertrain, tire, wind, and ancillary-system noise in electric vehicles [1]. Horváth and Zelei discussed the specific NVH challenges associated with EV powertrains, including electric motors, inverters, and gear systems, and emphasized the need for simulation-based approaches to manage these effects [2]. More generally, recent vehicle-NVH reviews confirm that the transition toward electrified and hybrid vehicles requires improved modelling and validation methods because the dominant excitation sources and passenger perception conditions are changing [3].

For this reason, NVH analysis has become a central aspect of electric powertrain development. The dynamic behaviour of an electric powertrain depends on several coupled elements: the motor and gearbox housing, bearings, mounting arms, bolted interfaces, rubber mounts, support brackets, and the boundary conditions imposed by the vehicle or by the test bench. These elements define the mass, stiffness, damping, and vibration-transmission paths of the complete assembly. Even small uncertainties in mount stiffness, joint stiffness, local component flexibility, or boundary-condition representation can significantly modify the predicted natural frequencies and mode shapes.

In the current state of the art, numerical simulation is widely used to predict the dynamic behaviour of powertrain systems before or during physical testing. Finite element models, multi-body models, and dedicated powertrain simulation tools can be used to estimate natural frequencies, mode shapes, forced response, and possible resonance problems. Holehouse et al. presented an integrated NVH approach for electro-mechanical rotating systems, showing the importance of considering the complete system response in electric driveline applications [4]. In the present thesis, the numerical reference is provided by a Romax model of the electric powertrain. Such a model is useful because it allows the dynamic behaviour of the assembly to be studied and modified virtually. However, the reliability of any numerical model depends on the assumptions used to describe geometry, material properties, mass distribution, joint stiffness, rubber mounts, bearing supports, and boundary conditions.

Therefore, simulation alone is not sufficient for reliable NVH assessment. Experimental validation is required to verify whether the numerical model reproduces the actual dynamic behaviour of the physical system. A numerical mode can only be considered reliable if it is consistent with the corresponding experimental mode in terms of both natural frequency and deformation shape. Frequency comparison alone is not enough, because two modes may appear in a similar frequency range while representing different physical motion. For this reason, validation procedures combine frequency-error analysis with mode-shape comparison methods such as the Modal Assurance Criterion [5–7].

Experimental Modal Analysis is one of the main experimental techniques used for structural dynamic identification and model validation. In EMA, a known input force is applied to the structure and the corresponding vibration response is measured. The ratio between output response and input force gives the Frequency Response Function, from which natural frequencies, damping ratios, and mode shapes can be extracted. Impact testing with an instrumented hammer is particularly suitable when several excitation points must be measured efficiently. In the roving-hammer configuration, the accelerometers remain fixed while the hammer is moved over the selected excitation points. This approach is useful for complex systems because it keeps the sensor mass distribution constant during the test and allows many input coordinates to be acquired with a limited number of accelerometers [5].

After the FRFs are measured, modal parameters must be extracted using a suitable identification method. In industrial modal testing, PolyMAX is widely used because it provides stabilization diagrams that help distinguish physical modes from computational or noise-related poles. Peeters et al. presented the PolyMAX frequency-domain method as an important modal parameter estimation approach for experimental modal analysis [8]. In the present thesis, PolyMAX is used in Simcenter Testlab to identify natural frequencies, damping ratios, and mode shapes from the measured FRFs.

The correlation between experimental and numerical models is especially important for vehicle structures, powertrain mounting systems, and mounting brackets because these components strongly affect vibration transmission paths. Oktav applied experimental and numerical modal analysis to a passenger vehicle and used modal correlation to compare structural dynamic behaviour [9]. Zhao et al. presented a simulation and experimental validation approach for a powertrain mounting bracket design, showing the relevance of modal behaviour in mount-system design [10]. Li et al. also showed that natural frequencies of powertrain mount brackets have a strong influence on NVH performance and proposed finite element model refinement to reduce discrepancies between measured and calculated natural frequencies [11]. These studies confirm that powertrain-related structures require both simulation and experimental validation, especially when mount stiffness, bracket flexibility, and boundary conditions influence the dynamic response.

Before applying this procedure to a complex industrial assembly, the methodology must be checked on a simpler and more interpretable structure. For this reason, the present thesis starts from a cantilever beam. The beam provides a controlled benchmark where the experimental setup, hammer excitation, sensor placement, Testlab workflow, PolyMAX modal identification, MATLAB post-processing, FRF synthesis, reciprocity verification, and MAC-based correlation can be developed and verified. This preliminary step is important because it confirms that the measurement chain and post-processing tools are reliable before they are applied to the electric powertrain.

After this methodological validation, the same experimental-numerical workflow is transferred to the powertrain. The activity is progressively developed from global low-frequency behaviour to higher-frequency structural behaviour. First, the low-frequency rigid-body and mount-controlled modes are identified. These modes are mainly influenced by the rubber mounts, global mass distribution, inertia properties, and support stiffness. Then, the analysis is extended to the structural modes of the long arm and bulk powertrain, where local flexibility, arm thickness, bolted connections, and assembled boundary conditions become more important.

The specific role of this thesis is to identify and interpret the correspondence between the experimental modal behaviour measured by EMA and the modal behaviour predicted by the Romax model. The comparison is not limited to listing frequencies. Instead, the experimental and numerical modes are compared through frequency errors, visual mode-shape interpretation, and MAC-based correlation where suitable. This makes it possible to distinguish between modes that are well represented by the numerical model and modes that still require further investigation or model updating.

The motivation for this work is therefore twofold. From an experimental point of view, the thesis develops a reliable roving-hammer EMA procedure for a complex mounted electric powertrain. From a modelling point of view, it provides experimental evidence that can be used to evaluate and improve the Romax model. The validation is considered reliable only if the procedure is consistent at different levels: first on the cantilever beam, then on the low-frequency powertrain modes, and finally on the higher-frequency structural modes of the long arm and bulk assembly.

The work also provides a basis for future development of the project. Additional data from the company test bench may be used in later stages to extend the validation from modal testing toward operational or forced-response conditions. In this way, the present thesis represents a first validation step: it establishes the experimental modal reference and identifies the main discrepancies between the physical powertrain and the numerical model. Future work can then use this reference to improve the simulation model further and to validate the powertrain under more realistic operating conditions.

3.2 Experimental Modal Analysis for model validation

EMA is based on the assumption that the dynamic behaviour of a linear structure can be described as a combination of modal contributions. Each mode is characterized by a natural frequency, a damping factor, and a mode shape. When the structure is excited near one of its natural frequencies, the response is dominated by the corresponding mode. By acquiring the input and output signals over a suitable frequency range, the modal properties can be estimated from the measured FRFs.

In this thesis, the excitation is applied by means of an instrumented impact hammer. This approach is suitable for laboratory modal testing because the input force is directly measured and the excitation point can be easily changed. The method adopted is the roving-hammer technique: the accelerometers are kept fixed at selected reference locations, while the hammer is moved across different excitation points and directions. This strategy is particularly useful when the structure is complex or when moving the accelerometers would alter the mass distribution of the system.

The roving-hammer approach also allows many input locations to be tested with a limited number of sensors. The resulting dataset contains the dynamic relationship between several excitation coordinates and the measured response coordinates. These FRFs are then used for modal parameter identification. In the present work, the modal identification is mainly performed using the PolyMAX estimator available in Simcenter Testlab, while additional post-processing and validation operations are performed in MATLAB.

3.3 Role of the preliminary beam study

Before applying the methodology to the electric powertrain, the complete workflow was developed and validated on a cantilever beam. The use of a beam as a preliminary test case is important because its dynamic behaviour is simpler than that of a complete powertrain and can be interpreted through classical beam theory, numerical simulation, and experimental measurements.

The beam test was used to validate the acquisition chain, including the LMS SCADAS system, the tri-axial accelerometers, the instrumented hammer, the channel mapping, and the Testlab acquisition settings. It was also used to verify the roving-hammer strategy, the quality-control procedure for rejecting double hits and overloads, the construction of FRFs, the use of stabilization diagrams, and the extraction of modal parameters.

The beam case also allowed the MATLAB post-processing pipeline to be developed. This included the import of experimental FRFs, the synthesis of FRFs from identified modal parameters, the evaluation of Maxwell reciprocity, the computation of Auto-MAC and Cross-MAC matrices, the comparison between experimental and numerical mode shapes, and the estimation of damping parameters. The beam therefore represents the methodological benchmark of the thesis.

3.4 Thesis objectives

The main objective of this thesis is to develop and apply a robust roving-hammer EMA procedure for the validation of the numerical modal model of an electric powertrain.

The specific objectives are:

1. to define a complete experimental workflow for modal testing using Simcenter Testlab, LMS SCADAS acquisition hardware, tri-axial accelerometers, and an instrumented impact hammer;
2. to validate the workflow on a cantilever beam before applying it to the powertrain;
3. to develop MATLAB-based post-processing tools for FRF handling, modal synthesis, reciprocity verification, MAC analysis, damping identification, and FE/EMA correlation;
4. to perform experimental modal analysis on an electric powertrain mounted on its support system;
5. to identify the main experimental natural frequencies, damping factors, and mode shapes of the powertrain;
6. to compare the experimental modal properties with the available numerical model;
7. to interpret discrepancies between test and simulation in terms of mount stiffness, boundary conditions, mass distribution, and local structural flexibility;
8. to propose possible model-updating directions for improving the correlation between the experimental and numerical models.

3.5 Thesis organization

Chapter 2 introduces the theoretical background and short literature review. It presents the fundamentals of structural dynamics, EMA, FRFs, impact testing, PolyMAX identification, MAC-based validation, FE-model updating, and the relevance of these tools to electric powertrain NVH.

Chapter 3 introduces the instrumentation and software used in the experimental activities. The working principles of piezoelectric accelerometers, the instrumented impact hammer, the SCADAS acquisition system, and Simcenter Testlab are discussed.

Chapter 4 describes the preliminary cantilever beam study. The chapter presents the experimental setup, instrumentation, roving-hammer acquisition strategy, Testlab workflow, modal identification results, MATLAB post-processing procedure, analytical and numerical comparison, and model-updating results.

Chapter 5 presents the rigid-body identification stage of the electric powertrain. This chapter focuses on the low-frequency, mount-dominated behaviour of the assembly and on the role of the rubber mounts in the global dynamic response.

Chapter 6 presents the long-arm and bulk powertrain structural-mode study. This chapter focuses on the flexible modes of the mounting arms and of the main powertrain body, including frequency comparison with the numerical model and interpretation of local stiffness effects.

Chapter 7 discusses FE/Romax correlation and possible model-updating actions. The discussion focuses on mount stiffness, boundary conditions, mass distribution, long-arm stiffness or thickness modifications, damping assumptions, and local structural flexibility.

Chapter 8 summarizes the conclusions of the thesis and proposes future developments.

4 Theoretical Background and Short Literature Review

4.1 Fundamentals of modal analysis

The dynamic behaviour of a mechanical structure can be described by the equilibrium between inertia, damping, stiffness, and external excitation. In matrix form, the equation of motion of a linear multi-degree-of-freedom system is:

$$[M]\ddot{x}(t) + [C]\dot{x}(t) + [K]x(t) = f(t) \tag{4.1}$$

where $[M]$, $[C]$, and $[K]$ are respectively the mass, damping, and stiffness matrices; $x(t)$ is the displacement vector; and $f(t)$ is the external force vector. Under the assumption of linear behaviour, the response can be interpreted as the superposition of individual modes. Each mode is defined by a natural frequency, a damping ratio, and a mode shape.

Modal analysis starts from the free-vibration problem. If no external force is applied and damping is initially neglected, the equation of motion becomes:

$$[M]\{\ddot{x}(t)\} + [K]\{x(t)\} = 0 \tag{4.2}$$

A harmonic solution can be assumed in the form:

$$\{x(t)\} = \{X_0\}e\hat{}(j\omega t) \tag{4.3}$$

where (ω) is the angular frequency and $\{X_0\}$ is the displacement amplitude vector. Substituting this solution into the undamped free-vibration equation gives:

$$([K] - \omega^2[M])\{X_0\} = \{0\} \tag{4.4}$$

This is the classical undamped eigenvalue problem. Non-trivial solutions exist only when:

$$det([K] - \omega^2[M]) = 0 \tag{4.5}$$

The solutions of this equation provide the eigenvalues and eigenvectors of the system. The eigenvalues are related to the squared natural angular frequencies $\lambda_r = {\omega_r}^2$, while the corresponding eigenvectors represent the mode shapes, $\{X_0\}_r = \{\psi_r\}$

Therefore, each mode (r) is characterized by a natural frequency (ω_r) and a mode shape vector (ϕ_r). The natural frequency in hertz is obtained from $f_r = \omega / 2\pi$.

The physical meaning of the mode shape is the relative deformation pattern of the structure when it vibrates at the corresponding natural frequency. The absolute scale of a mode shape is arbitrary; what is important is the relative motion between the different degrees of freedom. This is why mode-shape comparison methods, such as the Modal Assurance Criterion, are used later in this thesis to compare experimental and numerical modes.

For an assembled structure such as an electric powertrain, the matrices ([M]) and ([K]) are large and contain the information related to the mass distribution, geometry, material properties, bearings, supports, joints, mounting arms, and boundary conditions. In a numerical software such as Romax, these matrices are not manually assembled by the user. They are generated internally from the model definition and from the mechanical properties assigned to the components and connections.

A general damping matrix can make the modal equations coupled and can lead to complex mode shapes. However, in many structural-dynamic applications, damping is represented using proportional damping, also called Rayleigh damping. In this case, the damping matrix is expressed as a linear combination of the mass and stiffness matrices:

$$[C] = \alpha[M] + \beta[K] \tag{4.6}$$

where (α) is the mass-proportional damping coefficient and (β) is the stiffness-proportional damping coefficient. Using the undamped modal matrix ([Ø]), the displacement vector can be written as:

$$\{x(t)\} = [\Psi]\{\eta(t)\} \tag{4.7}$$

Where ($\eta(t)$) is the vector of modal coordinates. By pre-multiplying by ($[\Phi]^T$), the equations of motion can be decoupled into independent modal equations. For mode (r), the modal equation becomes:

$$\ddot{\eta}_r(t) + 2\,\zeta_r\omega_r\dot{\eta}_r(t) + \omega_r^2\eta_r(t) = Q_r(t) \tag{4.8}$$

where ($q_r(t)$) is the modal coordinate, (ω_r) is the undamped natural angular frequency, (ζ_r) is the modal damping ratio, and ($Q_r(t)$) is the modal force.

For Rayleigh damping, the damping ratio of mode (r) is:

$$\zeta_r = \alpha/(2\omega_r) + \beta\omega_r/2 \tag{4.9}$$

This equation shows the different roles of (α) and (β). The mass-proportional term $\left(\alpha/(2\omega_r)\right)$ decreases with frequency and therefore has a hyperbolic trend. The stiffness-proportional term ($\beta\omega_r/2$) increases linearly with frequency. The total damping ratio is the sum of these two contributions.

Although proportional damping preserves undamped mode shapes, the damped eigenvalues are not identical to the undamped ones. For a damped single modal equation, the complex eigenvalues can be written as:

$$s_r = -\zeta_r \omega_r \pm j\omega_r \sqrt{1 - \zeta_r{}^2} \tag{4.10}$$

and the damped natural frequency is:

$$\omega_{d,r} = \omega_{n,r} \sqrt{1 - \zeta_r{}^2} \tag{4.11}$$

The advantage of proportional damping is that the system can still be decoupled using the eigenvectors of the undamped system. In other words, the same mode shapes obtained from the undamped eigenvalue problem can be used to transform the physical coordinates into modal coordinates. This is important because the modal basis remains defined by the undamped eigenvectors, while damping modifies the modal response and the complex eigenvalues.

For lightly damped structures, $(\omega_{d,r})$ is close to (ω_r), but they are not exactly the same. This distinction is important because the undamped eigenvalue problem provides the reference mode shapes and natural frequencies, while damping affects the dynamic response amplitude, resonance width, and decay rate.

In the Romax workflow, the modal analysis of the powertrain is performed on a complex assembled system. The model may include nonlinear elements or nonlinear relationships, for example in bearings, contacts, preloads, or support conditions. Therefore, the numerical procedure starts from the definition of the loads and the static operating condition. Romax first evaluates the static equilibrium of the system under the applied loads. Around this equilibrium point, the system is linearized. The resulting linearized mass and stiffness matrices represent the dynamic behaviour of the assembly for small vibrations around the selected operating condition.

Once the system has been linearized, the modal problem can be solved using the linearized matrices. The extracted numerical natural frequencies and mode shapes are then compared with the experimental modal parameters obtained from EMA. This is the basis of the experimental-numerical correlation performed in the following chapters. In this thesis, the comparison focuses mainly on natural frequencies and mode shapes, while damping is treated separately through the experimental damping ratios and, where necessary, through the proportional damping formulation.

In FE-model validation, modal parameters are useful because they are sensitive to the physical properties of the structure. Natural frequencies are mainly affected by the ratio between stiffness and mass, while mode shapes provide spatial information about how the structure deforms. A comparison between experimental and numerical modal parameters can therefore reveal modelling errors related to mass distribution, material stiffness, joints, boundary conditions, or mount properties.

4.2 Frequency Response Functions

An FRF describes the relationship between an input force applied at one coordinate and the output response measured at another coordinate. Depending on the measured response quantity, the FRF may be expressed as receptance, mobility, or inertance. In this thesis, the measured response is acceleration and the input is force; therefore, the FRFs are mainly inertance functions:

$$H_{ij}(\omega) = \frac{\ddot{x}_i(\omega)}{F_j(\omega)} \tag{4.12}$$

where i is the response coordinate and j is the excitation coordinate. Peaks of the FRF magnitude are associated with resonant behaviour, while the phase evolution provides additional information for distinguishing physical resonances from noise or computational artefacts.

FRFs are also useful for validating the assumption of linearity. In a linear reciprocal system, the FRF measured between two coordinates should be independent of which coordinate is used as input and which is used as output. This property, known as Maxwell reciprocity, can be checked by comparing cross-inertance functions such as H_{ij} and H_{ji}.

The modal properties of a structure can be interpreted from both its free response and its forced response. In Experimental Modal Analysis, the structure is excited by an impact hammer. Although the excitation is applied as an external force, the force pulse is very short in time. After the impact, the structure is left to vibrate and decay freely. Therefore, the measured response can be interpreted as the impulse response of the system.

For a single-degree-of-freedom system subjected to a unit impulse, the free-decay response can be written as:

$$h(t) = \frac{1}{m\omega_d} e^{-\zeta\omega_n t} \sin(\omega_d t), \qquad t > 0 \tag{4.13}$$

where (h(t)) is the impulse response function, (m) is the mass, (ω_n) is the undamped natural angular frequency, (ζ) is the damping ratio, and (ω_d) is the damped natural angular frequency:

$$\omega_d = \omega_n\sqrt{1-\zeta^2} \tag{4.14}$$

This exponential term controls how quickly the response disappears after the hammer impact. The decay rate is governed by the product ($\zeta\omega_n$). Therefore, for the same damping ratio, a higher natural frequency decays faster, while a lower natural frequency decays more slowly. This means that the first mode usually requires the longest observation time, because it has the lowest natural frequency and therefore the slowest exponential decay.

This concept is important for selecting the acquisition time in impact testing. The measurement window must be long enough to capture the free decay of the slowest relevant mode after the hammer impact. If the acquisition time is too short, the response is truncated before it has decayed sufficiently, producing leakage errors in the FRF. If the acquisition time is unnecessarily long, the useful response may have already disappeared and the measurement can become more affected by background noise.

For this reason, only one theoretical impulse-response plot is reported in this thesis. The plot is used to explain the physical meaning of the acquisition time. The same principle is then applied in the beam, low-frequency powertrain, and long-arm tests without repeating the impulse-response figure.

In Simcenter Testlab, the measured time response can also be manipulated by applying a response window, such as an exponential window. This does not change the physical behaviour of the structure, but it modifies the measured time signal before the FRF is calculated. The purpose of the exponential window is to force the response signal to decay more quickly inside the acquisition time. This is useful when the natural free decay of the structure is too long compared with the selected acquisition window, because an unfinished decay can produce leakage in the frequency-domain FRF.

The exponential window therefore acts as a numerical signal-processing tool. It multiplies the measured response by an artificial decay function so that the signal approaches zero before the end of the acquisition record. In this way, the FRF estimation becomes cleaner and leakage effects are reduced.

However, this operation must be used carefully. Since the exponential window introduces additional artificial decay, it can influence the apparent damping of the identified modes. For this reason, the window is used mainly to improve the quality of the FRF estimation, while the physical interpretation of damping must always consider the acquisition settings. In this thesis, this concept is explained only once because the same principle applies to the beam, low-frequency powertrain, and long-arm structural tests.

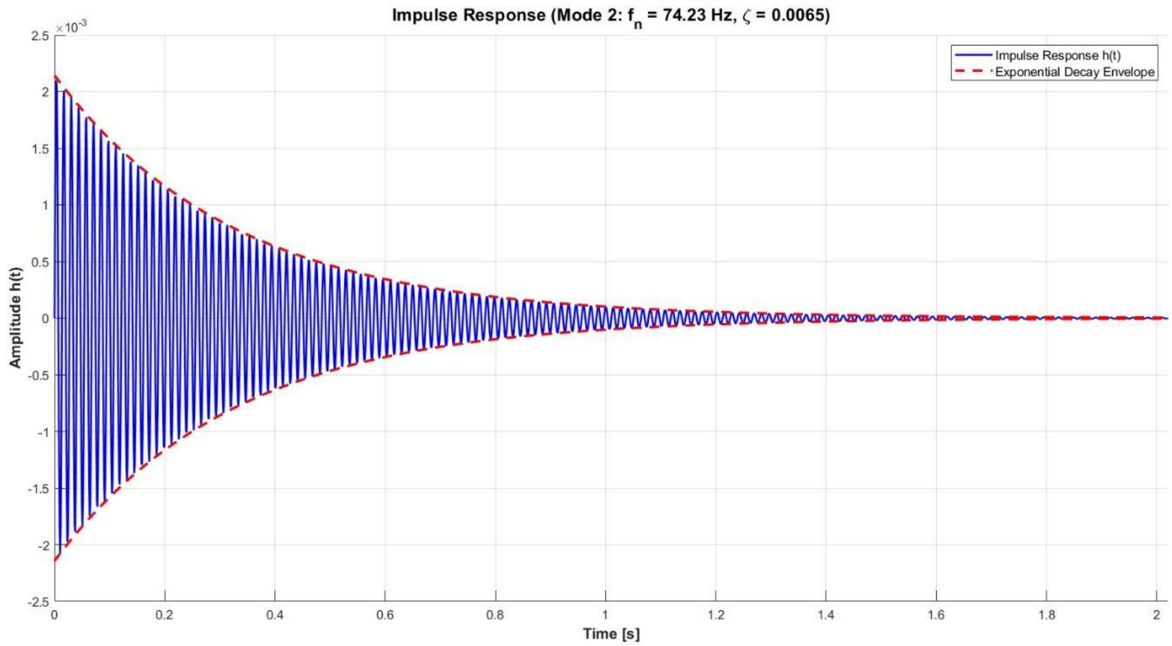

Figure 4.1 :Theoretical impulse response of a damped single-degree-of-freedom system. The response oscillates at the damped natural frequency and decays according to the exponential term $e^{-\zeta\omega_n t}$. The lowest-frequency mode usually has the longest decay duration and therefore governs the minimum acquisition time required for impact testing.

Generally, any structural response vector can be expanded in the modal basis as:

$$v = \sum_{r=1}^{N} C_r \, \psi_r \tag{4.15}$$

where (C_r) are the modal coordinates or modal participation coefficients. This is the principle of modal expansion. The physical response is transformed into modal coordinates in order to decouple the equations of motion, each modal equation is studied as an equivalent single-degree-of-freedom system, and the total response is then reconstructed in physical coordinates by superposition.

A multi-degree-of-freedom system can be interpreted as the superposition of several decoupled modal responses. Each mode behaves like an equivalent single-degree-of-freedom oscillator in modal coordinates. Therefore, the measured physical response is obtained by summing the contribution of all the modes. In the undamped free-response case, the displacement vector can be expressed as:

$$x(t) = \sum_{r=1}^{N} A_r \cos(\omega_r t + \phi_r)\, \psi_r \tag{4.16}$$

Where ($x(t)$) is the physical displacement vector, (A_r) is the amplitude of mode (r), (ω_r) is the natural angular frequency of mode (r), (ϕ_r) is the phase angle, and (ψ_r) is the mode shape vector. This expression shows that the physical motion of the structure is obtained by combining the mode shapes with their time-dependent modal amplitudes.

In the frequency domain, the forced response is described by Frequency Response Functions. For a harmonic excitation, the equation of motion is:

$$[M]\ddot{x}(t) + [C]\dot{x}(t) + [K]x(t) = F_0 e^{i\Omega t} \tag{4.17}$$

where (Ω) is the excitation angular frequency. It is important to distinguish (Ω) from the natural frequency (ω_r). The natural frequency is a property of the structure, while (Ω) is the frequency imposed by the external excitation.

Assuming a steady-state harmonic response, $x(t) = X_0 e^{i\Omega t}$ And substituting into the equation of motion gives:

$$([K] + i\Omega[C] - \Omega^2[M])X_0 = F_0 \tag{4.18}$$

The term in brackets is the dynamic stiffness matrix:

$$[K_d(\Omega)] = [K] + i\Omega[C] - \Omega^2[M] \tag{4.19}$$

Therefore, the response amplitude vector is $X_0 = [K_d(\Omega)]^{-1}F_0$ and the receptance matrix is defined as:

$$[\alpha(\Omega)] = [K_d(\Omega)]^{-1} \tag{4.20}$$

so that $X_0 = [\alpha(\Omega)]F_0$ and the steady-state displacement response becomes:

$$x(t) = [\alpha(\Omega)]F_0 e^{i\Omega t} \tag{4.21}$$

The receptance matrix ($[\alpha(\Omega)]$) relates displacement response to force input. Other FRF forms can be obtained from it. Mobility is the ratio between velocity and force:

$$[\mu(\Omega)] = i\Omega\alpha(\Omega) \tag{4.22}$$

Inertance, also called accelerance, is the ratio between acceleration and force:

$$[A(\Omega)] = -\Omega^2[\alpha(\Omega)] \tag{4.23}$$

In this thesis, the measured response is acceleration and the input is hammer force. Therefore, the experimentally measured FRFs are mainly inertance functions. For an input force applied at coordinate (k) and an acceleration response measured at coordinate (l), the inertance FRF is:

$$A_{lk}(\Omega) = \frac{\ddot{X}_l(\Omega)}{F_k(\Omega)} \tag{4.24}$$

In impact testing, each hammer strike corresponds to a single-input, multi-output measurement. When the hammer excites coordinate (k), the force vector contains a non-zero value only at that coordinate, while the other force components are zero. The acceleration responses are measured simultaneously at the available accelerometer coordinates. By moving the hammer from point to point, several columns of the FRF matrix can be measured.

The direct calculation of the FRF matrix by inverting the dynamic stiffness matrix can be computationally expensive for large systems, because the mass, damping, and stiffness matrices may contain many degrees of freedom. An alternative is to express the FRFs using modal superposition. For the receptance between response coordinate (l) and excitation coordinate (k), the modal form is:

$$\alpha_{lk}(\Omega) = \sum_{r=1}^{N} \frac{\psi_{lr}\psi_{kr}}{m_r(\omega_r^2 - \Omega^2 + i2\zeta_r\omega_r\Omega)} \tag{4.25}$$

where (ψ_{lr}) is the component of mode shape (r) at the response coordinate (l), (ψ_{kr}) is the component of the same mode shape at the excitation coordinate (k), (m_r) is the modal mass, (ω_r) is the natural angular frequency of mode (r), and (ζ_r) is the modal damping ratio.

If the mode shapes are mass-normalized, the modal mass becomes equal to one and the expression becomes:

$$\alpha_{lk}(\Omega) = \sum_{r=1}^{N} \frac{\phi_{lr}\phi_{kr}}{\omega_r^2 - \Omega^2 + i2\zeta_r\omega_r\Omega} \tag{4.26}$$

This modal form is useful because it shows that the FRF is the sum of the contributions of the individual modes. Around a resonance, the corresponding modal term becomes dominant and a peak appears in the FRF magnitude. Therefore, the FRF magnitude is commonly used to identify the frequency regions where modes are present $|\alpha_{lk}(\Omega)|$.

The phase of the FRF also provides important information. Near a resonance, the phase changes rapidly, typically by approximately ($180°$) depending on the FRF type and sign convention. This phase variation helps distinguish physical resonances from noise or numerical artefacts.

Antiresonances can also appear in the FRF. An antiresonance is a frequency where the measured response becomes very small due to the superposition and cancellation of modal contributions. Unlike resonance peaks, antiresonances are strongly dependent on the selected input-output pair and can be sensitive to damping, spatial location, and modal truncation. For this reason, antiresonance regions may also show local drops in coherence during experimental testing, because the response amplitude is small and the signal-to-noise ratio decreases.

In the low-frequency range of this thesis, damping is not the main parameter used for model correlation.

The comparison between EMA and Romax is based mainly on natural frequencies and mode shapes, because these quantities are most directly related to mass, stiffness, mount properties, and boundary conditions. Damping influences the amplitude and width of the FRF peaks, but for lightly damped systems it has a smaller effect on the position of the natural frequencies. Therefore, damping is reported and interpreted, but the main validation criteria remain frequency correlation, mode-shape comparison, and MAC where applicable.

4.2.1 Maxwell reciprocity and symmetry of the FRF matrix

For a linear, time-invariant, passive mechanical system with symmetric mass, damping, and stiffness matrices, the Frequency Response Function matrix is symmetric. This property is known as Maxwell reciprocity. It means that the response measured at coordinate (l) due to a force applied at coordinate (k) is equal to the response measured at coordinate (k) due to the same type of force applied at coordinate (l), $\alpha_{lk}(\Omega) = \alpha_{kl}(\Omega)$.

This property can also be observed from the modal expression of the receptance FRF given in equation (4.25).

$$\alpha_{lk}(\Omega) = \sum_{r=1}^{N} \frac{\psi_{lr}\psi_{kr}}{m_r(\omega_r^2 - \Omega^2 + i2\zeta_r\omega_r\Omega)}$$

If the input and response coordinates are exchanged, the FRF becomes

$$\alpha_{kl}(\Omega) = \sum_{r=1}^{N} \frac{\psi_{kr}\psi_{lr}}{m_r(\omega_r^2 - \Omega^2 + i2\zeta_r\omega_r\Omega)}$$

Since the product of the two modal components is unchanged,

$$\psi_{lr}\psi_{kr} = \psi_{kr}\psi_{lr}$$

it follows that

$$\alpha_{lk}(\Omega) = \alpha_{kl}(\Omega)$$

Therefore, the receptance matrix is symmetric:

$$[\alpha(\Omega)] = [\alpha(\Omega)]^T$$

The same reciprocity concept can be extended to mobility and inertance FRFs, provided that the same physical input-output coordinates and directions are considered. In impact testing, this property is useful because it allows the consistency of the measured FRFs to be checked by comparing cross-FRFs measured between two coordinates with reversed input and response locations.

In the roving-hammer procedure used in this thesis, the accelerometers remain fixed while the hammer is moved between different excitation points. When the excitation coordinate and the response coordinate are exchanged in the FRF matrix construction or in Testlab visualization, the interpretation relies on the reciprocity property of a linear mechanical system. If the structure behaves linearly and the measurements are reliable, the two cross-inertances should have similar magnitude, phase, and resonance peaks.

A lack of reciprocity can indicate a problem in the measurement or in the assumptions. Possible causes include double impacts, poor input-force quality, overloads, insufficient coherence, sensor-direction errors, nonlinear contact behaviour, or local boundary-condition changes during the test. For this reason, reciprocity is used later in the thesis as an experimental quality check. If the reciprocal FRFs show similar resonance peaks and overall trends, the system can be considered sufficiently linear for the purpose of Experimental Modal Analysis.

4.2.2 Residual effects in FRF synthesis and reciprocity interpretation

In modal testing, the measured FRF contains the contribution of all the modes of the real structure. However, during modal identification and FRF synthesis, only a limited number of modes within the selected frequency range are normally retained. The dynamic contribution of modes outside the identified range, or of modes not included in the selected modal model, is usually represented by residual terms.

$$\alpha_{lk}(\Omega) = \sum_{r=1}^{N} \frac{\psi_{lr}\psi_{kr}}{m_r(\omega_r^2 - \Omega^2 + i2\zeta_r\omega_r\Omega)} + R_{lk}(\Omega)$$

The modal expression of the receptance FRF can therefore be written in a more general form as:

$$\alpha_{lk}(\Omega) = \sum_{r=1}^{N} \frac{\varphi_{ir}\varphi_{jr}}{\omega_r^2 - \Omega^2 + 2j\zeta_r\omega_r\Omega} - \frac{LR_{lk}}{\Omega^2} + UR_{lk}$$

where ($R_{lk}(\Omega)$) represents the residual contribution of the modes that are not explicitly included in the summation. These residual terms may include the effect of modes below the selected bandwidth (LR), modes above the selected bandwidth (UR), weakly excited modes, local modes that are not clearly identified, and modelling or measurement limitations.

Residual effects are especially important when experimental FRFs are compared with synthesized FRFs. The synthesized FRF is reconstructed using only the selected modal parameters. Therefore, it should reproduce the main resonance peaks and the global dynamic trend, but it may not perfectly reproduce all off-resonance regions, antiresonances, phase details, or local irregularities. A discrepancy between experimental and synthesized FRFs does not automatically mean that the identified modes are incorrect. It may also be caused by modal truncation, residual contributions, measurement noise, or local flexibility that is not represented by the retained modal set.

Residual effects are also relevant when interpreting Maxwell reciprocity. In theory, for a linear reciprocal system, the cross-inertance (A_{lk}) should be equal to (A_{kl})when the same physical directions are considered. In practice, the two measured reciprocal FRFs may not be perfectly identical. Small differences can appear because the impacts are performed manually, the signal-to-noise ratio changes between measurement points, the response may be weak near antiresonances, and residual contributions from unmodelled modes may influence the FRF differently at different input-output coordinates.

For this reason, reciprocity is interpreted in this thesis as a quality and consistency check rather than as an exact equality requirement. A good reciprocity result means that the two reciprocal FRFs show similar resonance peaks, comparable phase behaviour, and the same global trend. Local differences near antiresonances or in low-response regions are acceptable if the coherence and impact quality remain satisfactory. Large differences, instead, may indicate double impacts, poor input energy, overloads, incorrect sensor direction, nonlinear contact, or a change in boundary condition during the test.

The residual concept is therefore important for the interpretation of the beam and powertrain results. In the beam case, residual effects explain why the synthesized FRFs and reciprocal cross-inertances may not match perfectly over the full bandwidth, even when the identified modes are physically meaningful. In the powertrain case, residuals are even more relevant because the structure is more complex, the number of local modes is higher, and the measured spatial resolution is limited by the available accelerometer locations.

4.3 EMA as a powerful tool for structural characterization

EMA is a controlled testing method used to identify modal parameters directly from measured data. The key advantage of EMA is that both the excitation and the response are known. This makes the method suitable for laboratory validation of numerical models because the measured FRFs provide a direct input-output representation of the physical structure.

In this thesis, EMA is used not only to identify the experimental modal properties of the beam and the powertrain, but also to create an experimental reference for numerical correlation. The experimental natural frequencies are compared with the numerical eigenfrequencies, while the experimental mode shapes are compared with the numerical eigenvectors through MAC-based indicators.

Classical modal-testing references, such as Ewins [5], describe EMA as a fundamental tool for identifying structural dynamic properties. More recent vehicle-NVH literature confirms that experimental validation remains essential for modern electric powertrains because electric vehicles introduce new excitation mechanisms and reduced masking noise [1-4].

4.4 Impact testing and the roving-hammer strategy

In this thesis, the experimental excitation is applied using an instrumented impact hammer. The hammer contains a force transducer that measures the contact force during the impact. The response of the structure is measured using accelerometers. The acquired force and acceleration signals are then processed to calculate Frequency Response Functions.

The hammer impact can be interpreted as a short-duration force pulse. After the impact, the structure is left to vibrate freely and its response decays with time. This makes impact testing suitable for modal analysis because the measured response contains the contribution of the modes excited by the hammer. The quality of the test depends on the ability of the hammer impact to provide sufficient input energy over the frequency range of interest.

The frequency content of the impact is strongly influenced by the hammer tip. For this reason, the available hammer tips are introduced first, and their frequency-response behaviour is then discussed.

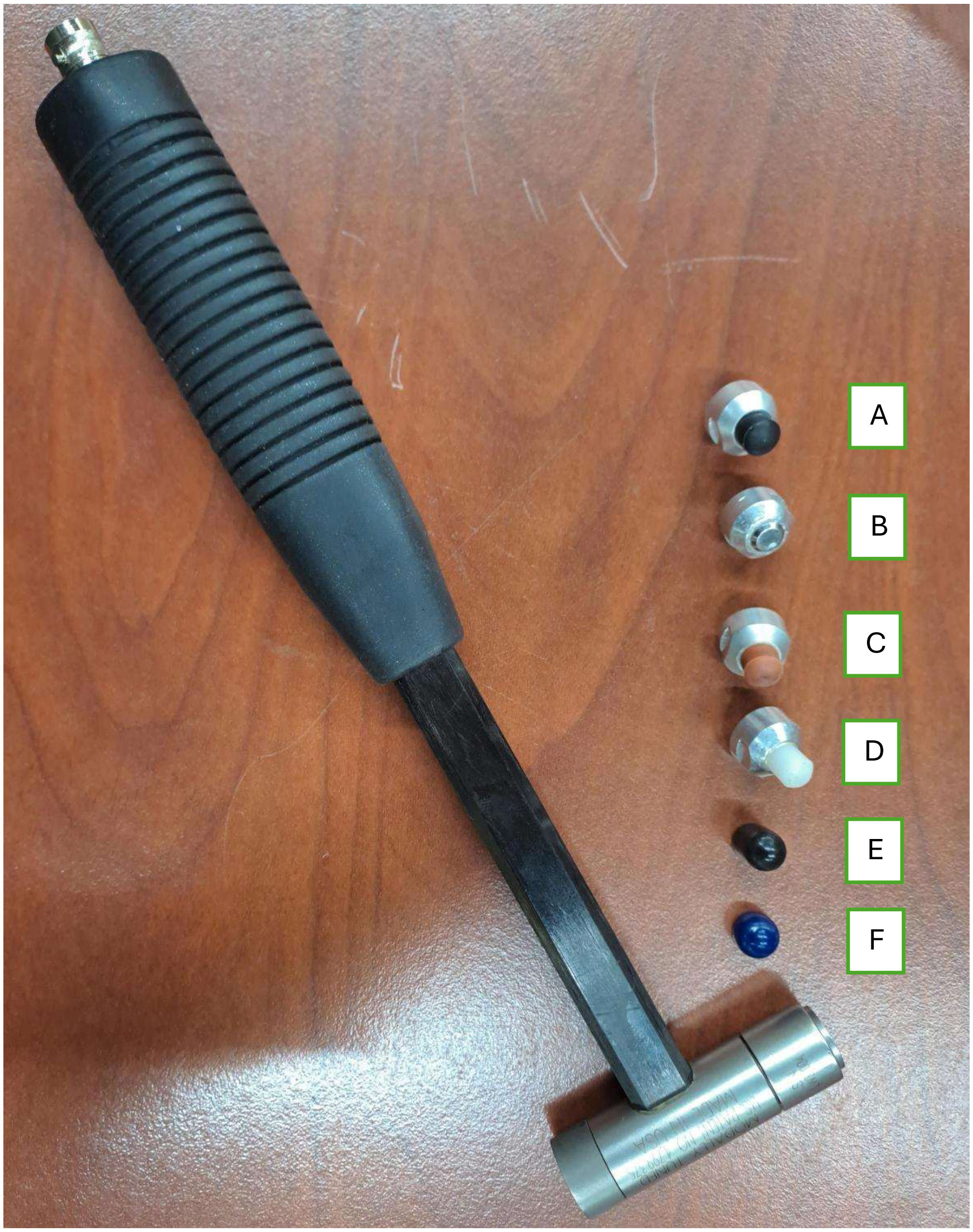

Figure 4.1: The Hammer, the tips and the covers available in the Lab, A (Soft Impact Tip), B (Hard Impact metallic Tip), C (Super soft Impact Tip), D (Medium Impact Tip) , E,F (Tip covers, only for tip protection)

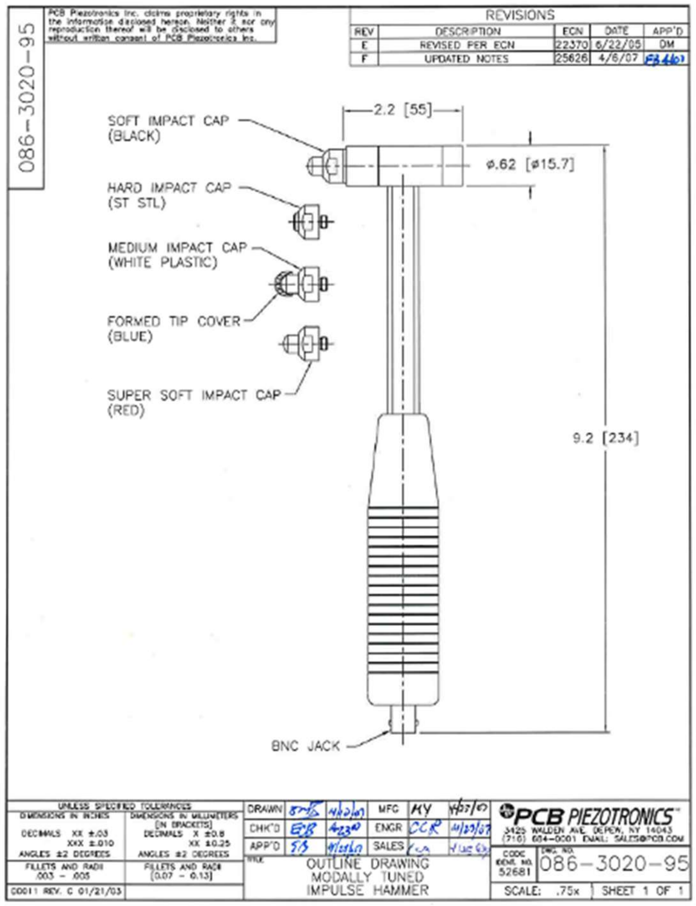

Figure 4.2: The description of the hammer tips

Figure 4.1 shows the instrumented impact hammer and the available tips and covers used in the laboratory. Tip A is the soft impact tip, tip B is the hard metallic impact tip, tip C is the super-soft impact tip, and tip D is the medium impact tip. The elements labelled E and F are tip covers. These covers are used to protect the tip and can help reduce tip damage. However, the main control of the excitation bandwidth is given by the selected impact tip.

After introducing the available hammer tips, their influence on the excitation bandwidth must be considered. The selected tip changes the contact duration between the hammer and the structure, and therefore modifies the frequency content of the applied force pulse. For this reason, the frequency-response behaviour of the hammer tips is reported in Figure 4.3.

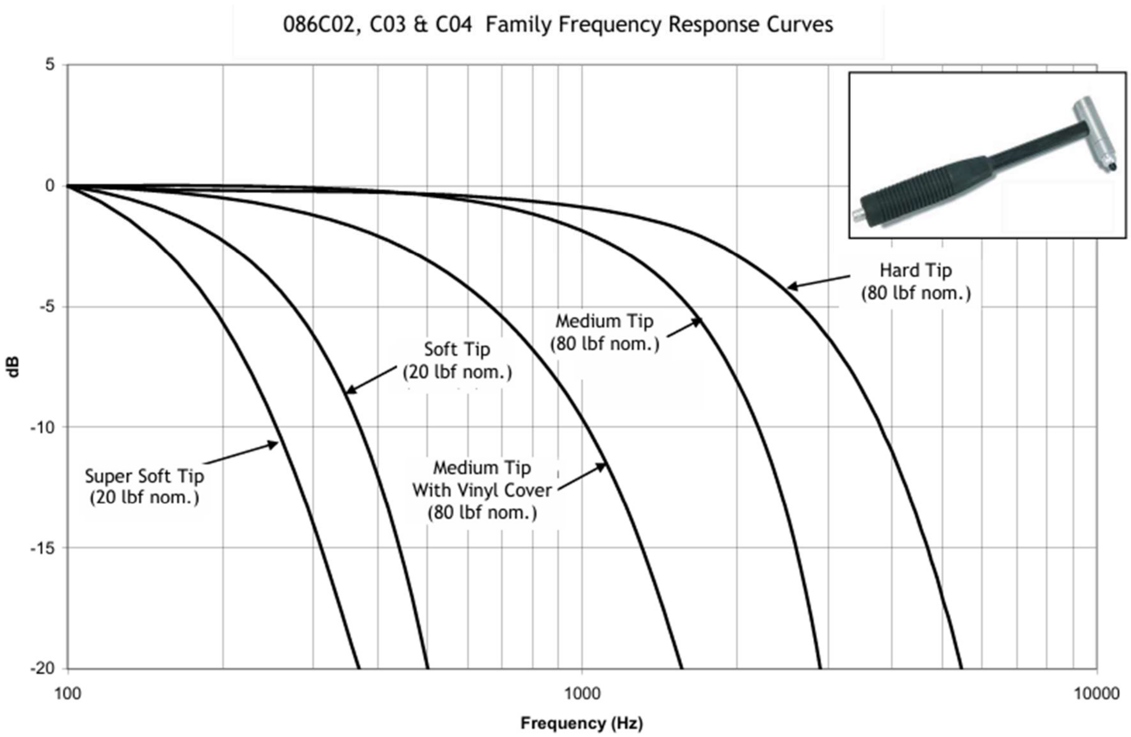

Figure 4.3: Frequency-response curves of the PCB 086C03 hammer tips. The hard tip provides the widest excitation bandwidth, while softer tips concentrate the input energy at lower frequencies.

Figure 4.3 shows that the hammer tip must be selected according to the target frequency range of the experiment. A softer tip produces a longer contact time and concentrates the input energy at lower frequencies. This is useful when the objective is to excite low-frequency modes and when a smoother force pulse is required. A harder tip produces a shorter contact time and extends the excitation bandwidth toward higher frequencies. This is useful when structural modes at higher frequencies must be excited.

The medium tip provides an intermediate compromise between low-frequency input energy and useful bandwidth. In this thesis, the medium tip was selected for the low-frequency powertrain rigid-body test because the objective was to excite the mount-controlled modes while preserving enough bandwidth for the first structural resonances. The hard metallic tip was selected for the long-arm structural test because the target frequency range was higher and required stronger high-frequency excitation. Therefore, hammer-tip selection was part of the measurement setup and was later verified through the Testlab bandwidth check.

The measurement strategy adopted in this work is the roving-hammer method. In this configuration, the accelerometers remain fixed at selected response locations, while the hammer is moved from one excitation point to another. Each hammer impact produces one input force signal and several acceleration response signals. Therefore, each impact corresponds to a single-input, multi-output measurement.

For example, if the hammer excites coordinate (k), the force vector contains a non-zero component only at that coordinate:

$$F = [0\ 0\ F_k\ 0\ \vdots]$$

The accelerometers measure the responses at the selected output coordinates. The corresponding inertance FRFs are then calculated as in equation (4.24).

$$A_{lk}(\Omega) = \frac{\ddot{X}_l(\Omega)}{F_k(\Omega)}$$

where (A_{lk}) is the inertance between response coordinate (l) and excitation coordinate (k). By moving the hammer to different excitation coordinates, different columns of the FRF matrix are measured. In this way, the dynamic behaviour of the structure can be described using many input-output relationships without moving the accelerometers.

The main advantage of the roving-hammer method is that the sensor mass distribution remains constant during the measurement campaign. This is important because moving accelerometers can modify the dynamic behaviour of lightweight structures and can also introduce mounting variability. Keeping the accelerometers fixed also improves repeatability and reduces the risk of sign or orientation errors. During the test, each impact must be checked before it is accepted. A valid impact should have a clean force pulse, no double hit, no overload, sufficient input level, clear response, and good coherence in the frequency range of interest. The instantaneous FRF is inspected after each impact, while the averaged FRF is used to improve repeatability. If an impact is affected by double contact, poor input level, abnormal PSD, overload, or poor coherence, it is rejected and repeated.

The roving-hammer method is also connected to the reciprocity property described in Section 4.2. For a linear reciprocal system, the cross-FRF measured between two coordinates should be the same when input and response are exchanged. Therefore, reciprocal FRFs can be compared to verify the consistency and linearity of the measurement. In this thesis, Maxwell reciprocity is used as a validation check in the beam study and as a general quality-control concept for the powertrain measurements.

4.5 Modal parameter estimation and PolyMAX

After the FRFs have been measured, the modal parameters must be extracted from the experimental dataset. The main parameters of interest are the natural frequencies, damping ratios, and mode shapes. Several modal parameter estimation methods are available, ranging from simple peak-picking to more advanced curve-fitting algorithms. In this thesis, the main estimator used in Simcenter Testlab is PolyMAX.

PolyMAX, also called the polyreference least-squares complex frequency-domain method, is a frequency-domain modal parameter estimation technique. It uses the measured FRFs as input data and estimates a modal model capable of reproducing the measured dynamic behaviour. One of the main advantages of PolyMAX is the stabilization diagram, which allows the user to distinguish physical modes from mathematical or noise-related poles.

The stabilization diagram is built by increasing the model order. At each model order, the algorithm estimates a set of poles. A physical mode should appear repeatedly when the model order is increased. In other words, its frequency, damping ratio, and mode-shape information should remain stable. Mathematical poles, noise-related poles, or computational artefacts usually appear only at isolated model orders, or they move significantly when the model order changes.

In the Testlab workflow used in this thesis, the stabilization diagram was not interpreted automatically. The final selection of modes was performed by combining several criteria. First, the pole had to be stable in frequency. Second, the damping ratio had to be stable and physically reasonable. Third, the pole had to correspond to a visible resonance peak in the measured FRFs or in the FRF sum. Fourth, the corresponding mode shape had to be physically meaningful when animated. A pole was therefore not accepted only because it appeared in the stabilization diagram; it also had to represent a real structural deformation of the tested system.

The practical modal-identification procedure used in Testlab can be summarized as follows. First, the measured FRFs were imported into the modal analysis worksheet. Then the frequency range of interest was selected according to the test objective. For the beam, the selected range covered the bending and torsional modes of the cantilever specimen. For the low-frequency powertrain analysis, the selected range focused on the rigid-body and mount-controlled modes. For the long-arm structural analysis, a higher-frequency range was used to capture the structural modes of the arm and powertrain body.

After defining the frequency range, PolyMAX was applied and the stabilization diagram was generated. Stable poles were selected by checking their frequency stability, damping stability, and physical relevance. The mode shapes were then animated in Testlab to verify whether the selected modes were consistent with the expected motion of the structure. For the beam, this meant checking bending and torsional deformation patterns. For the powertrain, this meant distinguishing translations, rotations, mount-controlled modes, and structural deformation of the arms or body.

After the modal parameters were selected, Testlab was used to synthesize FRFs from the identified modal model. The synthesized FRFs were compared with the measured experimental FRFs. This step was important because a reliable set of modal parameters should reproduce the main resonance peaks, antiresonance regions, and global trend of the measured FRFs. If the synthesized FRF did not reproduce the experimental behaviour, the pole selection was checked again and, if necessary, modified.

Therefore, the stabilization diagram was used as a guide, but the final modal selection was based on a combined engineering judgement. The selected modes had to be stable in the PolyMAX diagram, visible in the FRFs, physically meaningful in the mode-shape animation, and able to reconstruct the measured FRFs with acceptable accuracy. The PolyMAX method is a standard reference for industrial modal testing and is directly relevant to the Testlab workflow used in this thesis. Peeters et al. introduced the PolyMAX frequency-domain method as an effective modal parameter estimation approach and highlighted the use of stabilization diagrams for identifying physical modes from measured FRFs [8].

4.6 Modal validation using MAC

The comparison between experimental and numerical mode shapes is a fundamental step in modal validation. Natural frequencies are useful indicators, but they are not sufficient to identify the correspondence between modes. In a complex structure, two modes can have similar frequencies while representing different deformation patterns. Similarly, a numerical model that has not yet been validated may contain modes in a different order from the experimental sequence, or it may include additional modes that were not clearly identified experimentally. For this reason, mode-shape comparison must be performed in addition to frequency comparison.

The Modal Assurance Criterion is one of the most widely used indicators for comparing mode shapes. It evaluates the degree of linear similarity between two modal vectors [6]. Given two mode-shape vectors (ϕ_i) and (ϕ_j), the MAC value is defined as:

$$MAC(i,j) = \frac{\left|{\phi_i}^H \phi_j\right|^2}{\left({\phi_i}^H \phi_i\right)\left({\phi_j}^H \phi_j\right)} \tag{4.27}$$

where the superscript (H) indicates the complex conjugate transpose. If the mode-shape vectors are real, this becomes the ordinary transpose:

$$MAC(i,j) = \frac{\left({\phi_i}^T \phi_j\right)^2}{\left({\phi_i}^T \phi_i\right)\left({\phi_j}^T \phi_j\right)} \tag{4.28}$$

The MAC value ranges from 0 to 1. A value close to 1 means that the two mode-shape vectors are very similar from a geometrical point of view. In other words, the relative deformation pattern described by the two vectors is almost the same. A value close to 0 means that the two mode-shape vectors are poorly correlated and represent different deformation patterns. MAC does not compare the absolute amplitude of the modes, because mode shapes can be scaled arbitrarily. Instead, it compares the spatial distribution of the modal deformation.

In this thesis, MAC is used in two forms: Auto-MAC and Cross-MAC. Auto-MAC is computed between mode shapes belonging to the same dataset. For example, it can be computed between the experimental modes identified from the same EMA test. In this case, the diagonal terms are equal to 1 because each mode is compared with itself. The off-diagonal terms indicate whether two different modes have a similar geometry. Therefore, Auto-MAC is interpreted as a geometrical similarity check within the same modal basis. Low off-diagonal values indicate that the identified modes have clearly different deformation patterns, while high off-diagonal values may indicate modes with similar spatial shapes, closely spaced modes, insufficient measurement resolution, or possible identification issues.

In the context of an EMA performed on either a powertrain or a beam structure, the AutoMAC is useful for verifying whether the experimentally identified modes are clearly distinguishable from each other and properly observable with the selected measurement points. Ideally, the AutoMAC matrix should show unitary values along the main diagonal, since each mode is perfectly correlated with itself, and low off-diagonal values, indicating that different modes have clearly distinct spatial deformation patterns. High off-diagonal values may indicate that two or more identified mode shapes are not clearly distinguishable over the selected measurement degrees of freedom. This condition may arise for different reasons:

- Closely spaced modes with critical identification conditions: when two modes have close natural frequencies, their identification may become more difficult if the measured FRFs are affected by high modal damping, low excitation level of one or both modes, poor signal-to-noise ratio, or insufficient frequency resolution. Under these conditions, even robust estimators such as PolyMAX may provide mode shapes that are partially mixed or not clearly distinguishable over the selected measurement degrees of freedom.

- Limited or non-informative measurement grid: two physically different modes may appear similar when observed only through a limited number of measurement points or directions. Therefore, high off-diagonal AutoMAC values may indicate that the selected measurement grid is not sufficiently dense or informative to properly distinguish the corresponding mode shapes.

- Uncertainties in the modal identification process: measurement noise, low coherence, non-optimal curve fitting, or poor excitation of some modes may reduce the reliability of the estimated mode shapes and increase their mutual correlation.

The Auto-MAC matrix can be written as:

$$AutoMAC(i,j) = \frac{\left|\phi_i^{EMA^H}\phi_j^{EMA}\right|^2}{\left(\phi_i^{EMA^H}\phi_i^{EMA}\right)\left(\phi_j^{EMA^H}\phi_j^{EMA}\right)} \tag{4.29}$$

Where (ϕ_i^{EMA}) and (ϕ_j^{EMA}) are two experimental mode shapes from the same EMA dataset.

Cross-MAC is computed between two different datasets, usually experimental and numerical mode shapes. In this thesis, Cross-MAC is used to compare the mode shapes identified experimentally by EMA with the mode shapes predicted by the FE or Romax model. The Cross-MAC matrix is defined as:

$$CrossMAC(i,j) = \frac{\left|\phi_i^{EMA^H}\phi_j^{SYM}\right|^2}{\left(\phi_i^{EMA^H}\phi_i^{EMA}\right)\left(\phi_j^{SYM^H}\phi_j^{SYM}\right)} \tag{4.30}$$

where (ϕ_i^{EMA}) is the experimental mode-shape vector and (ϕ_j^{SYM}) is the numerical mode-shape vector. In the powertrain analysis, the numerical mode shapes are obtained from Romax, while the experimental mode shapes are obtained from Testlab.

Cross-MAC is especially important when the numerical model has not yet been validated. In this situation, it is not safe to assume that the first experimental mode corresponds to the first numerical mode, the second experimental mode to the second numerical mode, and so on. The sequence of modes may change because of differences in mount stiffness, local flexibility, mass distribution, joint stiffness, boundary conditions, or numerical modelling assumptions. Some numerical modes may also be missing experimentally, or some experimental modes may not be well represented in the numerical model.

For this reason, the comparison must start from the similarity of the mode shapes, not only from the order of the frequencies. The Cross-MAC matrix makes this possible because each experimental mode is compared with all candidate numerical modes. The best correspondence is then selected by considering the highest MAC value together with frequency proximity and physical interpretation of the deformation pattern. This approach reduces the risk of pairing modes incorrectly.

In the present thesis, MAC is used first in the cantilever beam validation stage and then in the powertrain correlation stage. In the beam case, Auto-MAC is used to check the geometrical separation of the experimentally identified modes, while Cross-MAC is used to compare experimental and FE mode shapes. In the powertrain case, the CrossMAC is used to identify the Romax mode shapes that best correspond to the experimental EMA modes, especially when the numerical model provides a larger number of candidate modes than those identified experimentally. In this context, each experimental mode is compared with the available numerical modes, and the numerical mode showing the highest CrossMAC value is selected as the best matching counterpart.

The interpretation of MAC must be made carefully. A high MAC value indicates strong similarity between the measured coordinates, but it does not guarantee that the complete three-dimensional deformation of the real structure is fully captured. The value depends on the number and location of measurement points, the selected directions, coordinate-system consistency, sensor orientation, and the spatial resolution of the experimental geometry. Therefore, MAC is not used alone. It is combined with frequency comparison, visual inspection of mode shapes, FRF validation, and physical understanding of the structure.

4.7 FE-model validation and updating

Finite element models are built using assumptions regarding geometry, material properties, joints, constraints, and boundary conditions. These assumptions can lead to discrepancies between numerical and experimental modal properties. FE-model updating aims to reduce these discrepancies by modifying selected model parameters so that the numerical response becomes closer to the measured response.

Model updating should be physically meaningful. A numerical model can be forced to match experimental frequencies by changing arbitrary parameters, but such a model may lose predictive value. The selected updating parameters should therefore correspond to real uncertain physical properties, such as mount stiffness, joint stiffness, material stiffness, mass distribution, or boundary-condition compliance. The importance of FE-model refinement for powertrain mount brackets [10,11] has also been highlighted in recent automotive-NVH work .

4.8 Summary of literature position

The literature supports three key ideas behind this thesis. First, EMA is a robust and widely accepted method for identifying modal parameters from measured FRFs. Second, electric powertrains create specific NVH challenges, making modal validation increasingly important in the vehicle-development process. Third, FE-model validation requires not only frequency comparison but also mode-shape correlation and physically meaningful model updating.

5 Instrumentation and Software

5.1 Overview of the measurement chain

The experimental measurement chain used in this thesis consists of four main elements:

1. sensors installed on or applied to the structure;
2. an excitation device used to input a known force;
3. a data acquisition system used to condition and digitize the signals;
4. acquisition and post-processing software used to calculate FRFs and extract modal parameters.

For both the beam and the powertrain activities, the measured input is the hammer force and the measured output is the acceleration response. The acquisition system records the time histories of force and acceleration, and Testlab processes these signals to estimate the inertance FRFs.

Component	Characteristics	Value
LMS SCADAS Mobile	BNC Input channels	16
	BNC Output channel	2
	Frequency range [kHz]	0÷242
	ICP High pass filter CF [Hz]	0.5
Impact Hammer PCB Model 086C03	Sensitivity [mV/N]	2.199
	Measurement range pk [N]	±2224
	Hammer mass [kg]	0.16-0.235
	Resonant frequency [kHz]	>22
	Tips number [-]	4
Tri-axial accelerometer PCB 356A45 TEDS s.n. LW329671	Sensitivity x-axis [mV/g]	96.4
	Sensitivity y-axis [mV/g]	96.7
	Sensitivity z-axis [mV/g]	96.8

	Frequency range [Hz]	0.7÷7000
	Measurement range pk [m/s2]	±490
	Resonant frequency [kHz]	>30
	Size: cubic edge [m]	10.2·10-3
	Weight: device [kg]	4.2·10-3
Tri-axial accelerometer PCB 356A45 TEDS s.n. LW330254	Sensitivity x-axis [mV/g]	99.0
	Sensitivity y-axis [mV/g]	96.7
	Sensitivity z-axis [mV/g]	96.6
	Frequency range [Hz]	0.7÷7000
	Measurement range pk [m/s2]	±490
	Resonant frequency [kHz]	>30
	Size: cubic edge [m]	10.2·10-3
	Weight: device [kg]	4.2·10-3
Tri-axial accelerometer PCB 356A45 TEDS s.n. LW329671	Sensitivity x-axis [mV/g]	95.9
	Sensitivity y-axis [mV/g]	96.2
	Sensitivity z-axis [mV/g]	94.8
	Frequency range [Hz]	0.7÷7000
	Measurement range pk [m/s2]	±490
	Resonant frequency [kHz]	>30
	Size: cubic edge [m]	10.2·10-3
	Weight: device [kg]	4.2·10-3

Table 0: Component characteristics and their values

5.2 Tri-axial piezoelectric accelerometers

The acceleration response was measured using PCB 356A45 tri-axial ICP accelerometers. A piezoelectric accelerometer converts mechanical acceleration into an electrical signal. When the sensor is accelerated, the inertial force acting on the internal seismic mass stresses the piezoelectric material, producing an electrical charge proportional to the applied acceleration. In ICP accelerometers, the signal conditioning electronics are integrated in the sensor, which simplifies cabling and improves signal robustness.

A tri-axial accelerometer measures acceleration along three orthogonal directions. This is particularly useful in modal testing because the motion of a structure is generally three-dimensional. For the powertrain, tri-axial sensing is necessary because the mounting arms, housing, and rubber mounts can produce coupled motion in multiple directions.

The PCB 356A45 model is specified by the manufacturer as a tri-axial ICP accelerometer with nominal sensitivity of 100 mV/g, measurement range of +/-50 g peak, and frequency range up to 7000 Hz within +/-5 percent amplitude tolerance and up to 10000 Hz within +/-10 percent amplitude tolerance [12]. In the experimental activity, the actual sensitivities of the individual sensors were entered in Testlab according to the calibration data.

Figure 5.1: PCB 356A45 tri-axial accelerometer

5.3 Instrumented impact hammer

The input force was applied using a PCB 086C03 instrumented impact hammer. An impact hammer contains a force transducer near the hammer head. When the hammer strikes the structure, the sensor measures the contact force as a time-domain pulse. This force signal is used as the reference input for FRF estimation.

The input force was applied using a PCB 086C03 instrumented impact hammer. The hammer contains an ICP quartz force sensor mounted near the striking end of the hammer head. During impact, the sensing element converts the applied contact force into an electrical signal that is acquired together with the acceleration responses. This force signal represents the reference input used for FRF estimation.

The hammer tip is a critical part of the excitation system because it affects the pulse width and the frequency content of the applied force. Softer tips increase the contact duration and concentrate the input energy at lower frequencies, while stiffer tips reduce the contact duration and extend the useful excitation bandwidth. The PCB manual states that tips of different stiffness allow the pulse width and frequency content of the force to be varied, while an extender mass can be used to concentrate more energy at lower frequencies [13] . Therefore, the hammer tip must be selected according to the frequency range of interest, the stiffness of the tested structure, and the required input energy.

The influence of hammer-tip stiffness on the excitation bandwidth was discussed in Section 4.4, where the available tips and their frequency-response behaviour were introduced.

Figure 5.2: PCB 086C03 impact hammer

5.4 SCADAS acquisition system

The acquisition system used in the experimental activity was an LMS/Simcenter SCADAS Mobile unit. SCADAS hardware is designed for physical testing applications and supports the acquisition of vibration, force, strain, displacement, sound, and other physical quantities [14] . The system provides signal conditioning and synchronized multi-channel data acquisition, which are essential for modal testing.

In this thesis, the SCADAS unit was used to acquire the force signal from the impact hammer and the acceleration signals from the tri-axial accelerometers. The accelerometer channels were configured as ICP channels, while the hammer channel was configured as a force input. During the preliminary activities, two SCADAS input ports were found to be non-functional and were excluded from the channel mapping.

The use of a multi-channel acquisition system is important because modal testing requires phase-consistent measurements between force and acceleration channels. Any time shift or phase error between channels would directly affect the estimated FRFs and therefore the identified mode shapes.

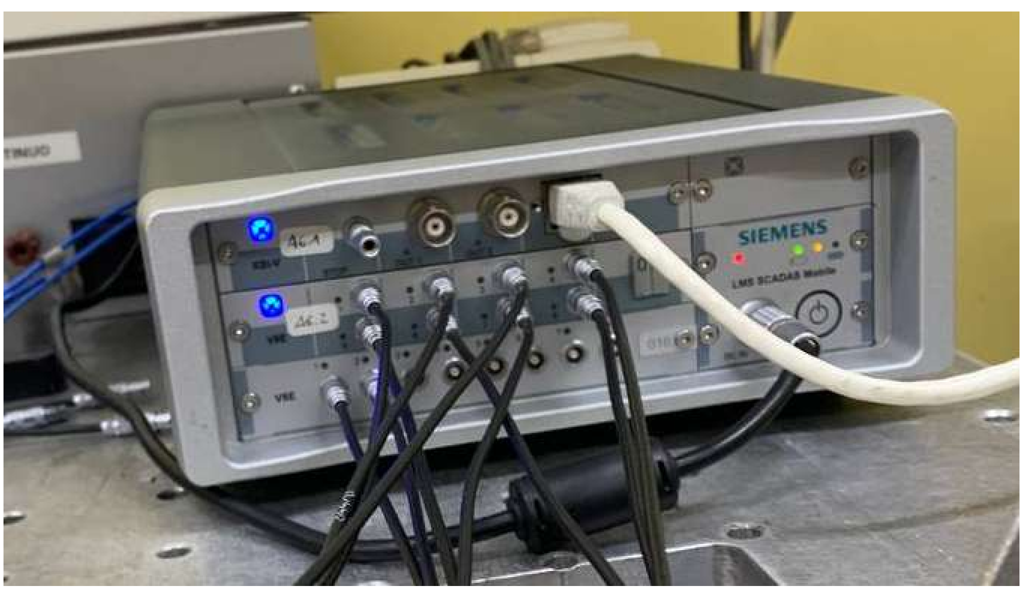

Figure 5.3: SCADAS acquisition system

5.5 Simcenter Testlab

Simcenter Testlab was used for test setup, geometry definition, channel configuration, impact testing, FRF estimation, and modal parameter identification [15] . In the impact-testing workflow, the user defines the measurement geometry, assigns the physical sensors to nodes and directions, configures the acquisition parameters, and performs the hammer impacts.

During acquisition, the software displays the force input, the acceleration response, the instantaneous FRF, the averaged FRF, and the coherence function. These plots are used to evaluate the quality of each impact. Measurements affected by overloads, double hits, or poor coherence are rejected and repeated.

After the acquisition phase, Testlab is used to generate the FRF dataset and identify modal parameters through PolyMAX. The stabilization diagram is used to select the stable poles corresponding to physical modes. The identified natural frequencies, damping ratios, and mode shapes can then be exported for further post-processing in MATLAB.

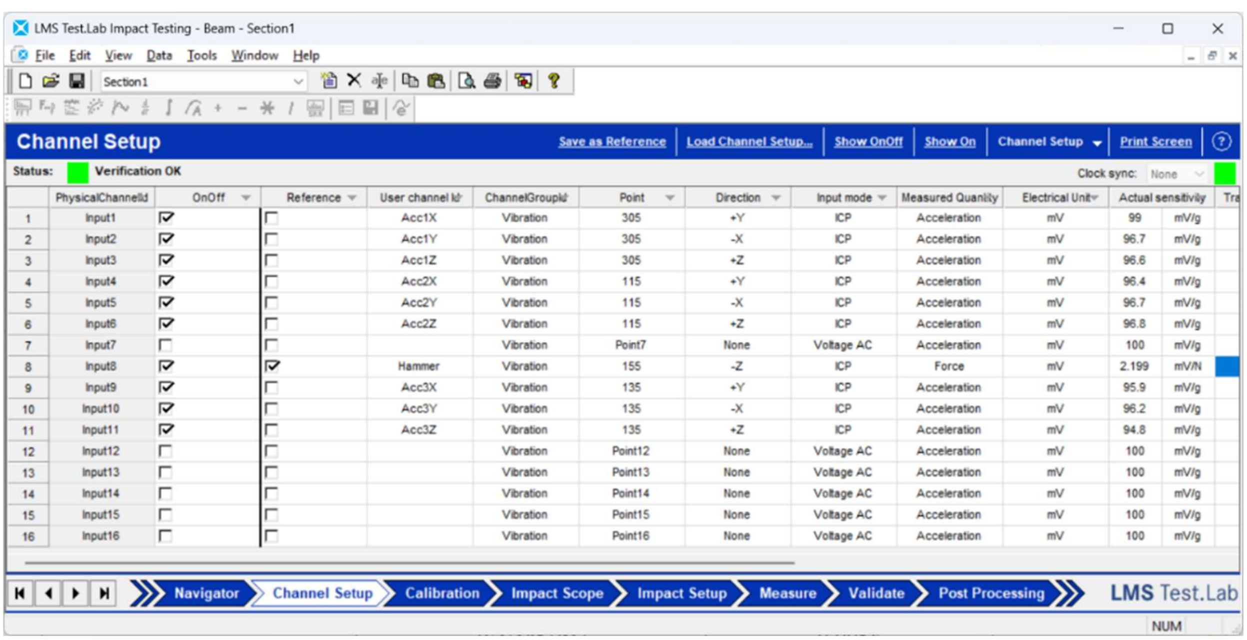

Figure 5.4: Testlab channel setup screenshot

5.6 Complete Testlab experimental workflow

Simcenter Testlab was used as the main software environment for the complete experimental modal analysis workflow. The software was used to define the measurement geometry, configure the acquisition channels, set the impact-test parameters, acquire the FRFs, perform data-quality checks, identify the modal parameters with PolyMAX, and export the modal results for further MATLAB post-processing.

The same general Testlab workflow was used for the cantilever beam, the low-frequency powertrain test, and the long-arm structural test. The main difference between the tests was the selected geometry, frequency bandwidth, hammer tip, acquisition time, and the number of measured excitation points. The complete workflow is described in the following subsections.

5.6.1 Overview of the Testlab workflow

The Testlab workflow can be divided into three main phases:

1. Pre-test preparation, including project creation, geometry definition, hardware connection, channel setup, impact scope, trigger setup, bandwidth check, and windowing.

2. Measurement phase, including roving-hammer impacts, real-time FRF estimation, coherence checks, and impact acceptance or rejection.

3. Modal post-processing, including FRF-set preparation, PolyMAX modal identification, mode-shape animation, Auto-MAC validation, FRF synthesis, and modal-data export.

5.6.2 Project creation and geometry definition

The first step in Testlab was the creation of a new project. After creating the project, the experimental geometry was defined in the Geometry worksheet. The geometry is necessary because the measured FRFs and identified mode shapes must be associated with physical positions on the tested structure. The Geometry worksheet contains several subsections, including components, nodes, lines, surfaces, mesh area, and torsional nodes. In this thesis, the geometry definition was mainly based on components, nodes, and lines.

5.6.2.1 Component definition

The geometry definition started from the component subsection. A single component was created to represent the tested system. For the powertrain test, the complete powertrain assembly was treated as one experimental component. This simplification was acceptable because the purpose of the Testlab geometry was not to reproduce the full CAD topology, but to create a clear experimental geometry for mode-shape visualization.

5.6.2.2 Node definition

After creating the component, the measurement nodes were defined. The node table contains the node name, the full name, and the node coordinates. The full name is generated from the component name followed by the node number. The coordinates were entered manually according to the measured physical positions of the nodes and with respect to the selected experimental origin. This step is important because the relative position of the nodes affects the visualization of the mode shapes. If the coordinates are not consistent with the real structure, the animated mode shapes may be misleading, even if the measured FRFs are correct.

5.6.2.3 Line definition

After defining the nodes, the lines subsection was used to connect selected nodes. These lines were introduced only for visualization. They do not add mass or stiffness to the structure. Their function is to make the animated deformation shapes easier to interpret. For example, in the powertrain test, lines were used to connect nodes on the long arm, short arm, rear arm, and powertrain body. This allowed translations, rotations, bending, and torsional deformation to be visualized more clearly during the modal analysis stage.

5.6.3 Hardware connection and SCADAS channel verification

Before defining the acquisition channels in Testlab, the measurement hardware was connected. The SCADAS unit was switched on and connected to the acquisition computer through an Ethernet cable. The tri-axial accelerometers and the instrumented impact hammer were then connected to the SCADAS input ports. Each tri-axial accelerometer requires three input channels, one for each measurement direction. The impact hammer requires one additional input channel for the force signal. Therefore, the number of active SCADAS channels depends on the number of accelerometers used in the test. Before continuing with the channel setup, the physical connection of each sensor was checked. The channel lights on the SCADAS unit had to be green, confirming that the sensor was correctly connected, powered, and recognized by the acquisition system. Channels with connection problems, overloads, or non-working ports were not used.

5.6.4 Channel setup

After verifying the hardware connections, the Channel Setup worksheet was completed. The channel setup table defines how each physical SCADAS input channel is interpreted by Testlab.

The first column activates or deactivates the input channels. Only the channels used in the test were switched on. For each tri-axial accelerometer, three channels were activated. The hammer channel was also activated and selected as the reference channel because the hammer force represents the input of the FRF calculation.

The point column was used to assign each accelerometer channel to the corresponding measurement node. For the accelerometers, the point name must correspond to the physical location where the sensor is installed. For the hammer, the point is updated during the roving-hammer measurement because the excitation point changes from one impact location to the next.

The direction column was used to assign the measurement direction of each channel. The accelerometer directions were converted into the global coordinate system of the experimental geometry. This step was essential because the local axes of the accelerometers may not coincide with the global axes of the structure. If one accelerometer axis was opposite to the global direction, the corresponding negative direction was assigned in Testlab.

The input mode was set to ICP for all accelerometer and hammer channels. The measured quantity was set to acceleration for the accelerometer channels and force for the hammer channel. The actual sensitivity was then entered for each sensor. For the accelerometers, the calibration sensitivity was taken from the sensor calibration sheet and expressed in mV/g. For the hammer, the sensitivity was expressed in mV/N.

5.6.5 Impact scope settings

The Impact Scope settings define the main acquisition parameters of the impact test. The most important parameters are the bandwidth, the number of spectral lines, the frequency resolution, and the acquisition time.

The bandwidth defines the maximum frequency included in the analysis. The number of spectral lines defines the discretization of the frequency axis. Once the bandwidth and the number of spectral lines are selected, Testlab calculates the frequency resolution and acquisition time.

The selected acquisition settings must satisfy two requirements. First, the bandwidth must be high enough to cover the modes of interest. Second, the acquisition time must be long enough to allow the measured response to decay after the hammer impact. If the acquisition time is too short, the response can be truncated and leakage can appear in the FRF. If the acquisition time is unnecessarily long, the useful response may decay early and the measurement can become more affected by background noise.

5.6.6 Impact setup: trigger, bandwidth, and windowing

The Impact Setup worksheet was used to define the trigger, check the input bandwidth, and apply the input and response windows.

5.6.6.1 Trigger setup

The trigger defines the force level at which Testlab starts recording the impact event. The pre-trigger defines a short time interval before the trigger instant, allowing the beginning of the force pulse to be included in the recorded signal.

To define the trigger, the scope was started and the structure was impacted several times. Testlab displayed the free-run force signal and the software-triggered force signal. The free-run signal shows the hammer force as a continuous time signal. The software-triggered signal shows the impact event detected by the trigger.

After several impacts, the suggested trigger settings were applied. Testlab provided the trigger level in volts, the pre-trigger time in seconds, and the input range in volts. The free-run force signal was used to check the impulse and trigger level. The software-triggered force signal was used to verify the pre-trigger. By zooming on one impulse and setting a cursor at zero time, the pre-trigger interval could be inspected.

A correct trigger setting is important because a trigger level that is too low may activate the acquisition due to noise, while a trigger level that is too high may miss valid impacts.

5.6.6.2 Bandwidth check

After the trigger setup, the bandwidth check was performed. This step verifies whether the hammer impact provides sufficient input energy over the frequency range of interest.

The check bandwidth function was started, the structure was impacted once, and the resulting spectra were inspected. Testlab displayed the PSD of the hammer input force and the PSD of the selected accelerometer response. The force PSD is especially important because it shows the frequency content of the hammer impact.

At low frequencies, the hammer force usually contains sufficient energy. At higher frequencies, the input energy decreases depending on the hammer tip and contact duration. Above a certain frequency, the structure may no longer be excited effectively. Therefore, the bandwidth check was used to verify whether the selected hammer tip and acquisition bandwidth were appropriate for the test. The response PSD was also checked to confirm that the structure responded clearly in the frequency range of interest.

5.6.6.3 Windowing

Windowing was then applied to reduce leakage effects in the frequency-domain FRFs. In impact testing, the input force is a short impulse, while the response is a decaying vibration signal. If the response does not decay sufficiently within the acquisition time, leakage can affect the FRF. The windowing worksheet displays six main plots: unwindowed input, unwindowed response, windowed input time signal, windowed response time signal, windowed input PSD, and windowed response PSD.

For the input force, a force-exponential window was used. For the response acceleration, an exponential window was used. The force window was adjusted to retain the hammer impulse and suppress unnecessary signal after the impact. The response exponential window was used to help the measured response decay inside the acquisition record.

The response window improves the clarity of the response PSD and reduces leakage. However, it must be used carefully. If the exponential decay is too strong, it can artificially modify the measured response and affect the apparent damping. Therefore, the window was used only to improve FRF quality without cutting the useful physical response.

5.6.7 Measurement settings and FRF acquisition

After defining the geometry, channels, scope settings, trigger, bandwidth, and windowing, the final measurement settings were checked in the Measure worksheet. In the All Settings area, the acquisition settings, triggering, and windowing parameters were verified. In the FRF settings, the FRF estimator was set to H1. This estimator is suitable for impact testing when the input force is considered cleaner than the measured response and the response may contain noise.

The number of averages was set to three. Therefore, each point and direction was impacted three times, and only the accepted impacts were included in the averaged FRF.

The run-name option was set to hammer-based run name. In this configuration, the run name is based on the hammer point and direction. This is important in a roving-hammer test because the excitation point changes continuously. Before each measurement, the current hammer point and direction were checked to avoid saving data with the wrong name or overwriting previous measurements.

During the measurement, Testlab displayed several plots. These included the input force in time and frequency domains, the acceleration response in time and frequency domains, the instantaneous FRF magnitude and phase, the averaged FRF magnitude and phase, and the coherence function.

Each impact was checked before acceptance. The input force pulse was inspected to confirm that the hit was clean and did not contain a double impact. The force PSD was checked to confirm sufficient input energy. The response and FRFs were checked to ensure that the measurement was not excessively noisy. The coherence was also inspected.

Coherence values close to 1 indicate a reliable input-output relationship. Local drops may appear near antiresonances because the response amplitude is very small in those regions.

The channel status indicators were checked to ensure that all active channels remained in the green range. In addition to these manual checks, Testlab automatically rejected impacts affected by double hit or overload. This procedure was repeated for each node and direction until three acceptable impacts were obtained.

5.6.8 Data viewing and acquisition verification

After acquisition, the Navigator and Data Viewing areas were used to inspect the measured data. The saved FRFs could be selected and plotted to verify the quality of the dataset. This step was useful for checking that the correct runs had been saved, that the point and direction labels were correct, and that the FRFs were suitable for modal identification.

This verification was especially important in the roving-hammer procedure because many measurements are acquired sequentially. A wrong point name, wrong direction, or repeated run name could create errors in the final modal dataset.

5.6.9 Modal data selection and FRF-set preparation

After the acquisition phase, the modal-analysis add-ins were activated. The required add-ins were Modal Analysis and PolyMAX Modal Analysis. Activating these add-ins made additional worksheets available, including Modal Data Selection, Modal Synthesis, Modal Validation, and PolyMAX. In Modal Data Selection, the FRF dataset was prepared for modal identification. A new FRF set was created, named, and saved. The selected FRFs could then be displayed individually or as an FRF sum. The FRF sum was useful because it provides a global view of the resonance peaks in the measured dataset.

In the roving-hammer configuration, the number of excitation coordinates can be larger than the number of response coordinates, because the hammer is moved over many points while the accelerometers remain fixed. When necessary, the FRF matrix was switched using the reciprocity principle. This allowed the data to be arranged in a suitable form for modal identification and mode-shape visualization.

5.6.10 PolyMAX modal identification and modal validation

The PolyMAX workflow was used to identify the modal parameters from the measured FRFs. The main PolyMAX subsections are Band, Stabilization, and Shapes.

In the Band subsection, the previously created FRF set was selected. The FRF sum was displayed, and the frequency band of interest was defined. The selected band depended on the objective of the test. For the beam, the band covered the beam bending and torsional modes. For the low-frequency powertrain analysis, the band focused on rigid-body and mount-controlled modes. For the long-arm structural analysis, a higher-frequency band was selected.

In the Stabilization subsection, the stabilization diagram was generated. The model size could be modified to improve the stability diagram. The resonance peaks were inspected, and stable poles were selected. In Testlab, stable poles are marked with stability indicators. A pole was accepted as a physical mode only when it was stable, located near a visible FRF peak, had a reasonable damping value, and gave a physically meaningful mode shape.

After selecting the stable poles, the corresponding modal frequencies and damping ratios appeared in the mode list. The selected modes were then checked in the Shapes subsection. In this thesis, real mode shapes were used for visualization and comparison. Upper and lower residuals were checked when required. After naming the processing and selecting Calculate, Testlab generated the final modal processing result.

The identified modes were then animated. Mode-shape animation was used to interpret whether each mode corresponded to translation, rotation, bending, torsion, or local structural deformation.

After PolyMAX, the Modal Validation worksheet was used. The active processing created in PolyMAX was selected. The identified mode shapes could then be visualized and exported for further analysis. The Auto-MAC matrix was also created from the active processing. Auto-MAC compares the identified mode shapes with each other. A good Auto-MAC result should show dominant diagonal values and low off-diagonal values. High off-diagonal values may indicate similar mode shapes, insufficient spatial resolution, closely spaced modes, or uncertainty in the modal identification.

The identified modal parameters and mode shapes were finally exported for MATLAB post-processing. This enabled FRF reconstruction, reciprocity checks, Cross-MAC calculation, EMA–Romax comparison, and final mode-pair selection.

Step	**Testlab area**	**Main operation**	**Purpose**
1	New project	Create a new Testlab project	Start the experimental dataset
2	Geometry : Components	Create one experimental component	Represent the tested structure
3	Geometry : Nodes	Enter node names and coordinates	Define measurement locations
4	Geometry : Lines	Connect nodes with lines	Improve mode-shape visualization
5	Hardware setup	Connect accelerometers, hammer, SCADAS, and PC	Prepare acquisition chain
6	Channel Setup	Activate input channels	Select accelerometer and hammer channels
7	Channel Setup	Assign points and directions	Link sensors to the geometry
8	Channel Setup	Define ICP, measured quantity, and sensitivity	Calibrate channels physically
9	Impact Scope	Select bandwidth and spectral lines	Define resolution and acquisition time

10	Impact Setup : Trigger	Define trigger, pre-trigger, and input range	Detect valid impacts
11	Impact Setup : Bandwidth	Check input and response PSDs	Verify excitation bandwidth
12	Impact Setup : Windowing	Apply input and response windows	Reduce leakage
13	Measure	Select H1 estimator and averaging	Prepare FRF acquisition
14	Measure	Use hammer-based run name	Save each impact with correct point and direction
15	Measure	Perform three accepted impacts per point/direction	Obtain averaged FRFs
16	Measure	Check force, response, FRF, coherence, and channel status	Accept or reject each impact
17	Navigator / Data Viewing	Inspect saved FRFs	Verify data quality
18	Modal Data Selection	Create FRF set and display FRF sum	Prepare data for PolyMAX
19	PolyMAX : Band	Select frequency band	Focus on target modes
20	PolyMAX : Stabilization	Select stable poles	Identify physical modes
21	PolyMAX : Shapes	Calculate and animate mode shapes	Interpret modal deformation
22	Modal Validation	Create Auto-MAC and export results	Validate and export modal data

Table 5.2: Summary of the complete Testlab workflow

5.7 MATLAB post-processing environment

MATLAB was used as an independent post-processing environment. The purpose of the MATLAB workflow was to verify and extend the results obtained in Testlab. The main operations performed in MATLAB include FRF import, FRF synthesis, reciprocity checks, Auto-MAC calculation, Cross-MAC calculation, frequency-error computation, Rayleigh damping identification, and preparation of FE/EMA comparison plots.

The MATLAB post-processing routines developed in this work were used to support the experimental modal analysis workflow after data acquisition in Simcenter Testlab. The scripts were organized to perform several complementary tasks: importing experimental and modal data exported from Testlab, visualizing the measurement geometry, selecting specific input–output FRFs, checking reciprocity through cross-inertance comparison, extracting identified modal parameters, estimating proportional Rayleigh damping coefficients, and comparing experimental FRFs with FRFs reconstructed from the identified modal parameters.

The first routine was used for FRF comparison. It loads the exported UNV dataset, allows the user to select the response and excitation coordinates, searches for the corresponding experimental and synthesized FRFs, and plots their magnitude and phase. This was useful for verifying whether the identified modal model reproduced the measured dynamic response.

A second routine was developed for reciprocity verification. In this case, only cross FRFs were selected, meaning that the excitation and response coordinates were different. The script searches for the reciprocal cross-inertance pair, (H_{AB}) and (H_{BA}), and plots their magnitude and phase. Good agreement between the two curves supports the assumptions of linearity and reciprocity in the measured structure.

A third routine was used for proportional damping identification. The modal parameters exported from Testlab were imported, and the natural frequencies and damping ratios were extracted. The Rayleigh damping coefficients (α) and (β) were then estimated using a least-squares formulation. The resulting damping curve was plotted together with the experimental damping ratios and with the individual mass-proportional and stiffness-proportional damping contributions.

Finally, the powertrain post-processing routine combined geometry visualization, FRF selection, modal-parameter extraction, mode-shape animation, FRF synthesis using the identified modal parameters, and experimental–identified FRF comparison. These MATLAB routines were not used to replace the modal identification performed in Testlab, but to verify, interpret, and present the experimental results in a clearer and more controlled way.

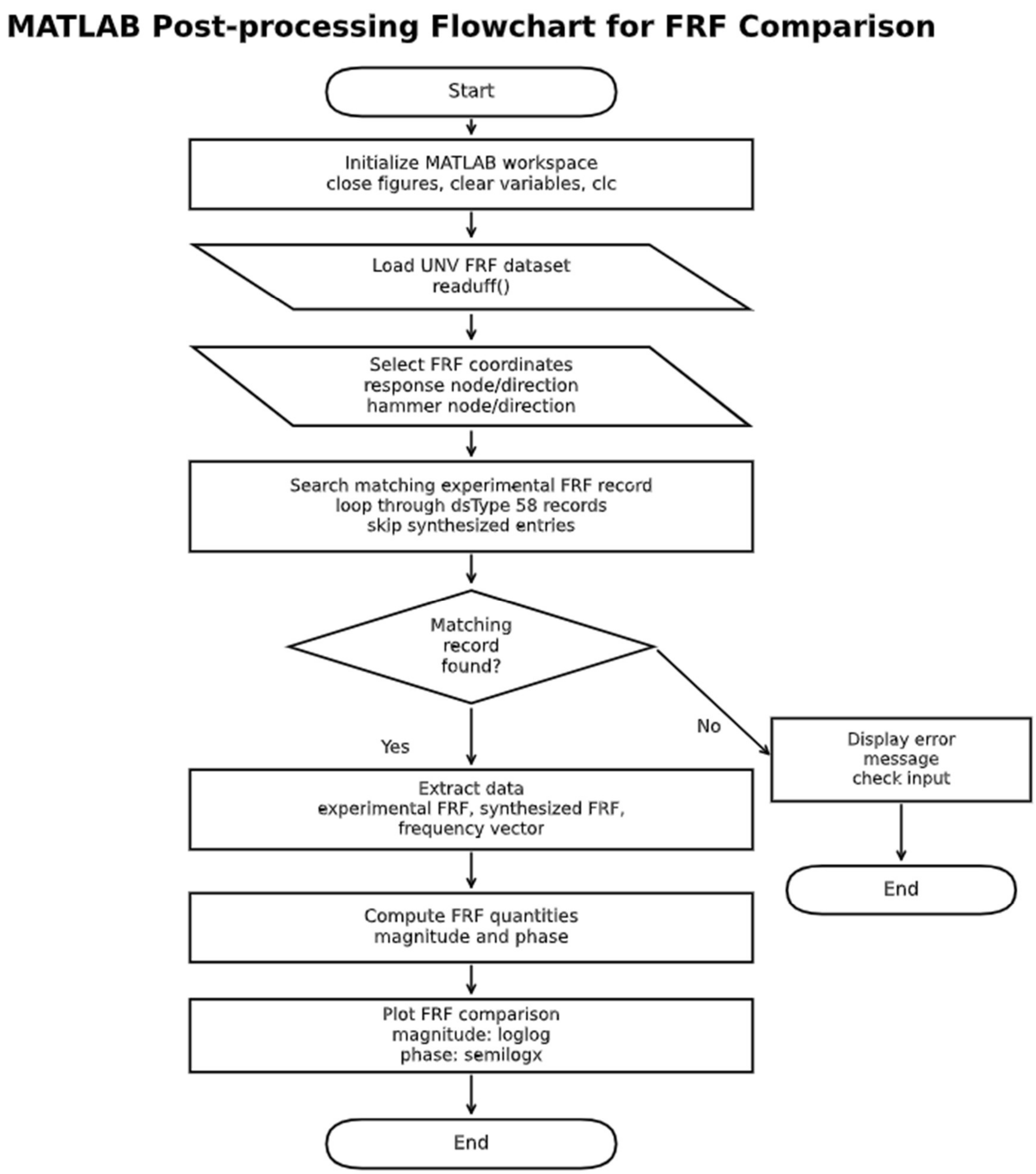

Figure 5.5: Flowchart of the MATLAB FRF comparison routine

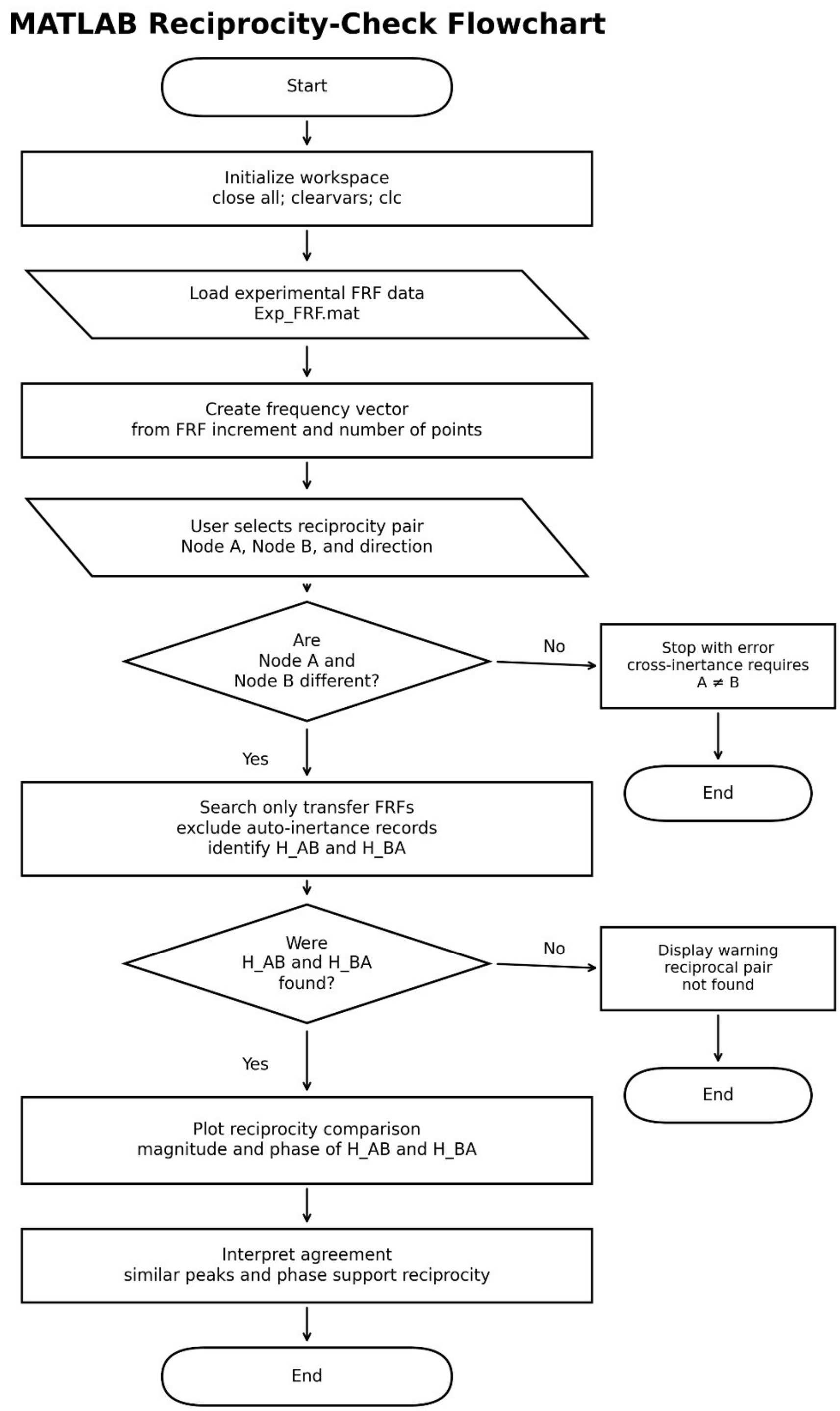

Figure 5.6: Flowchart of the MATLAB reciprocity-check routine.

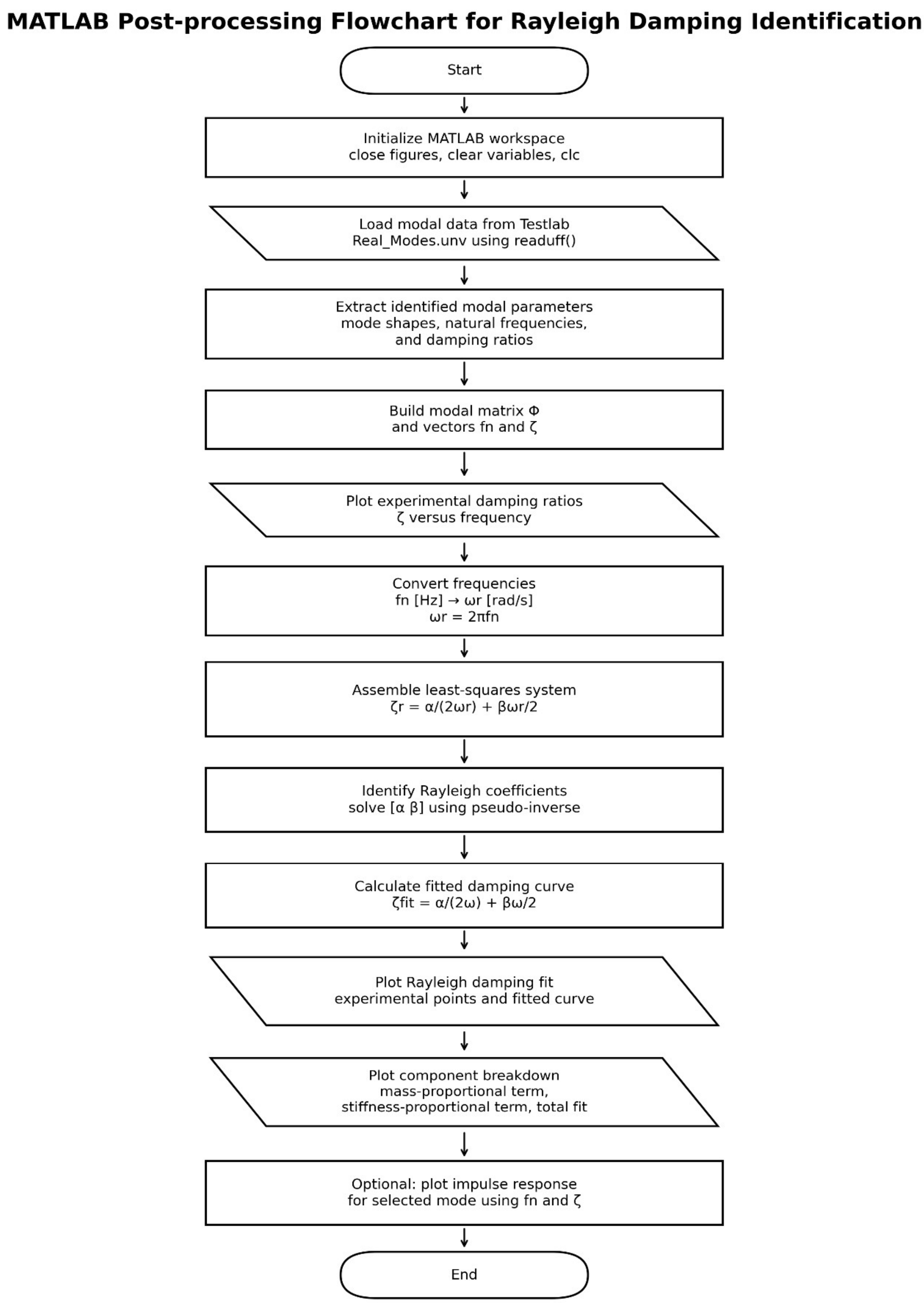

Figure 5.7: Flowchart of the MATLAB post-processing routine used for Rayleigh damping identification.

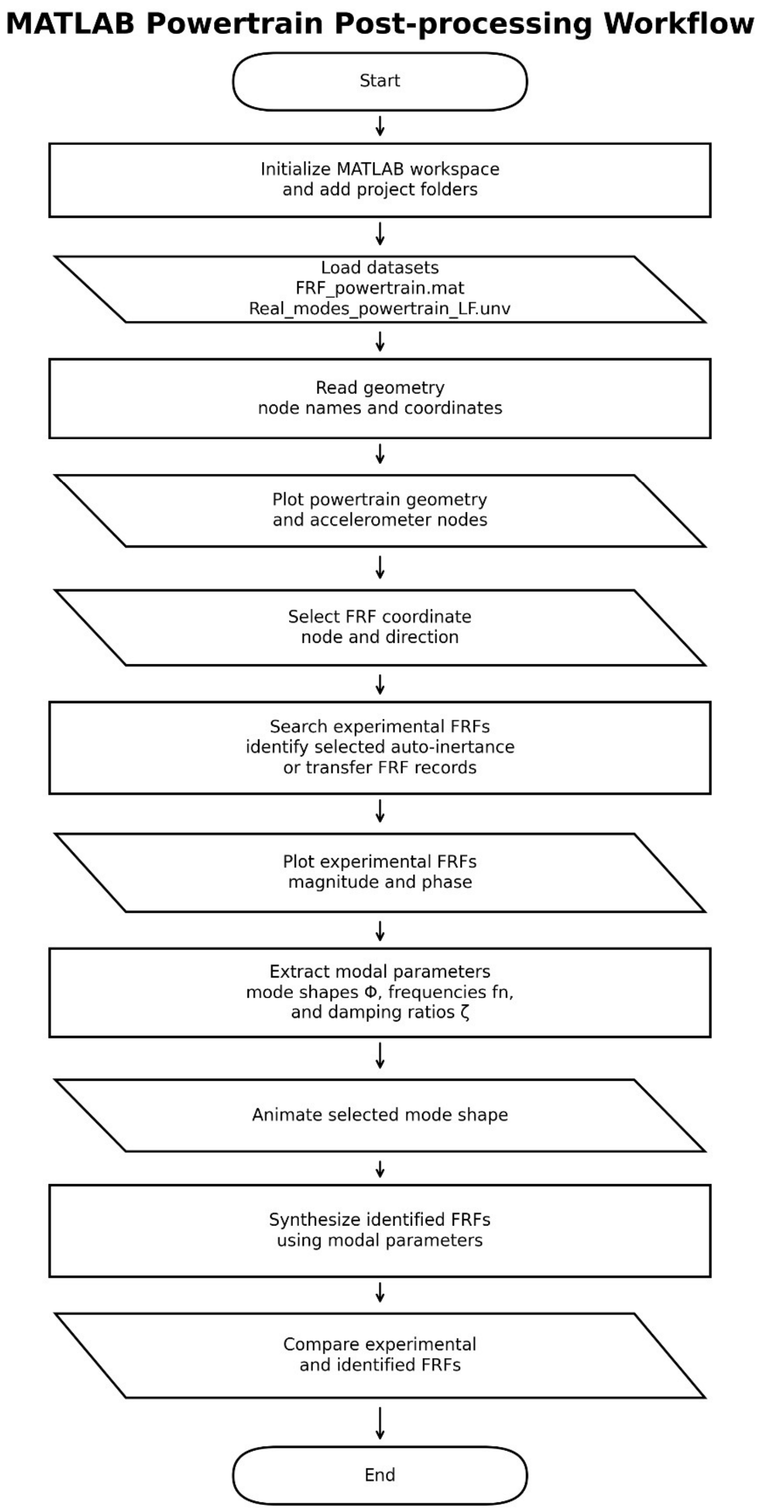

Figure 5.8: Flowchart of the MATLAB powertrain post-processing workflow.

5.7.1 Exported Testlab data structure

After the acquisition and modal identification steps in Simcenter Testlab, the experimental data were exported for independent MATLAB post-processing. The purpose of this export was to make the Testlab results directly accessible in MATLAB, so that the FRFs, synthesized FRFs, modal parameters, mode-shape vectors, and metadata could be checked, reorganized, plotted, and used for correlation with the numerical model.

Three main types of exported files were used in the post-processing workflow:

1. a UNV file containing the experimental and synthesized FRFs;
2. a UNV file containing the identified real modes;
3. a MAT file containing the experimental FRFs and their metadata in MATLAB structure format.

The UNV files were read using a MATLAB UFF/UNV reading function.

```
addpath('C:\Users\d016313\OneDrive - Politecnico di Torino\Desktop\LMS_Projects\EMA_Beam_2025-11-27\github_repo')

data = readuff('Real_Modes.unv');
```

After import, the content of the UNV file is stored as an ordered cell array. Each cell, or page, contains a different dataset exported by Testlab. The first pages usually contain project information, geometry information, and node information. The following pages contain the experimental FRFs, synthesized FRFs, or modal data, depending on the type of exported file.

This organization is important because the exported file is not a single matrix. It is a structured sequence of pages. Each page must be interpreted using its dataset type and its internal fields. Therefore, before extracting FRFs or mode shapes, the file structure must be inspected to identify which pages contain metadata, which pages contain node information, and which pages contain the actual measured or synthesized data.

5.7.2 Reading the experimental and synthesized FRF UNV file

The experimental and synthesized FRFs were exported from Testlab in UNV format. This file contains both the measured FRFs and the FRFs synthesized from the identified modal model. In MATLAB, the UNV file was read using the UFF reading function, which stores the content in a cell array, for example:

$$data\_s\{1, i\}$$

where i is the index of the page in the exported UNV file.

The first pages of this file contain general information about the Testlab project. This information can include the model name, the Testlab application name, the project name, the creation time, the creation date, the saving time, and the dataset type. The dataset type is important because it identifies the content of each page.

For example, the first data page may include general project metadata such as the model name and the Testlab project name. Another early page contains the node information. This node page stores the node names and, when available, the node coordinates. The node coordinates are necessary because the FRFs and mode shapes must be associated with the correct physical locations on the experimental geometry.

After the initial metadata and geometry pages, the file contains the FRF pages. In this thesis, the experimental FRFs and synthesized FRFs are both present in the same exported file. Each FRF is stored in one page. Therefore, the file contains a repeated structure: a page containing an experimental FRF is followed later by a page containing the corresponding synthesized FRF, or the experimental and synthesized FRFs are stored in two ordered groups with the same page structure.

This is useful because the same input-output coordinate can be compared directly between the experimental FRF and the synthesized FRF. The experimental FRF represents the measured dynamic response, while the synthesized FRF represents the response reconstructed by Testlab from the identified modal parameters.

5.7.3 Structure of each FRF page in the UNV file

Each FRF page contains both the numerical FRF values and the metadata required to identify the corresponding input-output function. The most important fields are the measured data vector, the FRF name, the frequency-axis information, and the channel information.

The measured data vector contains all the complex FRF values for that specific input-output pair. This vector gives the response quantity divided by the reference force over the exported frequency range. In this thesis, the response quantity is acceleration and the input quantity is force. Therefore, the FRFs are inertance functions.

The FRF name is also important because it identifies the response point, response direction, reference point, and reference direction. In the roving-hammer configuration, the accelerometer channels are the response channels, while the hammer channel is the reference channel. Therefore, the FRF name allows each function to be connected to the corresponding accelerometer location and hammer excitation direction.

Each FRF page also contains frequency-axis information. This includes the frequency start value, the frequency increment, the number of frequency values, and the frequency unit. From these values, the frequency vector can be reconstructed as:

$$f_i = f_{start} + (i - 1)\Delta f$$

Where f_i is the frequency at line i, f_{start} is the starting frequency, and Δf is the frequency increment.

The quantity information describes the physical units of the exported data. The frequency axis is expressed in hertz. The FRF values are expressed as acceleration divided by force. Depending on the export settings, the acceleration may be stored in g, so the FRF unit may appear as g/N. Testlab also stores unit-system information, such as MKS units.

The general structure of one FRF page can be summarized as follows.

Field / information	Meaning	Use in MATLAB
Measured data vector	complex FRF values for one input-output pair	FRF magnitude and phase plotting
FRF name	name of the function, including response and reference information	selection of the required FRF
Response channel	accelerometer channel	identifies response node and direction
Reference channel	hammer channel	identifies input/reference coordinate
Frequency start value	first frequency value	reconstruction of frequency vector
Frequency increment	spacing between frequency lines	reconstruction of frequency vector
Number of values	number of frequency points	size of FRF vector
Frequency quantity	hertz label and frequency unit	axis labelling
FRF quantity	acceleration/force information	confirms inertance type
Unit information	Testlab unit-system information	physical interpretation of values

Table 5.3: Internal structure of one FRF page in the UNV file

The same page structure is repeated for the experimental FRFs and for the synthesized FRFs. This repetition makes it possible to write MATLAB routines that automatically search for a specific FRF name, find the corresponding experimental and synthesized functions, and plot them together.

5.7.4 Reading the modal UNV file

A second UNV file was exported from Testlab to store the identified real modes. This file contains the modal properties obtained from the PolyMAX processing. Similar to the FRF UNV file, the modal UNV file is organized as a sequence of pages.

The first pages of the modal UNV file have the same general role as in the FRF UNV file. They contain project information, node information, and geometry-related data. After these initial pages, the modal pages appear. These pages contain the modal properties and mode-shape vectors.

The pages containing modal information can be identified from their dataset type. In the exported modal file, the modal-property pages contain the identified modes. Each modal page corresponds to one mode or one residual term. Therefore, the modal file is read page by page, and the pages with modal data are used to extract the natural frequencies, damping ratios, and eigenvector components. The main information contained in each modal page is:

- processing name;
- mode number;
- natural frequency;
- damping ratio;
- eigenvector components in the measured directions.

The processing name identifies the PolyMAX processing from which the mode was exported. This is important when several modal processing results exist in the same Testlab project. The mode number identifies the mode inside the selected processing. The natural frequency and damping ratio are the modal parameters identified by Testlab.

5.7.5 Modal parameters and eigenvectors in the modal UNV file

The modal UNV file contains the information required to build the experimental mode-shape matrix used in the MATLAB post-processing workflow. For each exported mode, the file contains the mode frequency, damping ratio, and eigenvector components.

The eigenvector components are stored by node and by direction. In the exported data, the modal components can be interpreted as the modal displacement or modal response components in the three spatial directions. These components are used to create the experimental modal matrix:

$$\Phi_{EMA}$$

where each column represents one experimental mode and each row represents one measured degree of freedom.

For example, if the experimental comparison uses three tri-axial accelerometers, the mode-shape vector of each mode contains nine translational components:

$$\phi_r = [120_X \quad 120_Y \quad 120_Z \quad 210_X \quad 210_Y \quad 210_Z \quad 305_X \quad 305_Y \quad 305_Z]^T$$

where r is the mode number. Repeating this extraction for all selected modes gives the complete experimental mode-shape matrix.

$$\Phi_{EMA} = [\phi_1 \quad \phi_2 \quad \cdots \quad \phi_m]$$

where m is the number of identified modes.

The size of Φ_{EMA} depends on how the FRF dataset is arranged before exporting the modal results. In a roving-hammer test with fixed accelerometers, if the FRF matrix is used in its original form, the rows of Φ_{EMA} correspond to the measured response DOFs, i.e. mainly the fixed accelerometer locations and directions. If the FRF matrix is switched in Simcenter Testlab by exploiting the reciprocity assumption, the hammer excitation coordinates can be treated as reciprocal response coordinates. In this configuration, the exported mode-shape vector can be defined over a larger set of spatial coordinates, corresponding to the hammer impact points and directions, provided that these coordinates are included in the switched/reciprocal modal dataset. Therefore, the reciprocity switch does not create new physical sensor measurements; rather, it rearranges the measured FRFs so that the roving-hammer locations can contribute to the spatial definition of the mode shapes.

In Simcenter Testlab, switching the FRF matrix relies on the reciprocity assumption, which is generally valid for linear passive structures.

In the modal UNV file, the three directional eigenvector components are stored separately. These components correspond to the X, Y, and Zdirections of the exported node. In MATLAB, these values are extracted and assembled according to the same DOF order used for the Romax eigenvectors. This is essential because MAC comparison requires the experimental and numerical vectors to have the same DOF order and the same coordinate convention.

Modal-file item	Meaning	Use in MATLAB
Processing name	name of the PolyMAX processing	identifies the modal processing
Mode number	mode index in the processing	mode ordering
Mode frequency	identified natural frequency	frequency comparison
Damping ratio	modal damping identified by Testlab	damping interpretation and Rayleigh fitting
X-component	modal component in X direction	construction of mode-shape vector
Y-component	modal component in Y direction	construction of mode-shape vector
Z-component	modal component in Z direction	construction of mode-shape vector

Table 5.4: Modal information extracted from the modal UNV file

This modal export is therefore the main source for the experimental frequencies, damping ratios, and mode-shape vectors used in the MAC calculations.

5.7.6 Reading the FRF MAT file

In addition to the UNV files, the FRFs were also exported in MAT format. This file can be loaded directly in MATLAB without using a UNV reader. The exported MAT file is organized as a MATLAB structure. In this thesis, the MAT file was organized as a 1×1structure containing three main fields:

$$x\_values$$
$$y\_values$$
$$function\_record$$

The field x_values contains the frequency-axis information. This includes the starting value, the frequency increment, the number of values, and the physical quantity associated with the x-axis. Since the x-axis represents frequency, the quantity label is hertz.

The field y_values contains the FRF data values. These values include the exported experimental FRFs. The data are stored as a matrix in which the rows correspond to frequency lines and the columns correspond to different FRFs. Therefore, the number of columns indicates the number of exported FRFs, and the number of rows indicates the number of frequency points.

The field function_record contains the metadata associated with each FRF. This field is essential because it links the numerical FRF values stored in y_values to their physical meaning. Without function_record, the FRF matrix would only contain numerical values, but the response point, excitation point, direction, method, and run name would not be directly known.

The MAT file structure can be summarized as follows.

MAT-file field	Main content	Meaning
x_values	frequency-axis definition	defines the frequency vector
y_values	FRF value matrix	contains the complex FRF data
function_record	FRF metadata	identifies each FRF physically

Table 5.5: Main fields of the exported FRF MAT file

The frequency vector is reconstructed from the x_values field using:

$$f_i = f_{start} + (i-1)\Delta f$$

where f_{start} is the start value and Δf is the frequency increment. The FRF matrix is extracted from the y_values field. Each column corresponds to one FRF exported from Testlab. The corresponding name and metadata of each column are read from function_record.

5.7.7 Frequency-axis and FRF-value fields in the MAT file

The x_values field contains the information required to reconstruct the frequency axis. The start value is usually zero or the first exported frequency line. The increment represents the frequency spacing between consecutive lines. The number of values gives the total number of frequency samples. The quantity subfield inside x_values provides the label and unit of the x-axis. In this case, the label is frequency and the unit is hertz. Additional information may indicate that the data were saved by Testlab using the MKS unit system.

The y_values field contains the actual FRF values. The values are stored in a numerical array. Each column contains all frequency-line values for one FRF. Therefore, if the file contains N_f frequency lines and N_H exported FRFs, the FRF matrix has the size of $N_f \times N_H$. Where N_f is the number of frequency values and N_H is the number of FRFs. The quantity subfield inside y_values describes the physical quantity of the FRF values. Since the measured response is acceleration and the reference is force, the exported FRFs are inertance functions. Depending on the export settings, the response acceleration may be expressed in g, giving units such as g/N.

Field	Subfield / item	Interpretation
x_values	start value	first frequency value
x_values	increment	frequency discretization
x_values	number of values	number of frequency lines
x_values.quantity	label and unit	frequency in Hz
y_values.values	numerical values	complex FRF matrix
y_values.quantity	label and unit	inertance, acceleration/force
y_values.info	unit-system information	Testlab export information

Table 5.6: Interpretation of x_values and y_values

This organization allows MATLAB to reconstruct the complete FRF dataset directly from the MAT file.

5.7.8 Function-record information in the MAT file

The function_record field stores the metadata for each exported FRF. This field is particularly important because it identifies each column of the FRF matrix. The name subfield contains the FRF names. The size of this cell array corresponds to the number of exported FRFs.

The type field identifies the function type. In this thesis, the functions are FRFs. The creation time and last modification time provide metadata about when the data were generated and saved.

The primary_channel field identifies the response channel used for each FRF. In the present experimental setup, the primary channel corresponds to the accelerometer channel. The reference_channel field identifies the reference channel, which corresponds to the impact hammer. This distinction is important because FRFs are defined as response over reference force.

The memo field can contain additional annotations, such as the accelerometer number and direction. This information helps verify whether each FRF has been assigned to the correct measurement coordinate.

The frf subfield contains information related to the FRF estimation. The method field indicates the estimator used to calculate the FRF. In this thesis, the estimator was H1. The scaling field indicates the scaling applied to the FRF. In the exported files used for this work, the scaling was set to none.

The export properties and annotation fields contain project and run information. In particular, the run name is important because it identifies the hammer point and hammer direction used during the roving-hammer measurement. This information was used to check that the FRF was saved with the correct excitation coordinate.

function_record item	Meaning	Use
name	FRF names	identifies each exported FRF
type	function type	confirms that the function is an FRF
creation_time	creation time	metadata
last_modification_time	last modification time	metadata
primary_channel	accelerometer channel	identifies response coordinate
reference_channel	hammer channel	identifies reference/input coordinate
memo	accelerometer number and direction	additional coordinate annotation
frf.method	FRF estimator	confirms H1 method
frf.scaling	scaling option	confirms scaling setting
TL_export_properties_annotation	Testlab export annotations	stores project and run information
project_name	Testlab project name	identifies source project
run_name	hammer point and direction	identifies excitation coordinate

Table 5.7: Main information stored in function_record

The function_record field therefore provides the link between the numerical FRF matrix and the physical test configuration. It allows a MATLAB script to search for a specific FRF by name, identify its response and reference coordinates, and compare it with the corresponding synthesized FRF or reciprocal FRF.

5.7.9 Use of the exported files in MATLAB post-processing

The exported UNV and MAT files were used together in the MATLAB post-processing workflow. The FRF UNV and MAT files provided the measured and synthesized FRFs, while the modal UNV file provided the identified modal parameters and mode-shape vectors.

The first use of these files was FRF visualization. The FRF names stored in the UNV pages or in function_record.name were used to select a specific input-output function. The corresponding frequency vector was reconstructed from the frequency-axis information, and the FRF magnitude and phase were plotted.

The second use was experimental/synthesized FRF comparison. The experimental FRF and the synthesized FRF corresponding to the same input-output pair were selected and plotted together. This comparison verified whether the modal model identified in Testlab reproduced the measured dynamic behaviour.

The third use was reciprocity verification. By using the FRF names, MATLAB selected reciprocal cross-FRF pairs, for example:

H_{AB} and H_{BA}

These functions were then compared in magnitude and phase. Good agreement between reciprocal FRFs supports the linearity and consistency of the measured data.

The fourth use was construction of the experimental mode-shape matrix. The modal UNV file provided the eigenvector components for the identified modes. These components were extracted at the selected nodes and directions and assembled into the matrix: Φ_{EMA} This matrix was then used to calculate the Auto-MAC matrix for the experimental modes.

The fifth use was EMA–Romax correlation. The experimental mode-shape matrix extracted from the Testlab modal export was compared with the numerical mode-shape matrix extracted from Romax. Before computing MAC, the DOF order and coordinate directions were checked to ensure that both matrices were expressed in the same reference system.

The exported file structure therefore made the MATLAB workflow traceable. Each FRF could be identified by its response point, response direction, reference point, and reference direction. Each mode could be identified by its frequency, damping ratio, and eigenvector components. This traceability was essential for reliable FRF validation, reciprocity checking, modal validation, and EMA–Romax correlation.

Exported file	Main structure	Main content	Use in MATLAB
Experimental/synthesized FRF UNV	ordered pages/cells	metadata, node information, experimental FRFs, synthesized FRFs	FRF plotting and FRF validation
Modal UNV	ordered pages/cells	modal frequencies, damping ratios, eigenvector components, residuals	construction of Φ_{EMA}, Auto-MAC, Cross-MAC
FRF MAT file	1×1MATLAB structure	x_values, y_values, function_record	direct access to FRF matrix and metadata
MAP file, when available	node mapping text/table	correspondence between exported node IDs and Testlab node names	node identification and DOF mapping

Table 5.8: Summary of exported Testlab file structures

This exported-data structure allowed the Testlab results to be used outside the Testlab environment. Testlab was used for acquisition and PolyMAX modal identification, while MATLAB was used to inspect the exported data, reconstruct FRFs, verify reciprocity, calculate MAC matrices, and perform the final experimental-numerical correlation.

6 Cantilever Beam: Method Validation

6.1 Purpose of the preliminary beam study

Before applying the experimental procedure to the electric powertrain, a preliminary validation activity was carried out on a cantilever beam. The beam was selected as a controlled test structure because its modal behaviour is simpler than that of a complete powertrain and can be interpreted using three complementary approaches: analytical beam theory, finite element simulation, and EMA.

The purpose of this chapter is not only to report the beam test results, but also to demonstrate the development of the complete experimental-numerical workflow used later for the powertrain. The cantilever beam was therefore used as a methodological benchmark. Through this case, the acquisition hardware, the Testlab setup, the roving-hammer strategy, the modal parameter extraction procedure, the MATLAB post-processing tools, and the FE/EMA correlation procedure were verified under controlled conditions.

6.2 Test specimen and boundary condition

The test specimen consisted of a rectangular steel beam arranged in a cantilever configuration. One end of the beam was clamped, while the other end was free. The fixed boundary condition was obtained by sandwiching the beam end between a base plate and a reinforced fixture. The complete clamping assembly was then fixed to the laboratory workbench using manual C-clamps.

This boundary condition was intended to approximate an ideal clamped-free configuration. However, from an experimental point of view, a real clamped boundary always has a finite compliance. Small rotations, local slips, imperfect contact, and flexibility of the fixture can reduce the effective stiffness of the system. For this reason, the beam test was also used to study the influence of boundary-condition flexibility on the correlation between numerical and experimental modal results.

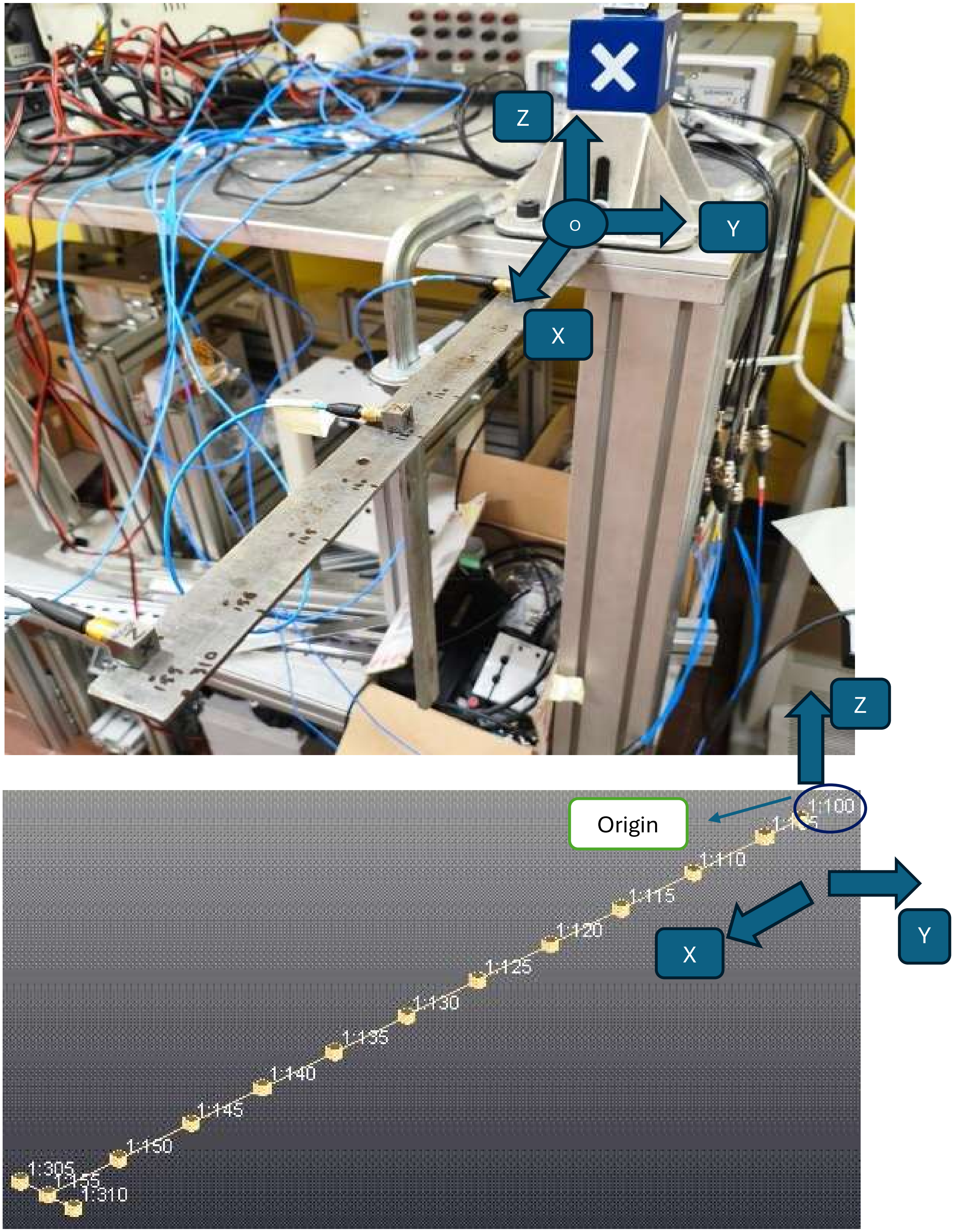

Figure 6.1: Beam experimental setup and Test.Lab geometry

6.3 Geometry definition

A simplified one-dimensional geometry was defined in Testlab to represent the beam. The main nodes were distributed along the longitudinal axis of the beam, while two additional off-axis nodes were introduced at the free end to capture torsional behaviour. This node configuration allowed both bending and torsional deformation patterns to be represented during mode-shape visualization.

Node	X [mm]	Y [mm]	Z [mm]
100	0	0	0
105	20	0	0
110	60	0	0
115	100	0	0
120	140	0	0
125	180	0	0
130	220	0	0
135	260	0	0
140	300	0	0
145	340	0	0
150	380	0	0
155	420	0	0
305	420	-15	0
310	420	15	0

Table 6.1: Node coordinates of the beam

Nodes 115, 135, and 305 were selected as accelerometer reference locations. Node 305 was located close to the free end of the beam, where the displacement of the first bending mode is expected to be high. Nodes 115 and 135 were located along the beam span and provided additional spatial information for the identification of higher-order modes.

6.4 Instrumentation and channel mapping

The experimental setup was composed of an LMS SCADAS Mobile acquisition system, a PCB 086C03 instrumented impact hammer, three PCB 356A45 tri-axial accelerometers, a workstation running Testlab, and the required BNC cables and ICP signal conditioning.

Component	SCADAS ports	Location / function
Accelerometer 1	1, 2, 3	Beam tip, node 305
Accelerometer 2	4, 5, 6	Node 115
Accelerometer 3	9, 10, 11	Node 135
Impact hammer	8	Roving excitation input

Table 6.2: Accelerometers position & dedicated SCADAS port

Two input ports of the SCADAS unit, ports 7 and 14, were identified as non-functional during the preliminary activity. These ports were excluded from the final channel mapping. All accelerometer channels were configured as ICP inputs. The measured quantity was defined as acceleration for the accelerometers and force for the hammer.

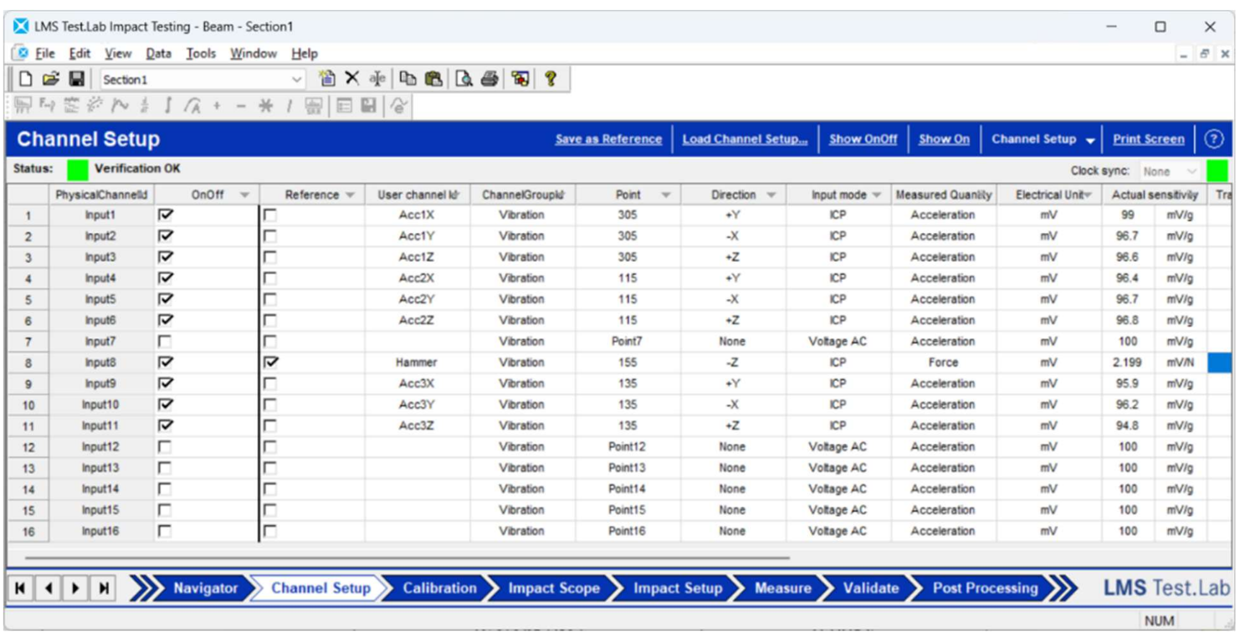

Figure 6.2: Testlab channel setup

6.5 Roving-hammer acquisition strategy

The experimental activity was carried out using a roving-hammer strategy. The accelerometers remained fixed at nodes 115, 135, and 305, while the hammer was moved between the excitation points. This approach was selected instead of a roving-accelerometer strategy because the beam is lightweight and therefore sensitive to accelerometer mass loading. The beam was excited using a roving-hammer strategy. Node 100 was not impacted because it was located under the clamp and was not accessible for hammer excitation.

For the accessible nodes, the main excitation direction was the vertical direction, and each point was impacted three times to improve repeatability. Horizontal excitation was also applied to the beam-span nodes, again with three repetitions where access allowed it. At the three free-end nodes, horizontal excitation was performed only once because of practical hammering limitations and because these points share the same longitudinal and vertical coordinates.

Excitation along the beam axis was performed only once at the central free-end node, since this was the only suitable location for applying an impact in the longitudinal direction. Therefore, the amount of data collected was not identical in all directions, and the modal identification is expected to be more reliable for the vertical bending modes than for the horizontal and longitudinal/torsional responses.

Node ID	Position description	Excited direction(s)	Number of repetitions	Comment
100	Clamped/root node	Not excited	0	Located under the clamp
105, 110, 115, 120, 125, 130, 135, 140, 145, 150	Accessible beam-span nodes	Vertical and horizontal	3 per direction	Main excitation grid
155, 305, 310	Free-end nodes	Vertical	3	Used for bending-mode excitation

155, 305, 310	Free-end nodes	Horizontal	1	Limited accessibility at the free end
155	Central free-end node	Longitudinal / beam-axis direction	1	Only suitable point for longitudinal excitation

Table 6.3: Beam roving-hammer excitation plan

The three measurements were averaged in order to improve repeatability and reduce random noise. Measurements affected by double hits, overload, poor input level, or poor coherence were rejected and repeated. During acquisition, Testlab displayed the force input, the acceleration response, the instantaneous FRF, the averaged FRF, and the coherence function.

The hammer-tip selection for the beam was made according to the target frequency range and the expected stiffness of the structure. Since the beam validation test aimed to identify several bending and torsional modes up to 1500 Hz, the selected tip had to provide sufficient bandwidth to excite the higher modes. According to the PCB hammer manual, a stiffer tip is recommended when a higher-frequency response is required, while a softer tip is more suitable for lower-frequency excitation. For this reason, the selected hammer tip, metallic in this case, was considered appropriate for the beam validation test, where the objective was not only to excite the first bending mode but also to identify higher-order modes within the selected bandwidth.

6.6 Modal parameter extraction using PolyMAX

After acquisition, the FRFs were processed in the Testlab modal analysis environment. The PolyMAX estimator was used to identify the modal parameters within the frequency bandwidth from 0 to 1500 Hz. The identification process was based on the stabilization diagram. Figure 6.3 is plotted based on the FRF sum, despite not having a physical meaning, it gives the opportunity to see all the peaks at a single plot.

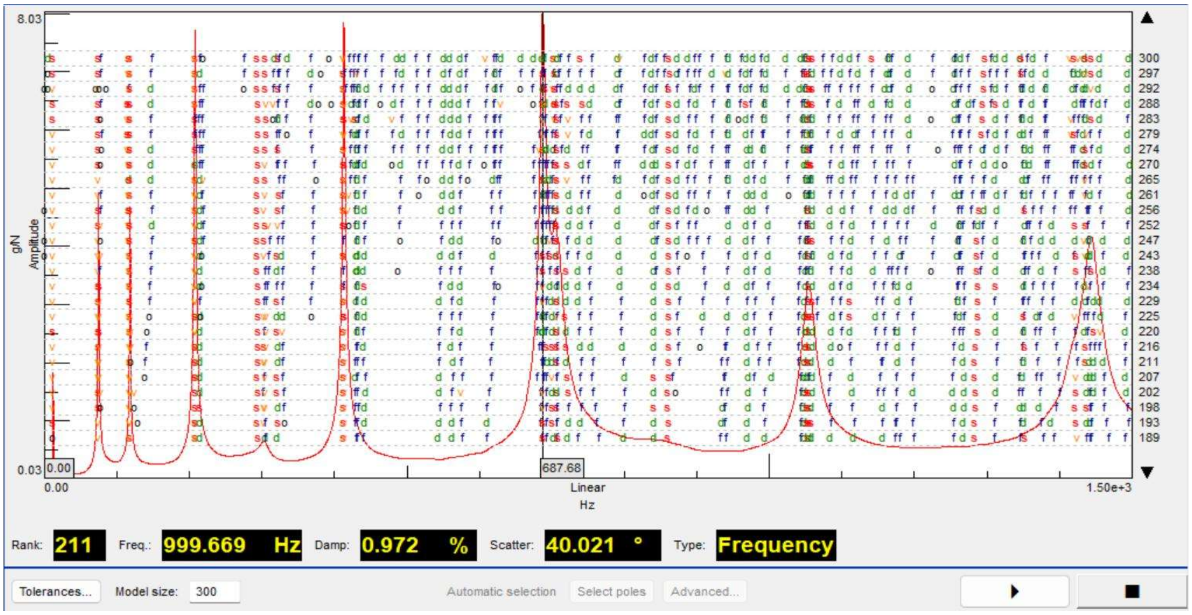

Figure 6.3: PolyMAX stabilization diagram used for pole identification

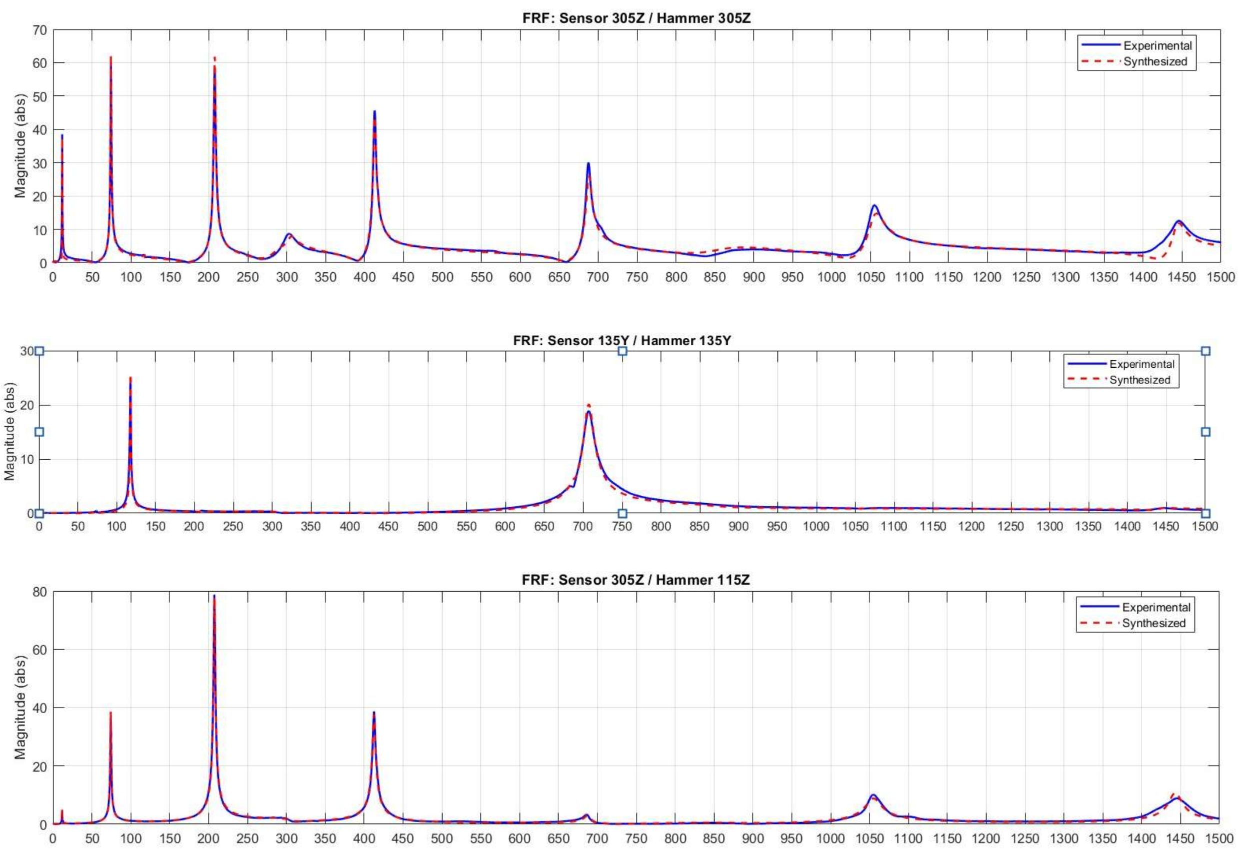

Figure 6.4: Testlab synthesized Frequency Response Function (FRF) via Experimental FRF in linear scale to compare with poles found in stabilization diagram

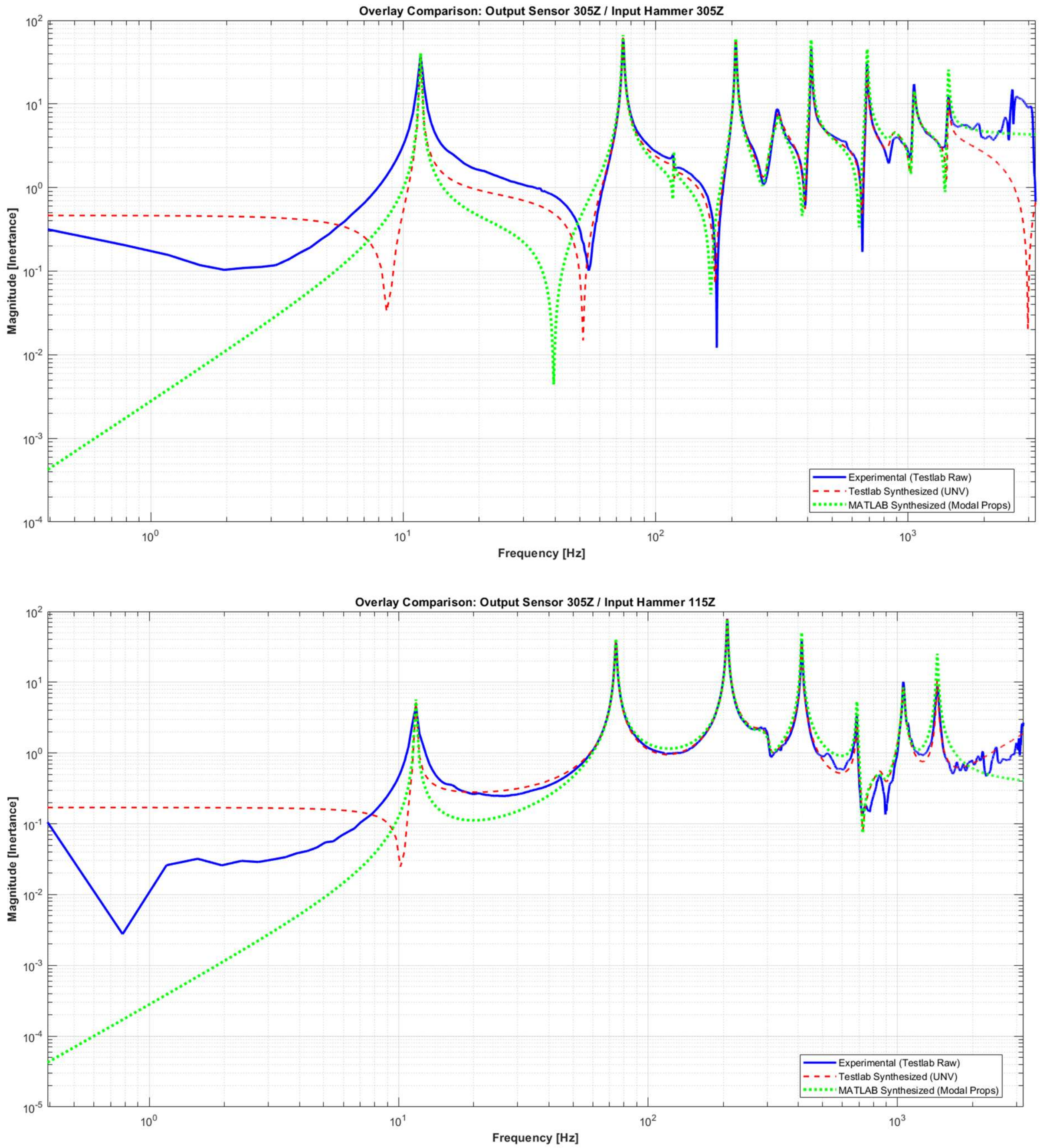

Figure 6.4: Testlab synthesized Frequency Response Function (FRF), Experimental FRF and Matlab synthesized FRF overlay in logarithmic scale for Auto & Cross inertances

6.6.1 Analytical Euler–Bernoulli beam model

For the preliminary beam validation, an analytical Euler–Bernoulli cantilever-beam model was used as a reference for the bending modes. The beam was modelled as a uniform rectangular steel beam with length

$$L = 0.436 \text{ m}$$

and rectangular cross-section dimensions

$$a = 30 \text{ mm}, b = 3 \text{ mm}$$

where $a$is the beam width and $b$is the beam thickness. The material properties used in the initial analytical model were

$$E = 210 \times 10^9 \text{ Pa}, \rho = 7850 \text{ kg/m}^3$$

The cross-sectional area and mass per unit length were calculated as

$$S = ab$$

$$\mu = \rho S$$

For vertical bending, the second moment of area was calculated using the weak bending axis:

$$I_v = \frac{ab^3}{12}$$

For horizontal bending, the second moment of area was calculated using the strong bending axis:

$$I_h = \frac{ba^3}{12}$$

Therefore, the analytical natural angular frequencies for vertical bending were obtained from

$$\omega_{n,v} = \lambda_n^2 \sqrt{\frac{EI_v}{\mu L^4}}$$

while the analytical natural angular frequencies for horizontal bending were obtained from

$$\omega_{n,h} = \lambda_n^2 \sqrt{\frac{EI_h}{\mu L^4}}$$

where $\lambda_n$is the dimensionless characteristic constant of the clamped-free Euler–Bernoulli beam. These constants are obtained from the cantilever-beam frequency equation:

$$\cos(\lambda_n)\cosh(\lambda_n) + 1 = 0$$

For the first modes, the values are

$$\lambda_1 = 1.875, \lambda_2 = 4.694, \lambda_3 = 7.855$$

The natural frequencies in hertz were then calculated as

$$f_{n,v} = \frac{\omega_{n,v}}{2\pi}$$

and

$$f_{n,h} = \frac{\omega_{n,h}}{2\pi}$$

The analytical mode shape of a clamped-free Euler–Bernoulli beam can be written as

$$\phi_n(x) = \cosh(\beta_n x) - \cos(\beta_n x) - \sigma_n[\sinh(\beta_n x) - \sin(\beta_n x)]$$

where

$$\beta_n = \frac{\lambda_n}{L}$$

and

$$\sigma_n = \frac{\cosh(\lambda_n) + \cos(\lambda_n)}{\sinh(\lambda_n) + \sin(\lambda_n)}$$

The coordinate $x$is measured from the clamped end to the free end of the beam. The same analytical mode-shape expression is valid for both vertical and horizontal bending. The difference between the two bending directions is not the shape function itself, but the bending stiffness EI, which depends on the corresponding second moment of area. Therefore, vertical bending uses $I_v = ab^3/12$, while horizontal bending uses $I_h = ba^3/12$.

These analytical frequencies and mode shapes were used as a first reference for the beam validation. The analytical model was then compared with the 3D Nastran model and with the experimental EMA results. The Euler–Bernoulli model provides a reliable reference for bending-dominated modes, but it does not predict torsional modes. For this reason, no analytical torsional frequency was reported, and torsional behaviour was interpreted using the 3D finite element model and the experimental mode shapes.

6.6.2 MSC Nastran finite element model

For the numerical comparison, a three-dimensional finite element model of the beam was prepared in MSC Nastran format and solved using SOL 103 normal modes analysis. The objective of this model was to provide a numerical reference for the experimental EMA modes and to check the accuracy of the simplified analytical Euler–Bernoulli beam model.

The beam was modelled with its real rectangular geometry. The longitudinal direction of the beam was defined along the X-axis. The model length was approximately:

$$L = 436 \text{ mm}$$

and the cross-section was approximately:

$$30 \text{ mm} \times 3 \text{ mm}$$

The finite element mesh was generated using three-dimensional CHEXA hexahedral solid elements. The final model contained 3212 grid points and 1450 CHEXA elements.

The mesh was regular along the beam length and across the beam width. The longitudinal discretization was approximately 3 mm, giving a sufficiently fine mesh for the frequency range considered in the beam validation. Since the objective of the model was modal-frequency and mode-shape comparison rather than local stress analysis, this discretization was considered adequate for the global bending and torsional modes investigated in this thesis.

The material was defined as linear elastic isotropic steel. The properties used in the initial finite element model were:

$E = 210\ \mathrm{kN/mm^2}$

$\nu = 0{,}3$

$\rho = 7{,}85 \times 10^{-9}\ \mathrm{tonne/mm^3} = 7850\ \mathrm{kg/m^3}$

where $E$is Young’s modulus, $\nu$is Poisson’s ratio, and $\rho$is the density.

The boundary condition was applied at the left end of the beam in order to reproduce the clamped-free configuration. The nodes of the clamped section were constrained using SPC constraints, with all six degrees of freedom fixed:

$$u_x = u_y = u_z = \theta_x = \theta_y = \theta_z = 0$$

In the Nastran model, this corresponds to fixing degrees of freedom 1 to 6 at the constrained end-section nodes. This boundary condition represents the ideal clamped support used in the analytical and numerical comparison. In the real experiment, however, the clamp has finite stiffness, and this difference is one of the reasons why the experimental frequencies are lower than the initial numerical predictions.

Two finite element configurations were considered.

The first model did not include the accelerometers and was used to compare the 3D FEA results with the analytical Euler–Bernoulli beam model.

The second model included the accelerometer masses in order to evaluate the mass-loading effect introduced by the sensors. In this second configuration, the accelerometers were represented using CONM2 concentrated mass elements placed at the experimental sensor locations. Three CONM2 elements were included, each with a mass of approximately:

$$m_{acc} = 4.2 \text{ g}$$

corresponding to the mass of one tri-axial accelerometer.

Item	Value / description
Analytical model	Euler–Bernoulli cantilever beam
Numerical model	3D MSC Nastran finite element model
Nastran analysis type	SOL 103 normal modes
Beam length	0.436 m/ 436 mm
Beam width	0.030 m/ 30 mm
Beam thickness	0.003 m/ 3 mm
Cross-sectional area	9.0×10^{-5} m^2
Mass per unit length	0.7065 kg/m
Second moment of area	6.75×10^{-11} m^4
Young's modulus	210 GPa
Poisson's ratio	0.3
Density	7850 kg/m^3
Element type	CHEXA hexahedral solid elements
Number of grid points	3212
Number of solid elements	1450
Boundary condition	Left end fully clamped
Constrained DOFs	1–6 fixed at the clamped section
Accelerometer modelling	CONM2 lumped masses in the mass-loaded model
Accelerometer mass	approximately 4.2 g each

Table 6.4 : Analytical and MSC Nastran beam model properties

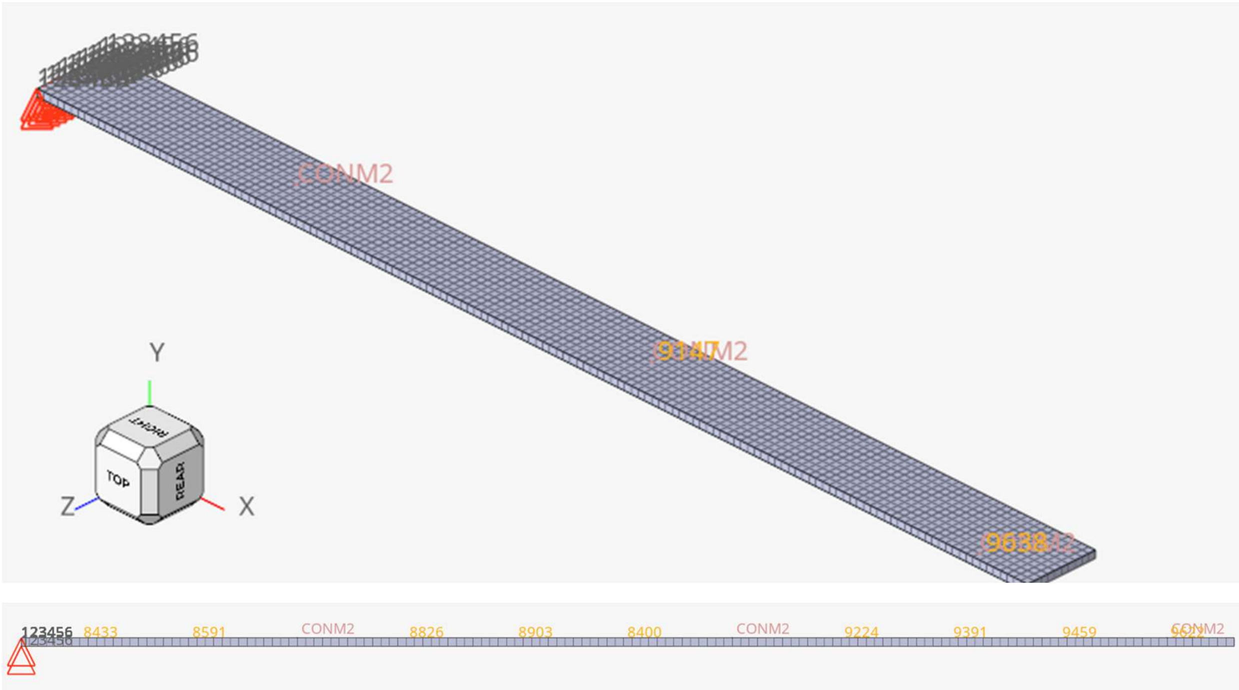

Figure 6.5 : MSC Nastran finite element model of the cantilever beam. The beam was discretized using CHEXA solid elements and fully constrained at the left end to reproduce the clamped-free boundary condition. In the mass-loaded configuration, the accelerometers were represented using CONM2 concentrated mass elements.

The comparison between the analytical Euler–Bernoulli model and the 3D Nastran model showed very small differences for the main bending modes. For the vertical bending modes, the analytical–FEA error remained approximately between 0.38%and 0.48%. This confirms that the finite element discretization was sufficiently accurate for the global bending modes and that the simplified Euler–Bernoulli model was justified as an analytical reference.

Therefore, the larger discrepancies observed between the numerical and experimental frequencies cannot be attributed mainly to poor mesh discretization or to the use of the 1D analytical beam theory. They are more likely related to experimental effects such as finite clamping stiffness, fixture compliance, accelerometer mass loading, and small deviations from the ideal clamped-free boundary condition.

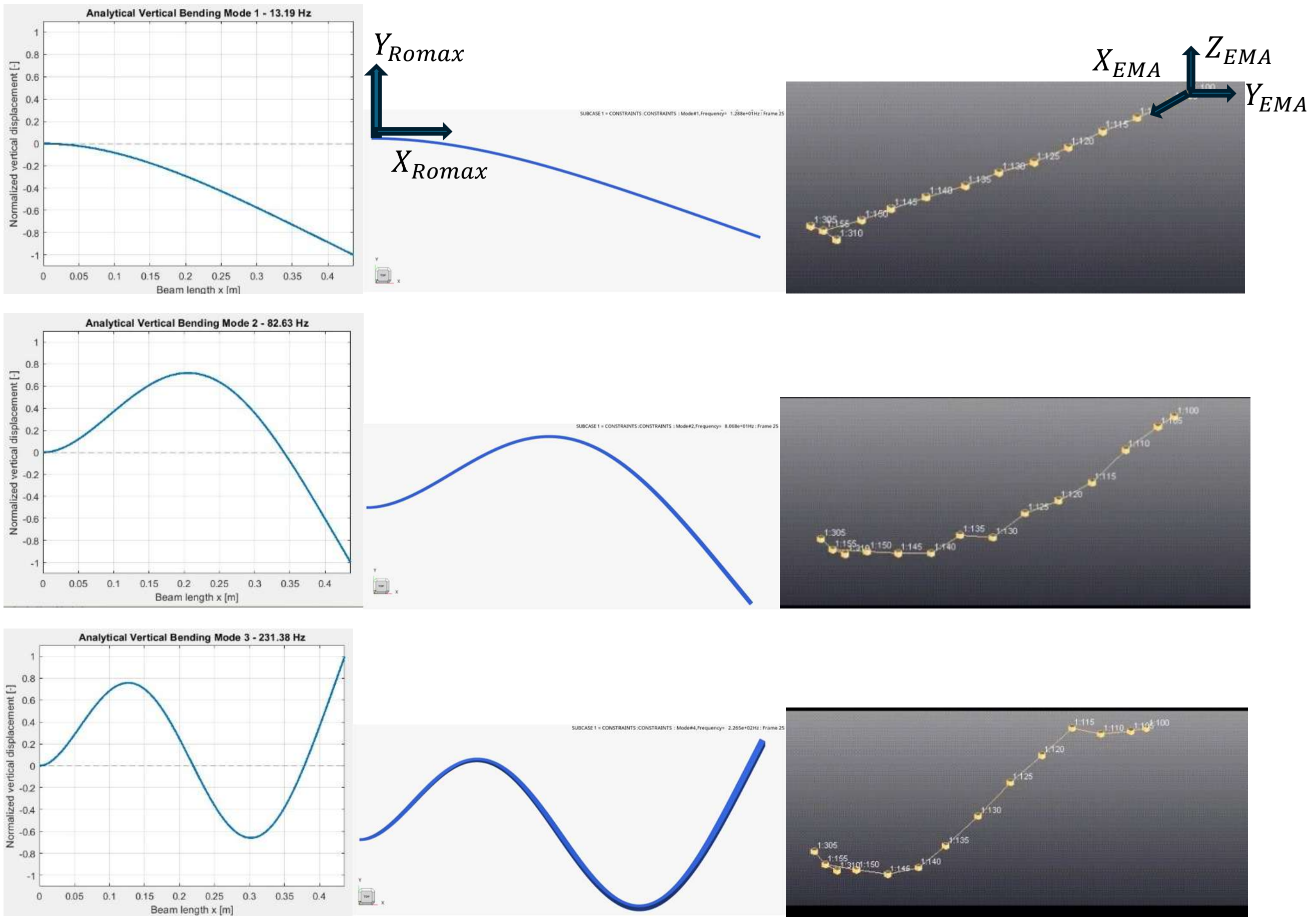

Figure 6.6: Visual comparison of the 3 primary bending mode shapes in Analytical , FEA and EMA from left to right in the EMA unlike the other two the fixed end is on the right, and the EMA shows the same mode shape but with eigenvector multiplied by -1.

The software initially identified 12 modes in the selected frequency range. The identified frequencies and damping ratios are summarized below.

Mode	Frequency [Hz]	Damping ratio [%]	Preliminary interpretation
1	11.687	0.34 %	1st vertical bending mode
2	74.233	0.65 %	2nd vertical bending mode
3	117.772	0.35 %	1st horizontal bending mode
4	207.590	0.5 %	3rd vertical bending mode
5	293.879	5.69 %	1st Torsional mode around beam axis
6	304.600	1.71 %	Vertical bending coupled with torsion around beam axis
7	412.752	0.48 %	4th vertical bending mode
8	687.879	0.55 %	5th vertical bending mode
9	706.834	0.92 %	2nd horizontal bending mode
10	860.305	5.25 %	2nd Torsional mode around beam axis
11	1054.802	0.96 %	6th vertical bending mode
12	1443.185	0.56 %	7th vertical bending mode

Table 6.5: EMA Modes frequency, damping ratio and interpretation

Although 12 modes were mathematically identified, a physical interpretation of the results was necessary. Modes 5 and 10 showed damping ratios greater than 5 percent, which is unusually high for a steel beam in this type of test.

6.7 MATLAB post-processing

After the modal extraction in Testlab, the experimental data were exported for independent post-processing in MATLAB. The measured FRFs were exported as MAT files, while the identified mode shapes were exported using universal file format. The objective of the MATLAB workflow was to provide an autonomous verification layer beyond the Testlab interface.

The MATLAB post-processing included the following tasks:

1. import of experimental FRFs and modal data;
2. organization of input and response coordinates;
3. coordinate-system alignment between experimental and numerical models;
4. FRF synthesis using the identified modal parameters;
5. comparison between experimental and synthesized FRFs;
6. Maxwell reciprocity checks;
7. Auto-MAC computation for experimental mode-shape independence;
8. Cross-MAC computation for FE/EMA mode-shape correlation;
9. frequency-error calculation;
10. Rayleigh damping identification.

6.8 Conclusions from the beam validation

The cantilever beam activity successfully validated the complete experimental and post-processing workflow required for the powertrain study. The acquisition chain was verified, the roving-hammer strategy was tested, modal parameters were identified using PolyMAX, and the MATLAB post-processing workflow was developed and checked. The beam was particularly useful because it is simple enough to interpret physically, but still sensitive to important experimental effects such as boundary-condition flexibility, accelerometer mass loading, measurement noise, and possible nonlinear behaviour.

The beam test also showed that the quality of the measured FRFs depends strongly on the selected input-output coordinates. In general, the results were more repeatable when the considered points were closer to the clamped root of the beam. In this region, the vibration amplitude is lower and the motion is more controlled by the boundary condition. Moving toward the free tip, the oscillation amplitude increases and the beam becomes more flexible. As a consequence, the measured response can become more sensitive to small nonlinear effects, imperfect impacts, local flexibility, sensor mass loading, and small variations in the boundary condition. Therefore, the comparison between reciprocal FRFs is expected to be better for points closer to the root and more critical for points closer to the free end.

For this reason, the reciprocity check should not be presented only with the best possible FRF pair. A representative pair of closer points should be shown to demonstrate the expected good agreement, while an additional less favourable or more flexible input-output pair should be included to show the real experimental limitations. The plot must clearly indicate the measured direction, for example (Z)-direction inertance, so that the compared FRFs are physically consistent.

The acquisition duration for the beam test was checked using the impulse-response concept introduced in Section 4.2. After the hammer impact, the beam response behaves as a free-decay signal governed by the exponential term $\left(e^{-\zeta \omega_n t}\right)$. The first bending mode is the most critical mode for the acquisition time because it has the lowest natural frequency and therefore the slowest decay. Higher modes decay more rapidly because the product $(\zeta \omega_n)$ is larger. Therefore, the acquisition window was selected to be long enough to capture the decay of the first mode without repeating the impulse-response plot in this chapter.

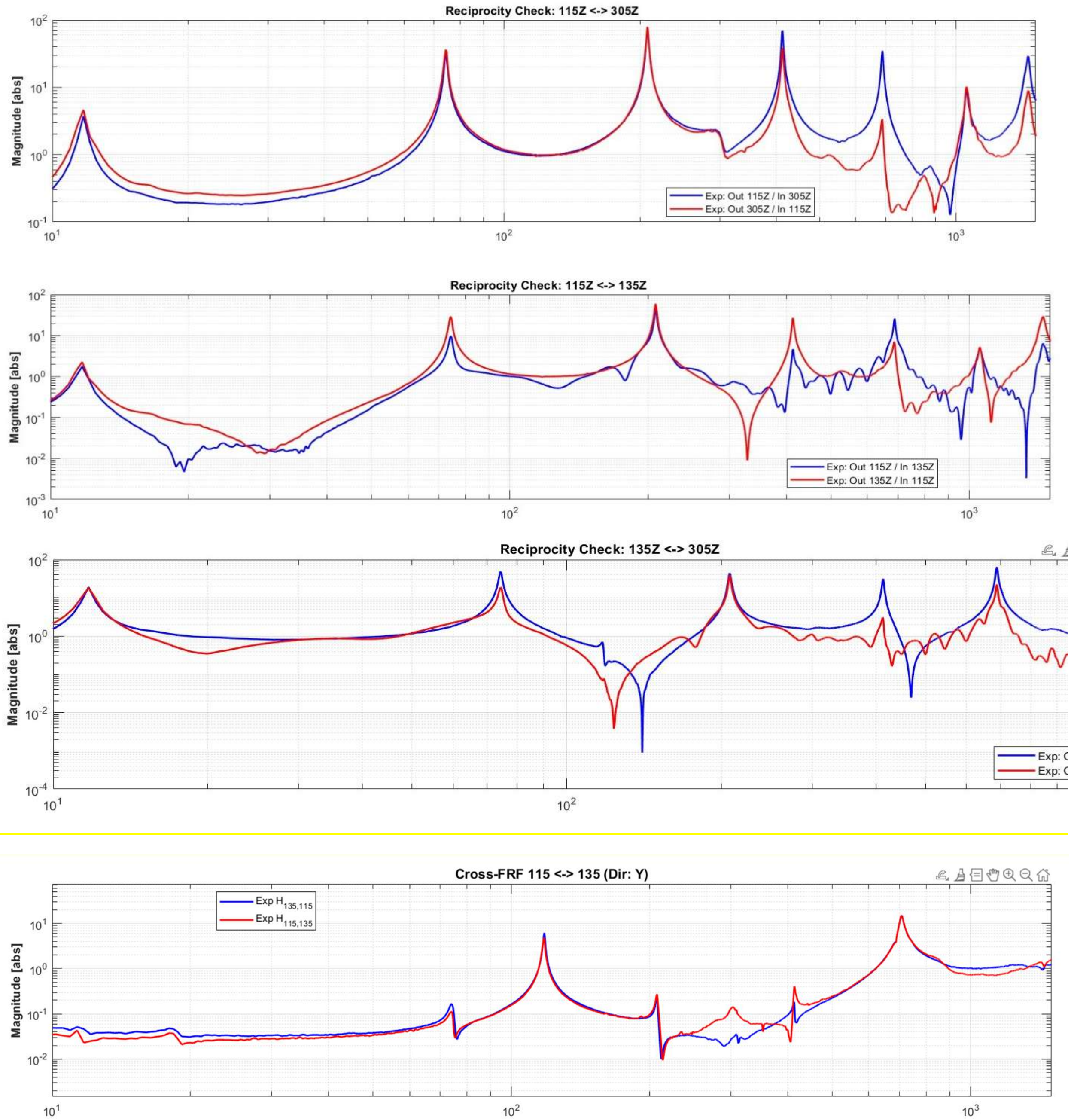

Figure 6.7: Maxwell's Reciprocity evaluation

The reciprocity comparison is based on Maxwell's reciprocity theorem. For a linear reciprocal structure, the cross-inertance measured from input coordinate k to response coordinate l should be equivalent to the cross-inertance measured from input coordinate l to response coordinate k, provided that the same physical direction is considered. In this thesis, reciprocity was used as an experimental consistency check rather than as a strict exact equality requirement, because small differences can appear due to manual hammer excitation, local flexibility, antiresonance regions, and measurement noise.

Figure 6.7 shows representative reciprocity comparisons for the beam test. The agreement is acceptable in the Z-direction and Y-direction, where the reciprocal FRFs show similar resonance peaks and comparable global trends. This confirms that the measured dataset is sufficiently consistent for the main bending-mode identification and for the following modal correlation steps. The remaining differences between reciprocal curves are considered acceptable because the beam response is sensitive to impact location, excitation direction, and local vibration amplitude, especially near the free end.

The reciprocity result in the X-direction is less reliable. This is mainly related to the practical limitation of the acquisition strategy: the X-direction excitation was performed only once and only at the limited accessible locations near the free end of the beam. Therefore, the X-direction reciprocal comparison has lower repeatability than the Y- and Z-direction cases and should be interpreted with more caution. For this reason, Figure 6.7 reports only representative reciprocity checks in the main text, while the additional reciprocity plots are reported in the appendix.

The Auto-MAC matrix was used to evaluate the geometrical similarity between the experimentally identified mode shapes. The diagonal terms are equal to one because each mode is compared with itself. The off-diagonal terms indicate whether different identified modes have similar spatial deformation patterns. Low off-diagonal values confirm that the mode shapes are well separated from a geometrical point of view, while high off-diagonal values may indicate similar deformation shapes, closely spaced modes, insufficient spatial resolution, or identification uncertainty.

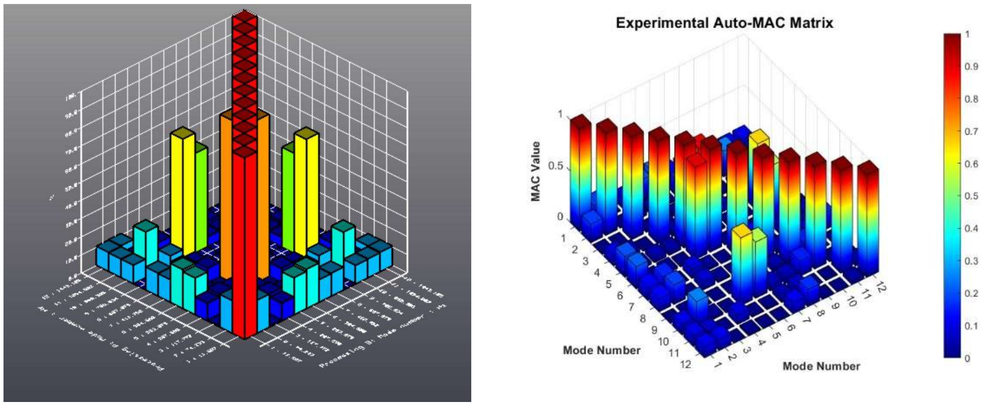

Figure 6.8: Auto-MAC 3D Matrix displaying experimental mode independence

.

The Cross-MAC matrix was then used to compare the experimental mode shapes with the numerical mode shapes. This comparison is necessary because frequency agreement alone is not sufficient for model validation. A mode can have a frequency close to a numerical prediction but still represent a different deformation pattern. The Cross-MAC results therefore provide a quantitative indication of the similarity between experimental and numerical mode shapes.

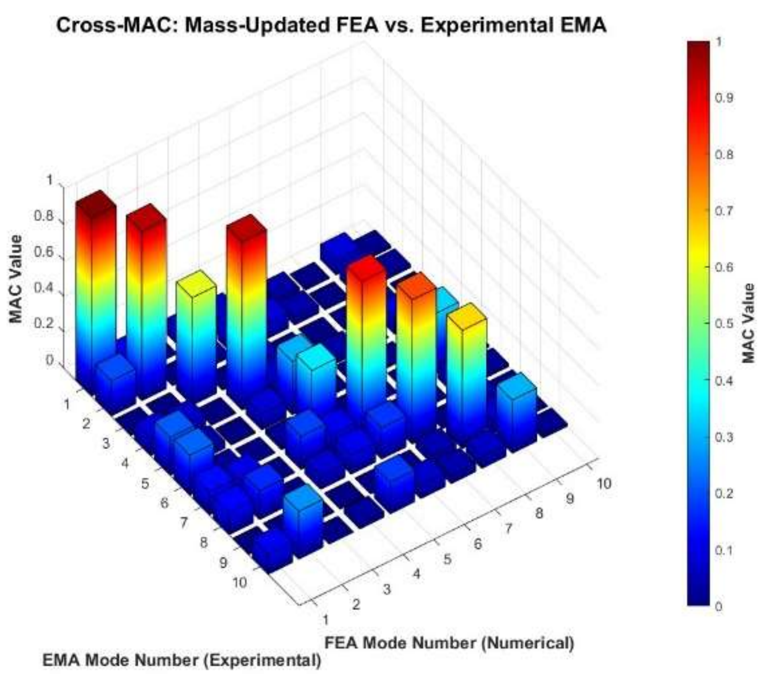

Figure 6.9: 3D Bar plot of the Cross-MAC matrix

CROSS-MAC CORRELATION RESULTS			
EMA Mode	**Freq [Hz]**	**Best Match FEA & EMA Mode**	**MAC Value**
1-1stVB	11.69	1	0.994
2-2ndVB	74.23	2	0.944
3-1stHB	117.77	3	0.600
4-3rdVB	207.59	4	0.938
5-1stT	293.88	5	0.298
6-V+T	304.60	5	0.357
7-4thVB	412.75	6	0.879
8-5thVB	687.88	7	0.803
9-2ndHB	706.83	8	0.659
10-2ndT	860.30	9	0.297

Table 6.6: Tabular breakdown of the best-matched EMA & FEA modes (V:vertical, H:Horzontal, B:Bending, and T:Torsional) and their corresponding MAC values AVERAGE MAC (For Matched Modes): 0.677

The initial FE/EMA comparison showed that the numerical model overestimated the natural frequencies when ideal material properties and ideal boundary conditions were assumed. This discrepancy was expected because the real experimental system included additional effects that were not fully represented in the initial numerical model. These effects included the finite stiffness of the clamped boundary, accelerometer mass loading, and small compliance of the fixture. After including the accelerometer mass and updating the effective Young's modulus, the agreement between the numerical and experimental frequencies improved significantly.

Mode Type	Mode No.	Analytical (1D)	FEA (3D Simulation)	EMA (Lab Test)	FEA vs. EMA Error	Analytical vs. FEA Error
Vertical Bending	1st	13.19 Hz	13.24 Hz	11.69 Hz	13.29 %	0.38 %
Vertical Bending	2nd	82.63 Hz	82.96 Hz	74.23 Hz	11.76 %	0.40 %
Horizontal Bending	1st	131.90 Hz	131.60 Hz	117.77 Hz	11.74 %	0.23 %
Vertical Bending	3rd	231.38 Hz	232.30 Hz	207.59 Hz	11.90 %	0.40 %
Torsional	1st	-	357.50 Hz	293.87 Hz	21.65 %	-
Vertical Bending	4th	453.40 Hz	455.20 Hz	412.75 Hz	10.28 %	0.40 %
Vertical Bending	5th	826.43 Hz	807.10 Hz	687.87 Hz	17.33 %	2.34 %
Horizontal Bending	2nd	749.51 Hz	752.60 Hz	706.83 Hz	6.47 %	0.41 %
Vertical Bending	6th	1119.64 Hz	1125.00 Hz	1054.80 Hz	6.66 %	0.48 %

Table 6.7: Error in Vertical, Horizontal and Torsional modes, with different methods.

The comparison between the analytical 1D Euler–Bernoulli beam model and the 3D FEA model shows very small discrepancies. For the vertical bending modes reported in Table 6.5, the analytical–FEA error remains approximately between $0.38\%$and 0.48%, with an average error of about 0.4%. This confirms that the simplified Euler–Bernoulli formulation is suitable for representing the main vertical bending behaviour of the beam.

The Cross-MAC analysis highlights that the highest correlation is obtained for the vertical bending modes, which show MAC values between 0.803 and 0.994. The horizontal bending modes exhibit an intermediate level of correlation, with MAC values of 0.600 and 0.659. Conversely, the torsional modes show poor correlation, with MAC values close to 0.30. However, these discrepancies should not be mainly attributed to modelling errors, since the torsional behaviour is evaluated from only two points located away from the beam centreline, making the estimation highly sensitive to experimental uncertainties, especially possible errors in the evaluation of the distance from the centreline.

Therefore, the use of a 1D analytical beam model is justified as a reference for the preliminary validation stage. Since the analytical and 3D FEA results are almost identical for the main bending modes, the larger differences observed between FEA and EMA cannot be attributed mainly to the analytical simplification. Instead, they are more likely related to experimental effects such as non-ideal clamping stiffness, accelerometer mass loading, fixture compliance, and small deviations from the ideal clamped-free boundary condition.

The extended comparison in Table 6.5 further confirms that the Euler–Bernoulli analytical model provides a good reference for bending-dominated modes. However, no analytical value is reported for the torsional mode, because the analytical model used in this work is based on Euler–Bernoulli beam theory, which describes bending deformation but does not predict torsional behaviour. For this reason, the Euler–Bernoulli model is considered reliable for validating the main bending-frequency trend, while the 3D FEA model remains necessary for interpreting torsional and coupled deformation modes.

MODEL UPDATING RESULTS			
Initial Young's Modulus: 210.00 GPa **UPDATED Young's Modulus: 174.62 GPa**			
Mode	**EMA (Target)**	**Initial Analytical**	**Updated Analytical**
1-1VB	11.69 Hz	13.19 Hz	12.02 Hz
2-2VB	74.23 Hz	82.63 Hz	75.35 Hz
3-3VB	207.59 Hz	231.38 Hz	210.99 Hz
4-4VB	412.75 Hz	453.40 Hz	413.45 Hz
Average Initial Error: 9.60 % **Average UPDATED Error: 2.11 %**			

Table 6.8: Final frequency results after updating the Effective Young's Modulus

The damping identified by Testlab was also analysed. Testlab estimates modal damping from the FRF behaviour in the neighbourhood of the resonance peaks. Therefore, the damping values are most reliable when the corresponding peak is clear, isolated, and well represented by the identified modal model. However, if a pole is computational, weakly excited, affected by noise, or close to another mode, the identified damping value may not be physically meaningful.

6.8.1 Experimental modal damping analysis

For the beam, the Rayleigh damping model was used as a compact way to describe the frequency dependence of damping. In Rayleigh damping, the damping matrix is written as

$$[C] = \alpha[M] + \beta[K]$$

and the damping ratio of mode (r) is

$$\zeta_r = \frac{\alpha}{2\omega_r} + \frac{\beta\omega_r}{2}$$

The first term, $(\alpha/(2\omega_r))$, is mass-proportional and decreases hyperbolically with frequency. The second term, $(\beta\omega_r/2)$, is stiffness-proportional and increases linearly with frequency. The Rayleigh coefficients (α) and (β) were estimated by using pinv (Pseudo-inverse) and fitting this expression to the experimental damping ratios of the accepted physical modes, making α=0.9323 and β=5.9069e-6.

Before fitting the Rayleigh damping curve, modes with unusually high damping values were examined carefully. In particular, modes 5 and 10 correspond to torsional modes of the beam and show damping ratios higher than 5%. Although flexural and torsional modes are not expected to have exactly identical damping values, their modal damping factors should generally remain of the same order of magnitude for a uniform steel beam unless a specific torsional dissipation mechanism is present. Therefore, the significantly higher damping values estimated for modes 5 and 10 are likely affected by the higher experimental uncertainty associated with the identification of the torsional modes. This interpretation is also supported by their low Cross-MAC values, which indicate weaker agreement between the experimental and numerical torsional mode shapes.

The damping-fit plot should report the mode number, frequency, damping ratio, and physical interpretation of the modes used in the fitting process. This information is important because the reader must understand which modes were retained, which modes were excluded, and why the fitted damping model is considered representative.

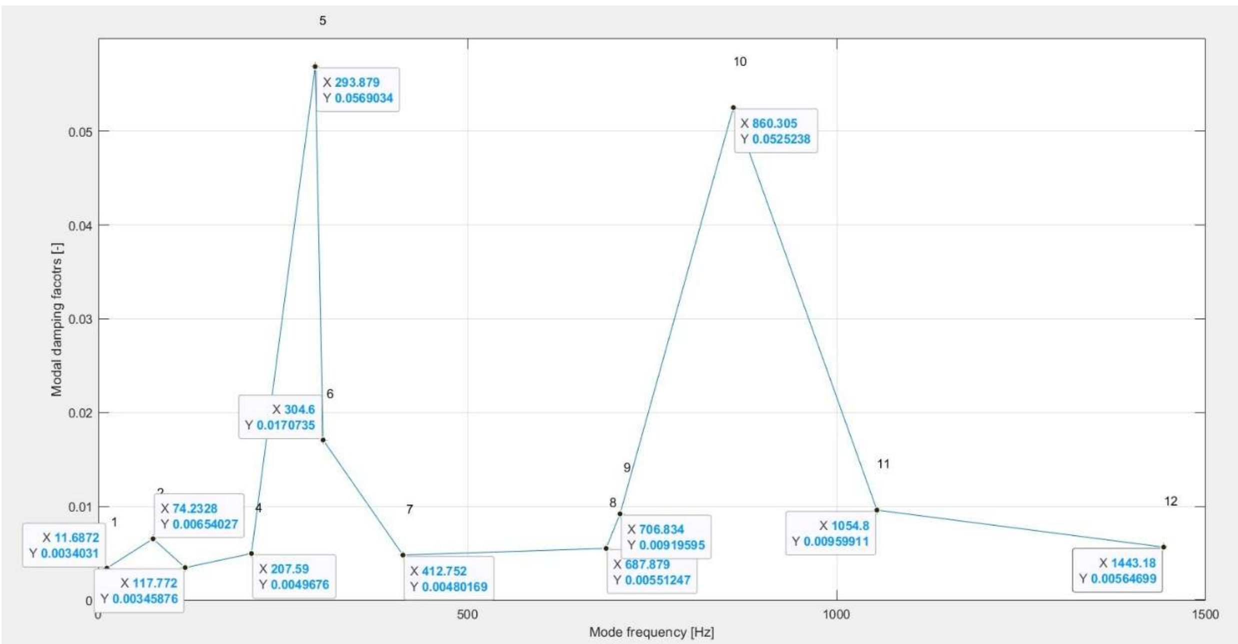

Figure 6.10: Rayleigh Damping with frequency and number of modes

Figure 6.10 reports the experimental damping ratio of each identified mode together with its modal interpretation. Modes 1, 2, 4, 7, 8, 11, and 12 are mainly vertical bending modes, modes 3 and 9 are horizontal bending modes, mode 6 is a coupled vertical bending/torsional mode, while modes 5 and 10 are torsional modes. The torsional modes show the highest damping values and are therefore treated with caution in the damping interpretation.

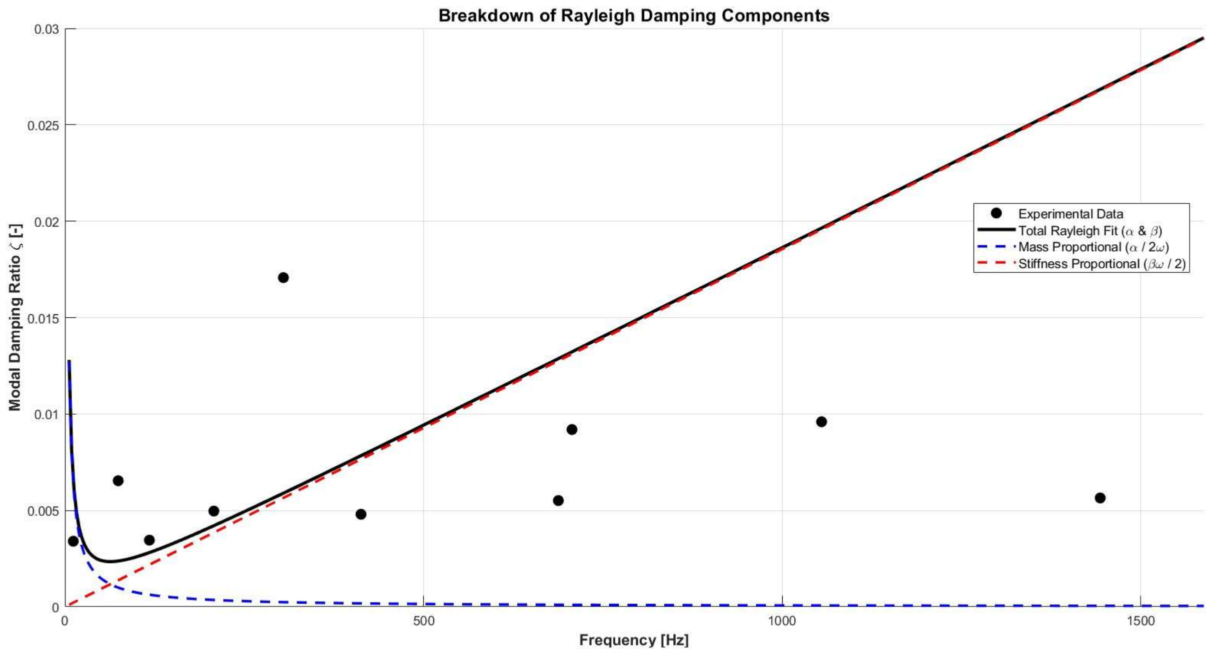

Figure 6.11: Rayleigh Damping identification curve considering only 1st and 2nd term of the proportional damping equation and the sum of the curves **α**=0.9323 & **β**=5.9069e-6 (The plot is zoomed so the mode 5 & 10 are not visible here)

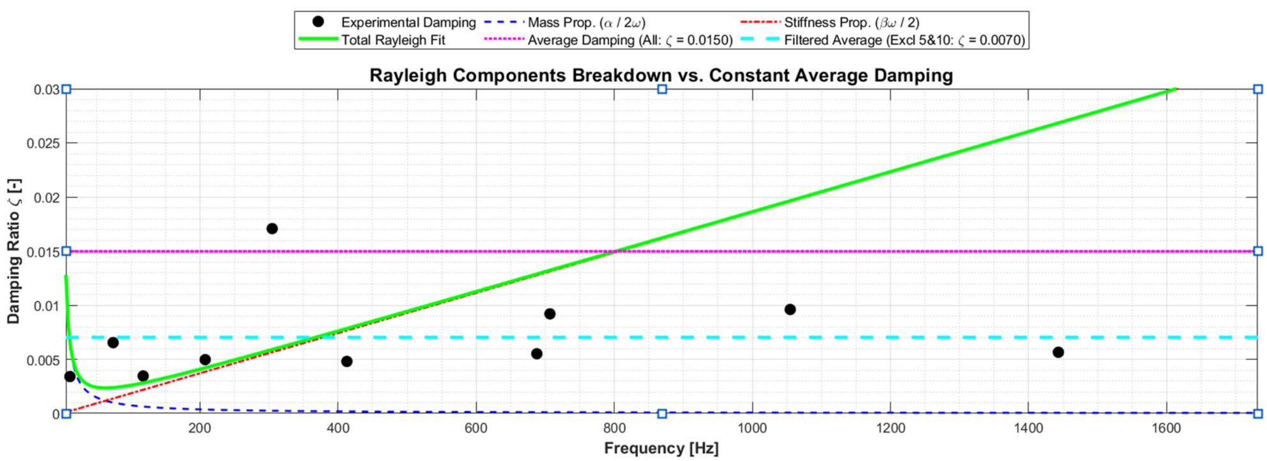

Figure 6.12: Comparison of experimental damping ratios with Rayleigh damping and constant average damping levels. The two horizontal lines define a practical constant damping range, showing that the beam damping is better represented by an approximately constant value than by the Rayleigh curve. (The plot is zoomed so the mode 5 & 10 are not visible here)

Figure 6.11 compares the experimental damping ratios with the Rayleigh proportional damping curve and with two constant average damping levels. The first horizontal line represents the average damping ratio calculated using all identified modes, while the second horizontal line represents the average damping ratio calculated after excluding modes 5 and 10, which showed unusually high damping values.

The purpose of these two horizontal lines is to show that the damping behaviour of the beam can be described more realistically by a nearly constant damping range rather than by a strongly frequency-dependent Rayleigh curve. Most of the physically accepted damping ratios are concentrated between these two constant levels. Therefore, a constant damping ratio in this range provides a better practical description of the experimental damping behaviour of the beam.

The Rayleigh model,

$$\zeta(\omega) = \frac{\alpha}{2\omega} + \frac{\beta\omega}{2}$$

shows a sharp variation at low frequency due to the mass-proportional term $\alpha/(2\omega)$, and then increases with frequency due to the stiffness-proportional term $\beta\omega/2$. This trend does not match the distribution of the experimental damping ratios very well. In contrast, the experimental points are mostly distributed around an almost horizontal level. For this reason, the damping of the beam is better interpreted as approximately constant within the range bounded by the two average damping lines.

Modes 5 and 10 were not used to define the lower average line because their damping ratios are much higher than the other modes and are not representative of the expected lightly damped behaviour of the steel beam. The lower horizontal line therefore represents the average damping of the more consistence dampings, while the upper horizontal line gives the average when all identified modes are included. The region between these two lines (0.7-1.5%) can be considered a reasonable constant damping range for the beam dataset.

The result of the beam study confirms that the experimental workflow is suitable for application to the electric powertrain. The beam validation demonstrated how to acquire reliable FRFs, identify modal parameters, verify reciprocity, evaluate mode-shape consistency with Auto-MAC, compare experimental and numerical mode shapes with

Cross-MAC, update physically meaningful model parameters, and build a damping model from selected experimental modes. These operations form the methodological basis for the powertrain analysis presented in the following chapters.

7 Electric Powertrain: Rigid-Body Identification

7.1 Purpose of the rigid-body identification stage

The first stage of the powertrain study is focused on the low-frequency dynamic behaviour of the complete assembly. In this range, the powertrain motion is expected to be strongly influenced by the rubber mounts and by the global mass and inertia properties of the assembly. The corresponding modes are often described as rigid-body or mount-controlled modes because the powertrain body moves mainly as a whole, while the deformation of the metallic components is limited.

Identifying these modes is important because they determine the vibration isolation performance of the mounting system. If the mount stiffness or damping is not correctly represented in the numerical model, the predicted rigid-body frequencies and mode shapes will differ from the experimental results. For this reason, the rigid-body identification stage provides direct information for mount-stiffness validation and possible updating.

7.2 Test bench and boundary conditions

The electric powertrain was tested on a Hardware-in-the-Loop test bench designed for controllable and repeatable validation of electric powertrains. The bench is intended for NVH performance assessment and for the experimental correlation of high-fidelity numerical models. In its complete operating configuration, the bench includes a Unit Under Test, a Load Emulating Unit, inverters, a bidirectional DC power supply, a rotating shaft, a torque meter, cooling components, safety barriers, and a control system.

In the present thesis, the bench was used primarily as a realistic mechanical support environment for impact-based Experimental Modal Analysis. The focus was not on powered operating conditions, but on the structural dynamic characterization of the mounted powertrain. This distinction is important because the modal test was performed to identify natural frequencies, damping ratios, and mode shapes, rather than to reproduce driving cycles or torque-speed operating points.

The most relevant aspect of the bench for this work is the mounting condition of the Unit Under Test. According to the bench documentation, the UUT is mounted using the same supports and elastic mounts as in the real vehicle [17] .

This condition is essential for the present EMA activity because the low-frequency modes of the assembly are strongly influenced by the rubber mounts and by the global mass and inertia properties of the powertrain. Therefore, the test bench provides a more representative boundary condition than a fully rigid laboratory fixture. The bench is built on a rigid steel frame isolated from the laboratory floor by rubber mats. A thick steel mounting plate with threaded holes allows the main components to be fixed in the required configuration.

From the point of view of modal correlation, this support condition must be considered carefully. Although the bench is designed to be stiff, it is not an ideal infinitely rigid ground. Its frame, mounting plate, bolted connections, and floor isolation may contribute to small discrepancies between the experimental modal properties and the numerical model, especially if the numerical model assumes ideal boundary conditions.

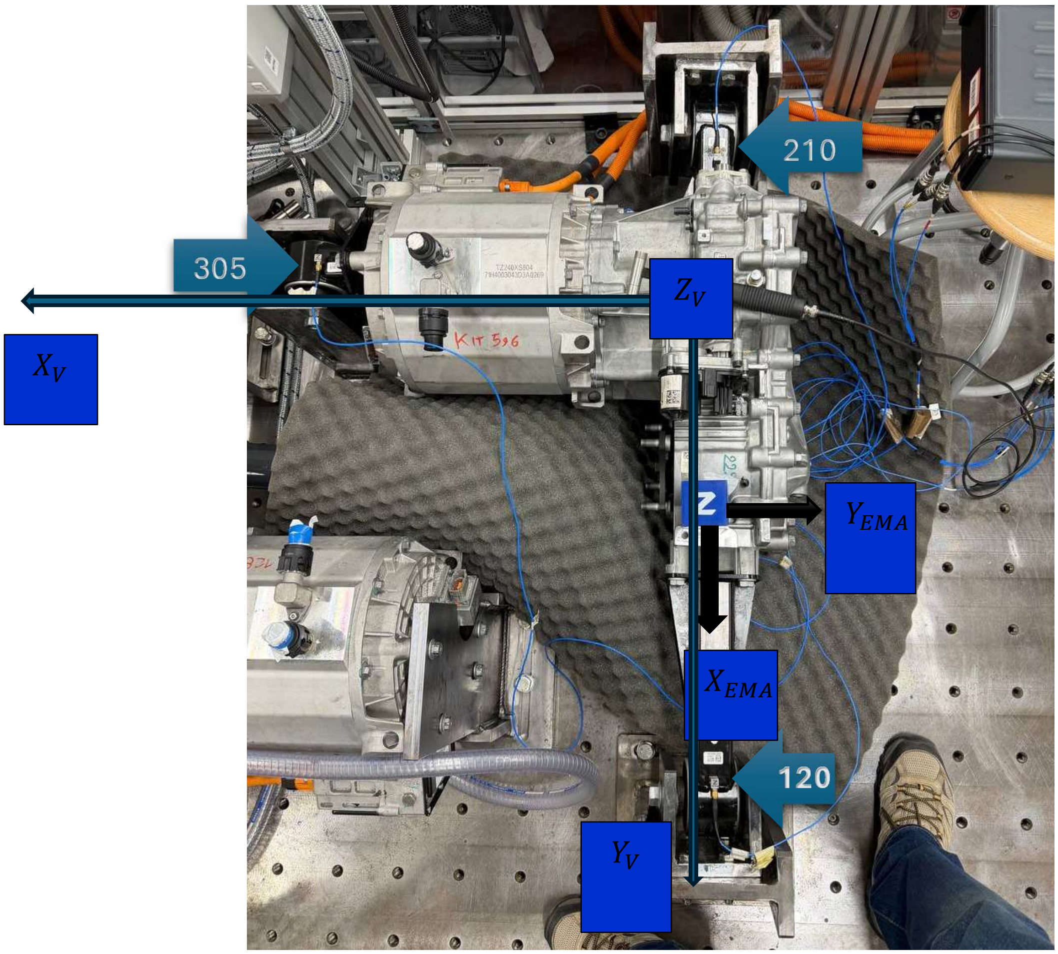

Figure 7.1 : Electric powertrain test bench and support system with Vehicle (subscript V) and Experimental (subscript EMA) reference frame

7.3 Powertrain mounting configuration

The electric powertrain was installed on the bench through its support system, including the long arm, short arm, rear arm, rubber mounts, brackets, and bolted connections. This configuration was selected because the purpose of the rigid-body identification stage was to characterize the global motion of the powertrain on its actual support paths. Testing the powertrain without its elastic mounts would not reproduce the boundary conditions relevant to the vehicle installation and would not allow the mount-controlled modes to be correctly identified.

In this thesis, the term rigid-body mode is used for low-frequency modes in which the powertrain assembly moves mainly as a whole on its rubber mounts, with limited deformation of the metallic components. When deformation of the mounting arms or brackets is visible, the safer term mount-controlled low-frequency mode is used. This distinction is important because purely rigid-body modes are mainly governed by the global mass, inertia, and mount stiffness, while mount-controlled modes may already include local flexibility of the support structure.

7.4 Rigid-body measurement nodes and reference DOFs

The experimental geometry was defined in Testlab by selecting measurement nodes on the mounting arms and on the powertrain body. The node set was chosen according to three criteria: physical relevance, accessibility, and suitability for mode-shape visualization. Nodes on the mounting arms were necessary because the arms represent the main structural paths between the powertrain body and the elastic mounts. Additional nodes on the powertrain body were included to describe the global motion of the assembly and to support comparison with the numerical model.

The initial measurement layout used one accelerometer on each main mounting arm. In the later configuration, the node set was expanded to improve the spatial description of the powertrain. The long arm was described with nodes on multiple faces so that bending and torsional deformation could be distinguished. Nodes on the short arm, rear arm, and powertrain body were included to capture the global motion of the assembly and to improve the reliability of EMA–Romax mode-shape comparison.

In Testlab, the experimental geometry was intentionally simplified. The purpose was not to reproduce the complete CAD topology of the powertrain, but to create a measurement geometry capable of visualizing the deformation at the selected experimental points. For this reason, nodes were connected using splines and the assembly was treated as a single experimental component. Screw nodes were also included where necessary because they represent the physical connection between the mounting arms and the motor body.

The following table summarizes the configuration used in the recent powertrain experimental activity. The measurement geometry used during the powertrain activity evolved during the experimental campaign. The layout reported later in the thesis was mainly used for the extended structural-mode analysis of the long arm and powertrain body. For the low-frequency rigid-body and mount-controlled correlation, additional nodes were also considered, including screw nodes and specific mounting-arm reference nodes.

The excitation directions were selected according to the accessibility and the physical orientation of each node group. The screw nodes were impacted only along the axial direction of the corresponding screw, because this direction represents the load path through the bolted connection. The nodes located on the horizontal face of the long arm were impacted in the vertical direction, while the nodes located on the vertical face were impacted horizontally. This strategy allowed the main local stiffness directions of the mounting arms to be excited while respecting the practical limitations of hammer access.

In particular, the MAC-based rigid-body comparison used the accelerometer-reference locations at nodes 120, 210, and 305. These nodes correspond to the long arm, short arm, and rear arm accelerometer positions. The numerical eigenvectors were extracted at the same physical locations and then transformed into the experimental reference system before computing the MAC.

Component	**Face / location**	**Node**	**x [m]**	**y [m]**	**z [m]**
Long arm	Screw	11	0.0000	0.0407	0.0430
Long arm	Screw	12	0.0000	0.0407	-0.0430
Long arm	Screw	13	0.0000	-0.0407	-0.0430
Long arm	Screw	14	0.0000	-0.0407	0.0430
Long arm	Horizontal face	105	0.1000	0.0040	0.0500
Long arm	Horizontal face	110	0.1500	0.0040	0.0500
Long arm	Horizontal face	115	0.2000	0.0040	0.0500

Long arm	Horizontal face	120	0.2500	0.0040	0.0500
Long arm	Vertical face	125	0.1000	0.0249	-0.0022
Long arm	Vertical face	130	0.1500	0.0249	-0.0022
Long arm	Vertical face	135	0.2000	0.0249	-0.0022
Long arm	Vertical face	140	0.2500	0.0249	-0.0022
Short arm	Screw	21	-0.5250	0.0407	0.0430
Short arm	Screw	22	-0.5250	0.0407	-0.0430
Short arm	Screw	23	-0.5250	-0.0407	-0.0430
Short arm	Screw	24	-0.5250	-0.0407	0.0430
Short arm	Horizontal face	205	-0.5400	0.0040	0.0500
Short arm	Horizontal face	210	-0.6000	0.0040	0.0500
Short arm	Vertical face	215	-0.5400	0.0249	-0.0022
Short arm	Vertical face	220	-0.6000	0.0249	-0.0022
Rear arm	Screw	31	-0.4134	-0.4886	0.1187
Rear arm	Screw	32	-0.3941	-0.4886	-0.1001
Rear arm	Screw	33	-0.4525	-0.4886	-0.0905
Rear arm	Screw	34	-0.5077	-0.4886	0.0548
Rear arm	Horizontal face	305	-0.4250	-0.5500	0.0670

Table 7.1 : Node coordination of the powertrain

7.5 Sensor placement and direction correction

Three tri-axial accelerometers were installed on the main support paths of the powertrain. One accelerometer was positioned on the long arm, one on the short arm, and one on the rear arm. This arrangement was selected as a compromise between spatial coverage and practical constraints such as available channels, cable routing, accessibility of the mounting surfaces, and the need to avoid interference with hammer impacts.

The accelerometer on the long arm was placed at node 120, the accelerometer on the short arm at node 210, and the accelerometer on the rear arm at node 305. This configuration allowed the response of the main mounting paths to be measured simultaneously and provided a first experimental description of the global mount-controlled motion of the powertrain.

Due to practical mounting constraints, the local axes of the accelerometers could not always be aligned with the global reference frame. In particular, some sensor axes were oriented opposite to the selected global directions. This was corrected in Testlab by assigning the corresponding negative measurement direction. This correction was necessary to avoid sign errors in the experimental mode shapes and to ensure consistency with the numerical coordinate system used for Romax or FE comparison.

Accelerometer	Location	Node	Main reason
Accelerometer 1	Long arm	120	response on main mounting arm
Accelerometer 2	Short arm	210	response on secondary support path
Accelerometer 3	Rear arm	305	response on rear support path

Table 7.2 : Accelerometer coordination

7.6 Hammer excitation strategy and tip selection

The powertrain was excited using the PCB 086C03 instrumented impact hammer. A roving-hammer strategy was adopted: the accelerometers remained fixed at selected reference locations, while the hammer was moved between the selected excitation nodes and directions. This strategy allowed several input coordinates to be tested while keeping the sensor mass distribution constant during the measurement campaign.

The hammer-tip selection was made according to the required frequency content of the input force. The powertrain test had to satisfy two requirements at the same time. First, the excitation had to contain enough low-frequency energy to identify rigid-body or mount-controlled modes. Second, the input had to preserve enough bandwidth to excite the first structural resonances of the mounting arms and powertrain body. For this reason, a medium-hardness plastic tip was selected.

The medium tip represents a compromise between the soft and hard tips. A softer tip would increase the contact duration and concentrate the input energy at lower frequencies, which is useful for rigid-body modes but may reduce the excitation of higher structural modes. A harder tip would extend the usable bandwidth but could reduce the low-frequency energy and make the impacts less repeatable on a complex mounted assembly. The PCB manual confirms that the frequency range of the hammer can be varied by changing the tip, and recommends stiffer tips for higher-frequency response and softer tips with extender mass for lower-frequency response.

As shown previously in Figure 5.2, the medium tip provides an intermediate force-spectrum bandwidth. The choice of the medium tip is also supported by the frequency response curves of the PCB 086C03 hammer family. These curves show that the medium tip occupies an intermediate position between the soft tips and the hard tip in terms of frequency bandwidth. Therefore, it was selected to excite both the low-frequency mount-controlled modes and the first higher-frequency structural modes without requiring multiple reconfigurations of the test setup.

7.7 Acquisition parameters and quality control

The acquisition settings were selected to provide sufficient frequency resolution for low-frequency modal identification. The bandwidth was set to 640 Hz, which was adequate for the rigid-body and mount-controlled frequency range of the powertrain. The number of spectral lines was set to 4096, resulting in a frequency resolution of 0.15625 Hz. This fine resolution was important because low-frequency modes can be close to each other, and damping estimation requires a sufficiently detailed description of the resonance peaks.

The acquisition time was set to 6.4 s. This value was chosen to allow the structural response to decay after the hammer impact. If the acquisition time is too short, the response is truncated and leakage errors appear in the frequency domain. If the acquisition time is excessively long, the useful vibration response may already have decayed and the measurement can become more affected by background noise. The selected acquisition time therefore represents a compromise between response decay and noise limitation.

Since the hammer impact is applied manually, it is not possible to reproduce exactly the same force amplitude for every strike. For this reason, the input range was configured in Testlab to define an acceptable force interval rather than a single target value. Impacts outside this range were rejected because they could either overload the measurement chain or provide insufficient excitation energy. This procedure improved repeatability while preserving the practical flexibility of manual impact testing.

Each measurement point was impacted three times and the corresponding FRFs were averaged. Averaging was used to reduce random variability caused by the manual impact process and to improve the signal-to-noise ratio. During acquisition, the force signal, acceleration responses, PSDs, instantaneous FRFs, averaged FRFs, and coherence functions were monitored. Measurements affected by overload, double impact, poor input level, abnormal PSD ripple, or poor coherence were rejected and repeated.

Parameter	Value	Reason
Bandwidth	640 Hz	covers low-frequency mount-controlled range
Spectral lines	4096	provides fine frequency discretization
Frequency resolution	0.15625 Hz	helps distinguish close resonances
Acquisition time	6.4 s	allows response decay after impact
Number of impacts per point	3	improves repeatability through averaging

Table 7.3 : Low-frequency powertrain acquisition settings

7.8 Low-frequency EMA mode identification

After acquisition, the accepted impacts were averaged to generate the low-frequency FRF dataset. The FRF sum was used as a first global indicator of the resonance distribution. This allowed the main frequency regions of interest to be identified before the detailed modal extraction. Individual FRFs were then inspected to check the consistency of the peaks, phase behaviour, and coherence.

The PolyMAX estimator was applied to the low-frequency FRF dataset. Stable poles were selected from the stabilization diagram by considering frequency stability, damping stability, correspondence with FRF resonance peaks, and physical plausibility of the associated mode shapes. A pole was not accepted only because it appeared in the stabilization diagram; it also had to correspond to a meaningful deformation pattern of the powertrain assembly.

The experimental analysis identified six relevant low-frequency modes. These modes were classified according to their dominant motion. The first three modes were mainly associated with global translations of the powertrain assembly along the principal directions, while the following modes showed bending and torsional characteristics. The six identified modes were therefore interpreted as rigid-body or mount-controlled modes, depending on the amount of visible deformation in the mounting arms and powertrain body.

The identified modes were classified as rigid-body modes or mount-controlled low-frequency modes. Modes were considered rigid-body-like when the powertrain moved mainly as a whole on the rubber mounts. When visible deformation of the mounting arms or brackets was present, the mode was classified as mount-controlled rather than purely rigid-body. This classification was necessary because the two types of modes are affected by different modelling parameters.

EMA mode	Experimental frequency [Hz]	Experimental damping ratio [%]	Dominant motion
1	22.79	1.80	Translation in Y
2	26.17	1.78	Translation in X
3	33.17	1.46	Translation in Z
4	43.40	2.05	Rotation around Z
5	48.48	3.08	Rotation around X
6	81.45	2.60	Rotation around Y

Table 7.4 : Experimental low-frequency modes identified by EMA

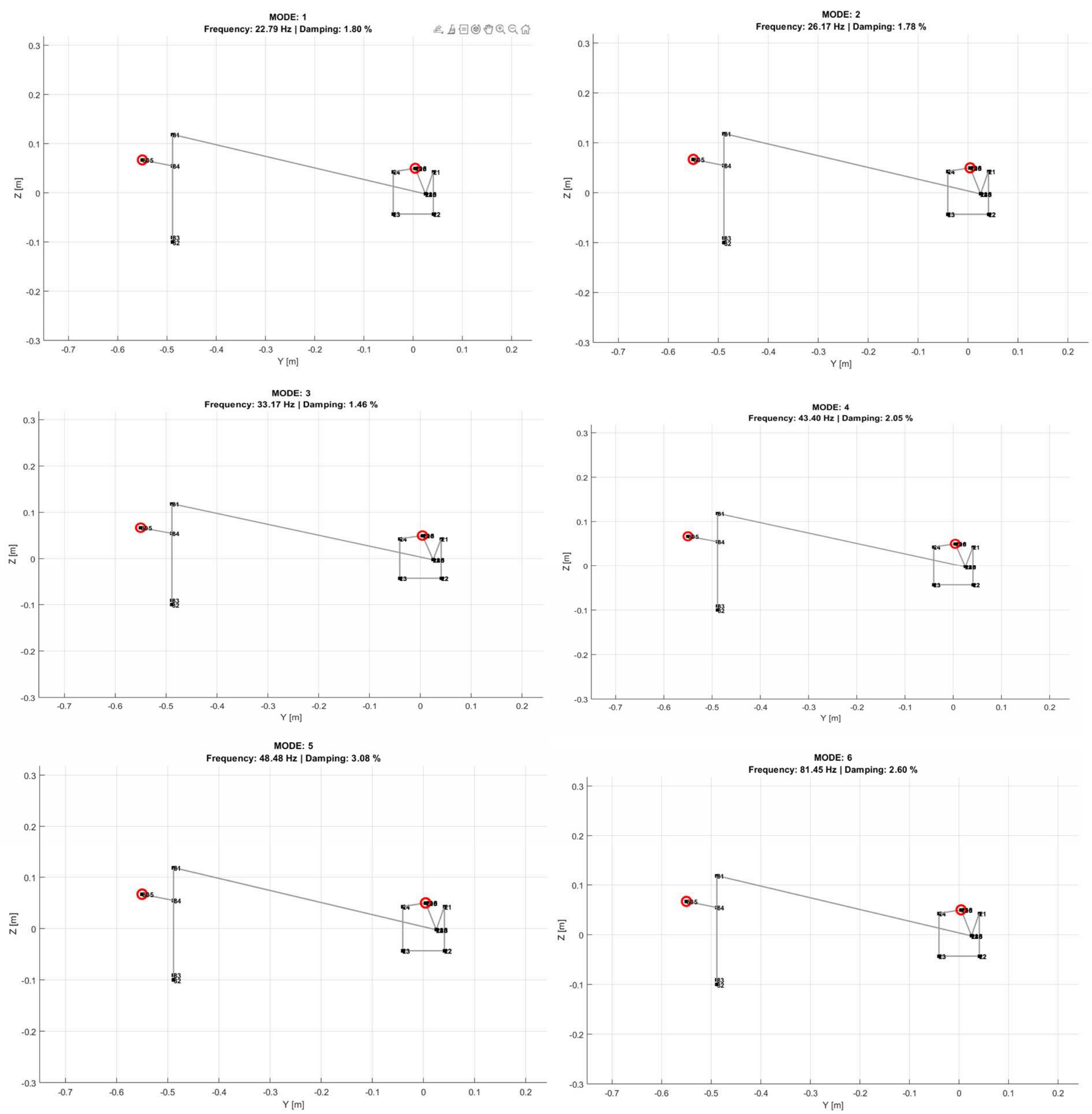

Figure 7.2 : EMA modes 1 to 6 with frequency and damping ratio

The damping ratios of the six low-frequency modes were also examined using a Rayleigh damping representation. This was done to observe the damping trend in the mount-controlled frequency range and to provide a compact damping model for the identified modes. However, in the rigid-body correlation stage, damping was not used as the primary validation parameter. The main correlation criteria were natural frequency, mode-shape interpretation, and MAC values.

*7.8.1 E*xperimental modal damping analysis

The Rayleigh fit should therefore be interpreted as a descriptive damping model for the experimental low-frequency modes, rather than as the main updating target for the Romax model. This is because the low-frequency damping is strongly affected by the rubber mounts, support conditions, and experimental boundary conditions.

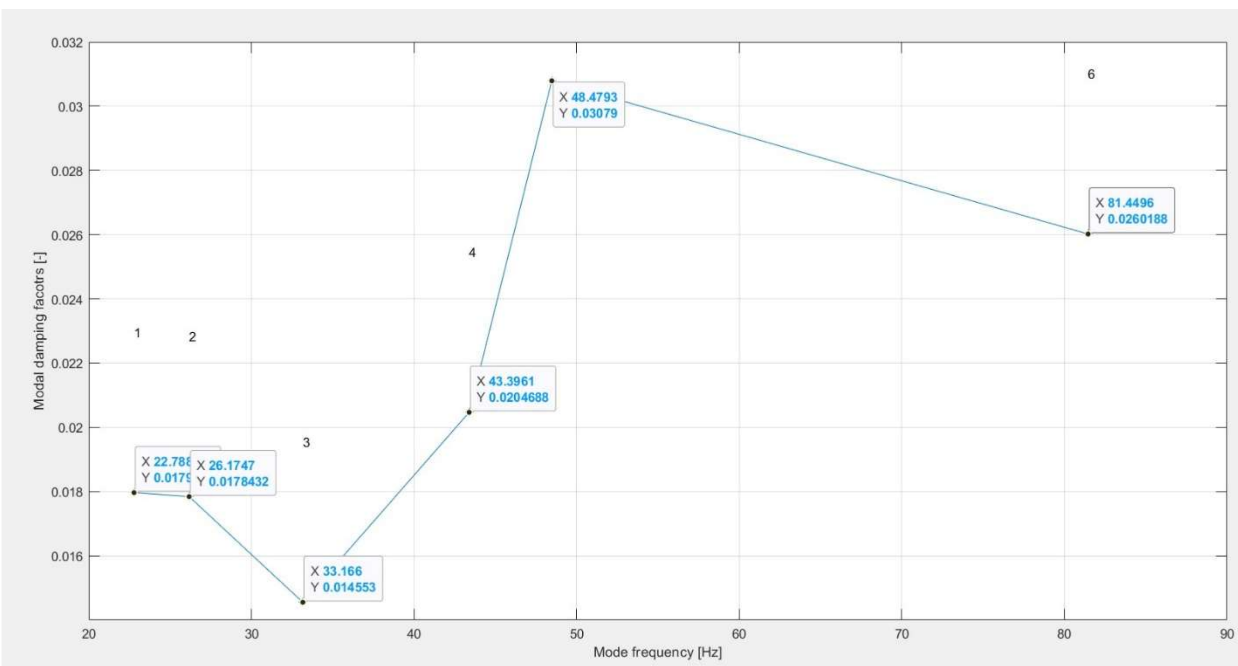

Figure 7.3: Rayleigh Damping with frequency and number of modes for low frequency range

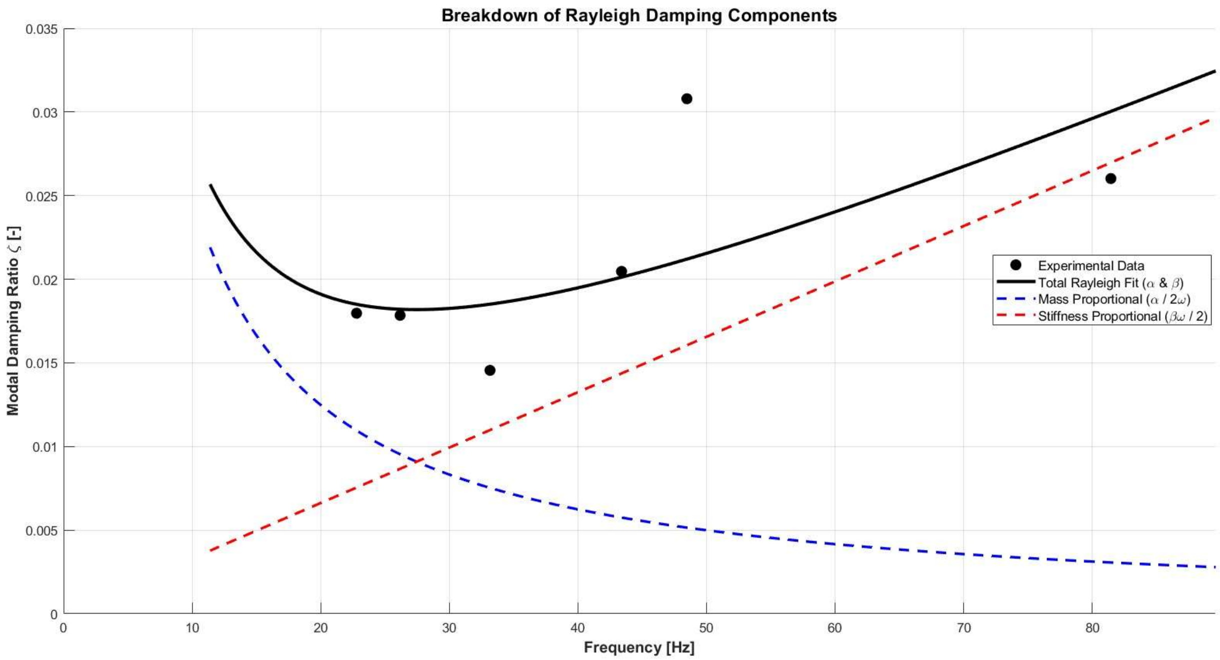

Figure 7.4: Rayleigh Damping identification curve considering only 1st and 2nd term of the proportional damping equation and the sum of the curves **α**=3.1371 & **β**=1.054e-6

The damping ratios identified for the low-frequency powertrain modes are higher than those obtained for the cantilever beam. In the beam case, the accepted physical modes were generally lightly damped, with most damping ratios below approximately 1%. This behaviour is expected for a steel beam with a relatively simple structure and limited internal dissipation. In contrast, the low-frequency powertrain modes show damping ratios in the range of approximately (1.5%) to (3.1%), as shown in Figure 7.3.

This higher damping level is physically reasonable because the low-frequency powertrain modes are governed mainly by the rubber mounts and by the support system. Unlike the beam, the mounted powertrain includes rubber elements, bolted interfaces, mounting arms, contact regions, and bench/support compliance. These elements introduce additional energy dissipation. Therefore, the damping of the mounted powertrain is not only material damping of the metallic structure, but also includes dissipation associated with the rubber mounts and the assembled boundary conditions.

The Rayleigh damping fit shown in Figure 7.4 provides a compact proportional damping representation of the identified experimental damping trend. In this model, the damping matrix can be written as

$$[C] = \alpha[M] + \beta[K]$$

where (\alpha) is the mass-proportional damping coefficient and (\beta) is the stiffness-proportional damping coefficient. For the low-frequency powertrain modes, the identified coefficients were $\alpha = 3.1371$, $\beta = 1.054 \times 10^{-6}$

The corresponding modal damping ratio is:

$$\zeta_r = \frac{\alpha}{2\omega_r} + \frac{\beta\omega_r}{2}$$

This representation is useful because, once the proportional damping coefficients are known, an equivalent damping matrix ([C]) can be introduced in a numerical model if the mass and stiffness matrices ([M]) and ([K]) are available. In this way, the damping behaviour identified experimentally can be used for dynamic response calculations.

However, in the present EMA–Romax correlation, damping was not used as the main updating parameter. The low-frequency validation focused primarily on natural frequencies, mode shapes, and MAC values, because these quantities are directly related to the mass, inertia, mount stiffness, and support stiffness of the powertrain. The Rayleigh damping model was therefore used mainly to describe the experimental damping trend and to show that the mounted powertrain has higher damping than the beam due to the presence of rubber mounts and assembled support interfaces.

7.9 Experimental and synthesized FRF comparison

After the low-frequency modes were identified, the quality of the modal extraction was verified by comparing the experimental FRFs with the synthesized FRFs generated directly in Simcenter Testlab. The experimental FRFs were obtained from the measured hammer force and acceleration responses, while the synthesized FRFs were reconstructed by Testlab from the modal parameters identified during the PolyMAX analysis.

This comparison was used as the first validation step of the EMA model. If the identified natural frequencies, damping ratios, and mode shapes are reliable, the synthesized FRFs should reproduce the main features of the measured experimental FRFs. In the present powertrain rigid-body analysis, the agreement between the experimental and synthesized FRFs was very satisfactory. The resonance peaks, antiresonance regions, and global FRF trends were reproduced with good accuracy, indicating that the selected modal parameters captured the dominant low-frequency dynamics of the mounted powertrain.

The synthesized FRFs are smoother than the experimental FRFs because they are generated from the identified modal model and are therefore less affected by measurement noise, impact variability, and small experimental disturbances. This difference is expected. The important result is that the synthesized curves follow the measured FRFs in the frequency regions where the rigid-body and mount-controlled modes were identified.

A second validation step was then performed in MATLAB. In this case, the identified FRFs were calculated independently using the exported modal parameters. This MATLAB reconstruction was introduced to verify the consistency of the post-processing workflow outside the Testlab environment and to prepare the data for further correlation operations such as MAC analysis and EMA–Romax comparison.

The MATLAB-identified inertance FRFs were calculated using modal superposition:

$$H_{ij}^{inertance}(\omega) = -\omega^2 \sum_{r=1}^{N} \frac{\phi_{ir}\phi_{jr}}{\omega_r^2 - \omega^2 + j2\zeta r\omega_r\omega}$$

where N is the number of selected modes, $\omega_r$is the natural angular frequency of mode r, $\zeta_r$is the damping ratio, and $\phi_{ir}$and $\phi_{jr}$are the modal components at the response and excitation coordinates.

The good agreement between the experimental FRFs, the Testlab synthesized FRFs, and the MATLAB-identified FRFs confirmed that the identified modal parameters were reliable. Therefore, the six low-frequency EMA modes were considered suitable for the following EMA–Romax correlation step.

FRF type	Source	How it was obtained	Purpose
Experimental FRFs	Testlab	measured from hammer force and accelerometer responses	direct experimental reference
Synthesized FRFs	Testlab	reconstructed by Testlab from PolyMAX-identified modal parameters	check quality of modal extraction inside Testlab
Identified FRFs	MATLAB	calculated later using exported modal parameters and modal superposition	independent verification and preparation for further correlation

Table 7.5 : FRF validation workflow for the rigid-body EMA analysis

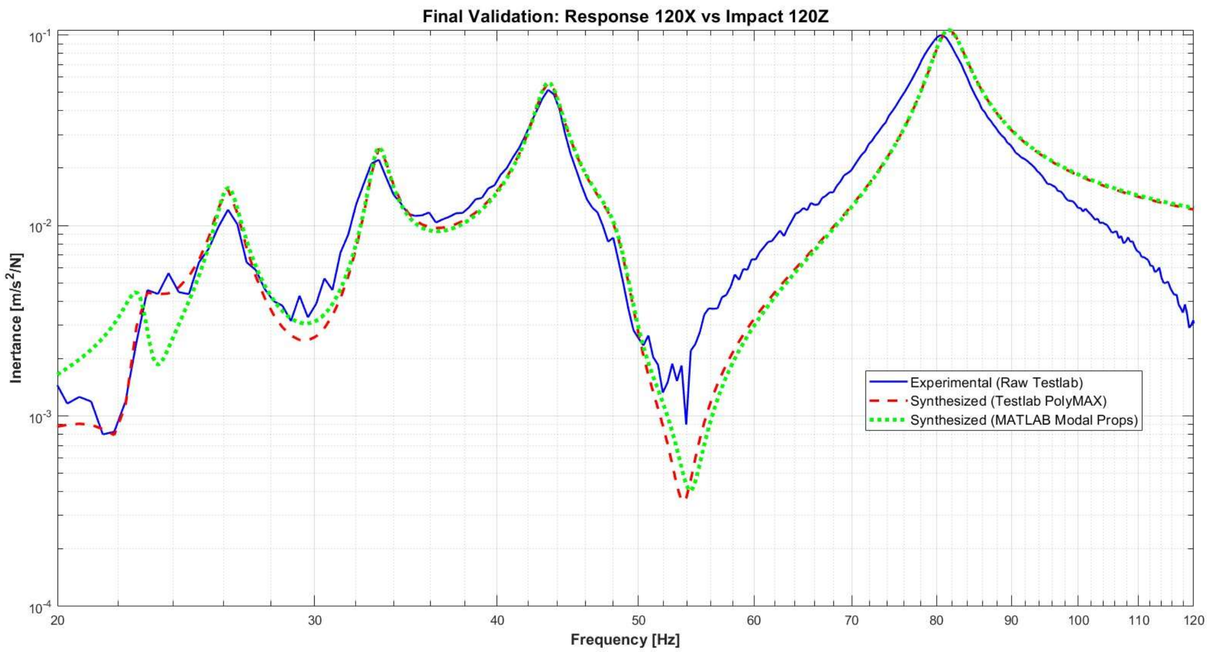
Final Validation: Response 120X vs Impact 120Z
Inertance [m/s^2/N]
Frequency [Hz]
Experimental (Raw Testlab)
Synthesized (Testlab PolyMAX)
Synthesized (MATLAB Modal Props)

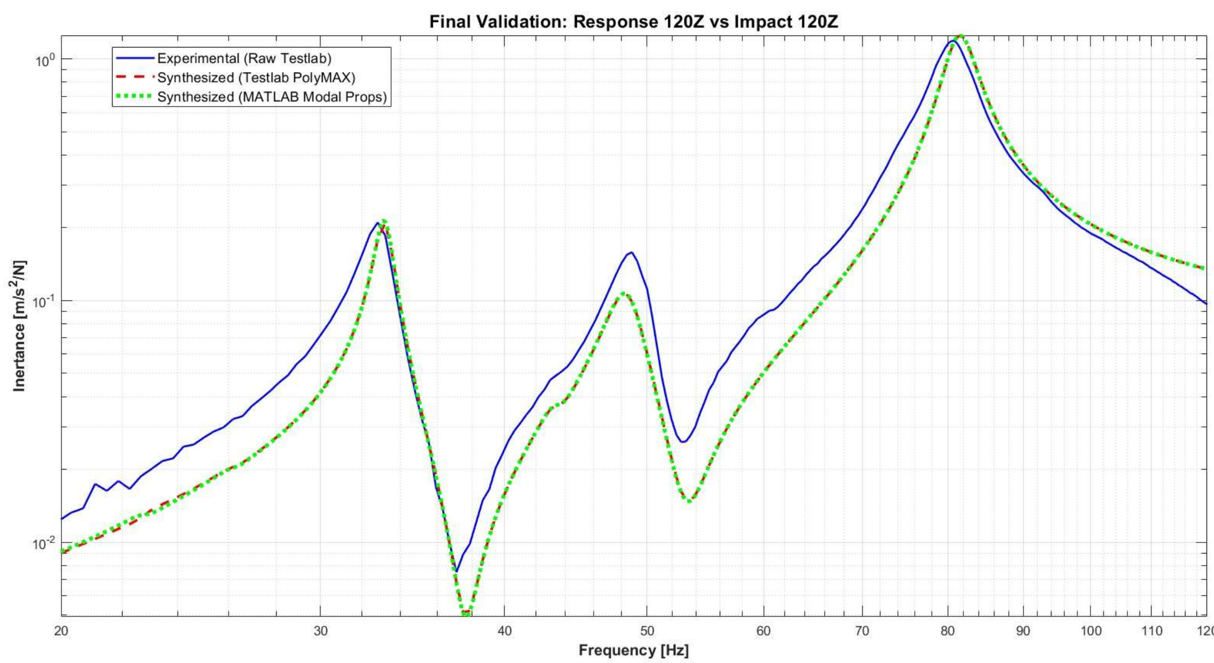
Final Validation: Response 120Z vs Impact 120Z
Inertance [m/s^2/N]
Frequency [Hz]
Experimental (Raw Testlab)
Synthesized (Testlab PolyMAX)
Synthesized (MATLAB Modal Props)

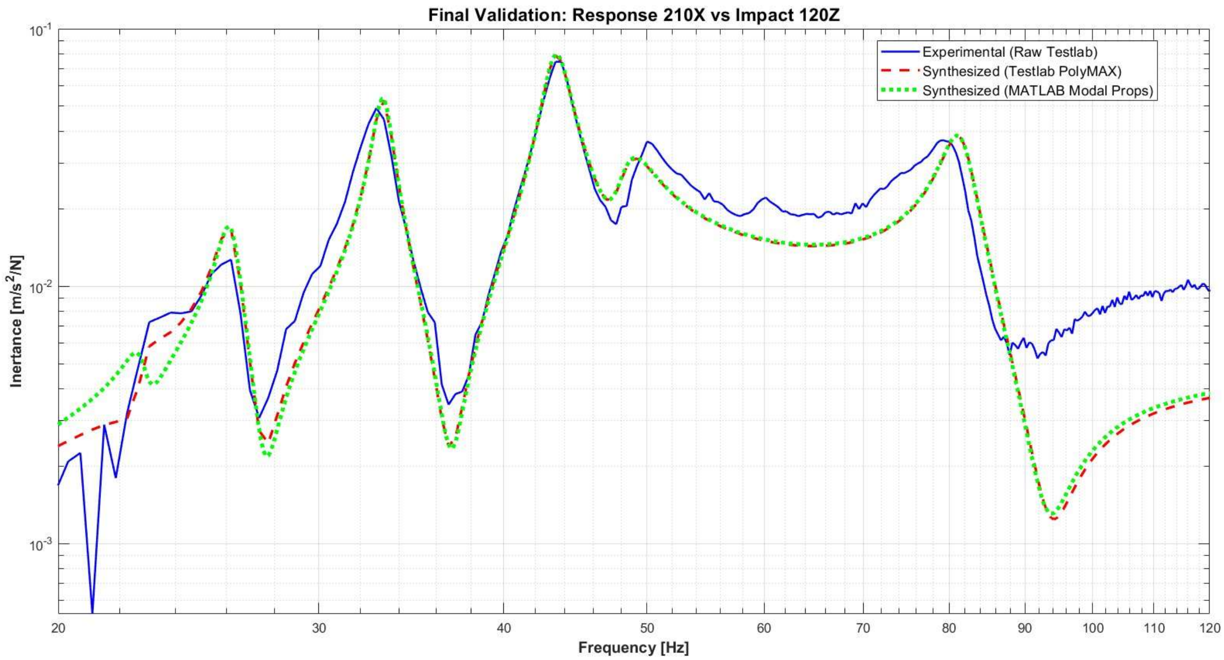
Final Validation: Response 210X vs Impact 120Z
Experimental (Raw Testlab)
Synthesized (Testlab PolyMAX)
Synthesized (MATLAB Modal Props)
Inertance [m/s²/N]
Frequency [Hz]

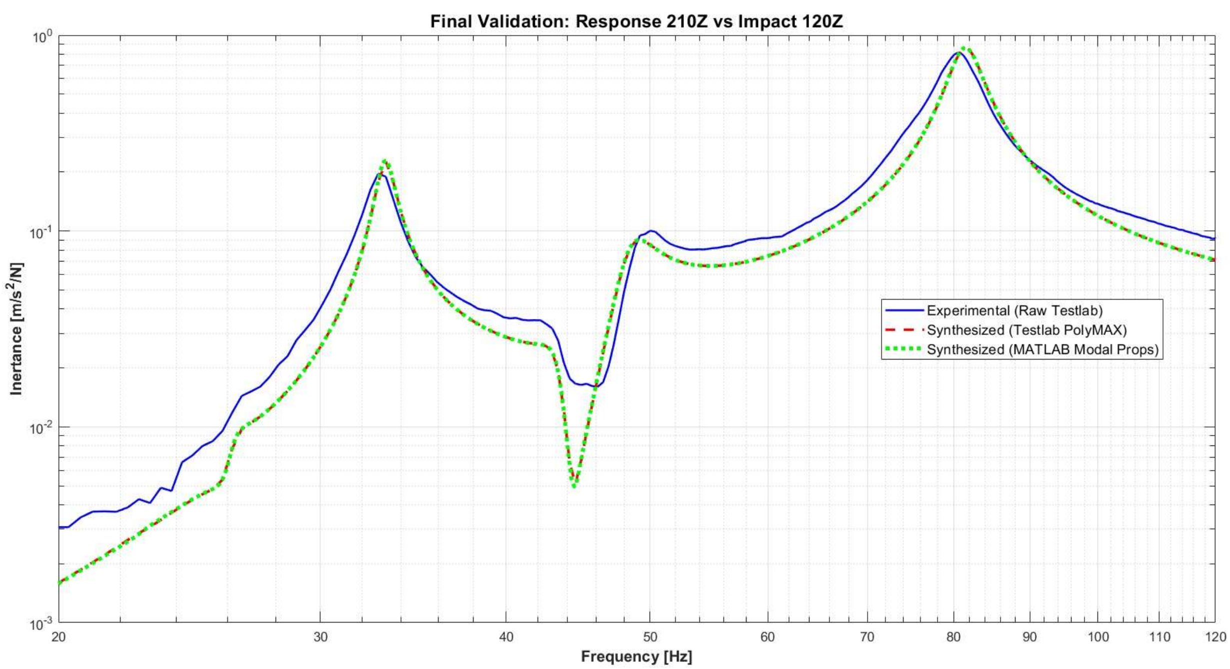
Final Validation: Response 210Z vs Impact 120Z
Experimental (Raw Testlab)
Synthesized (Testlab PolyMAX)
Synthesized (MATLAB Modal Props)
Inertance [m/s²/N]
Frequency [Hz]

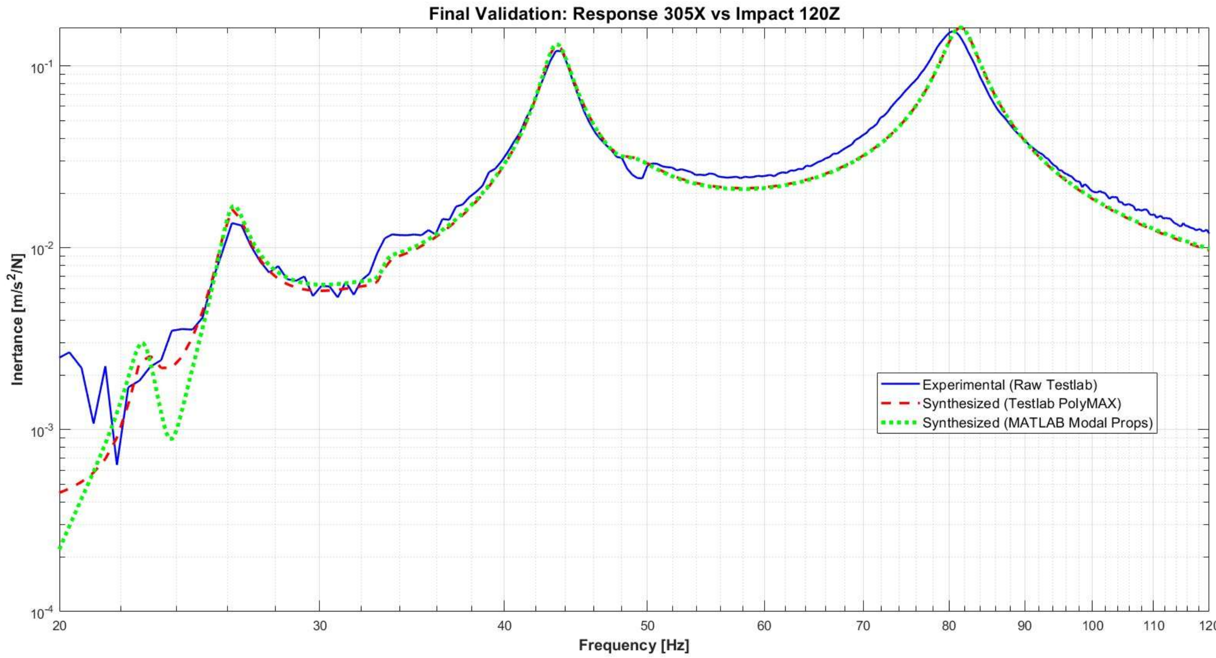

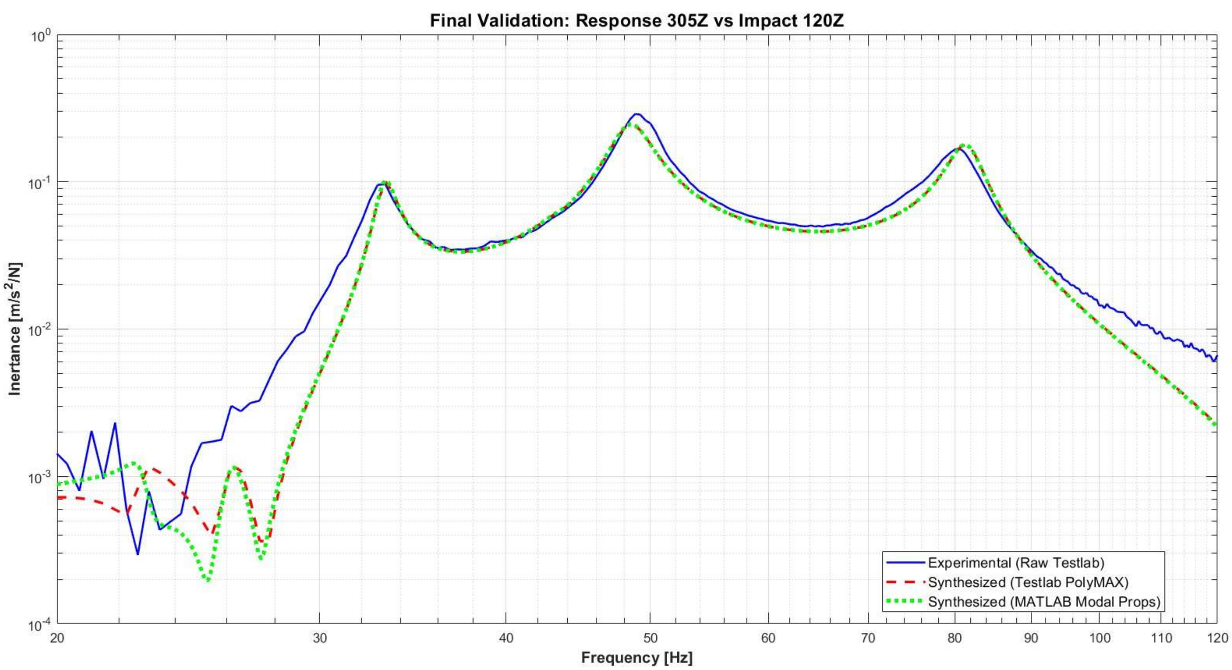

Figure 7.5 : Experimental, Testlab-synthesized and Matlab synthesised FRF comparison

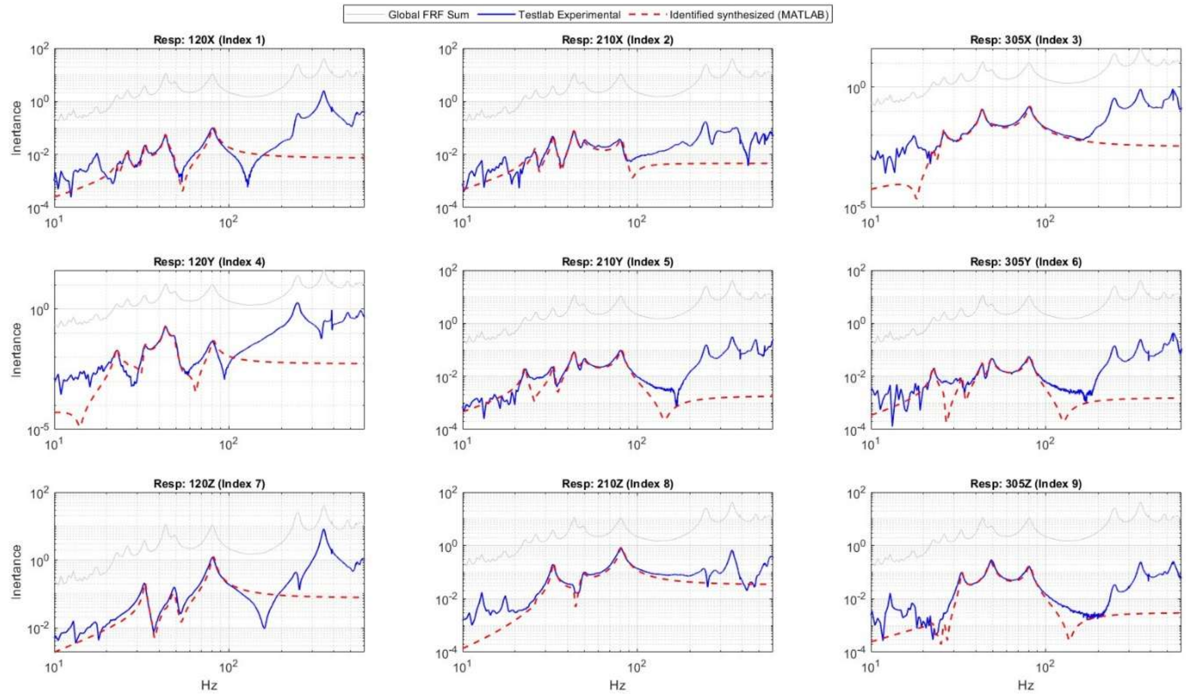

Figure 7.6 :Identified Synthesized MATLAB VS Experimental Testlab FRF comparison the impact is 120Z

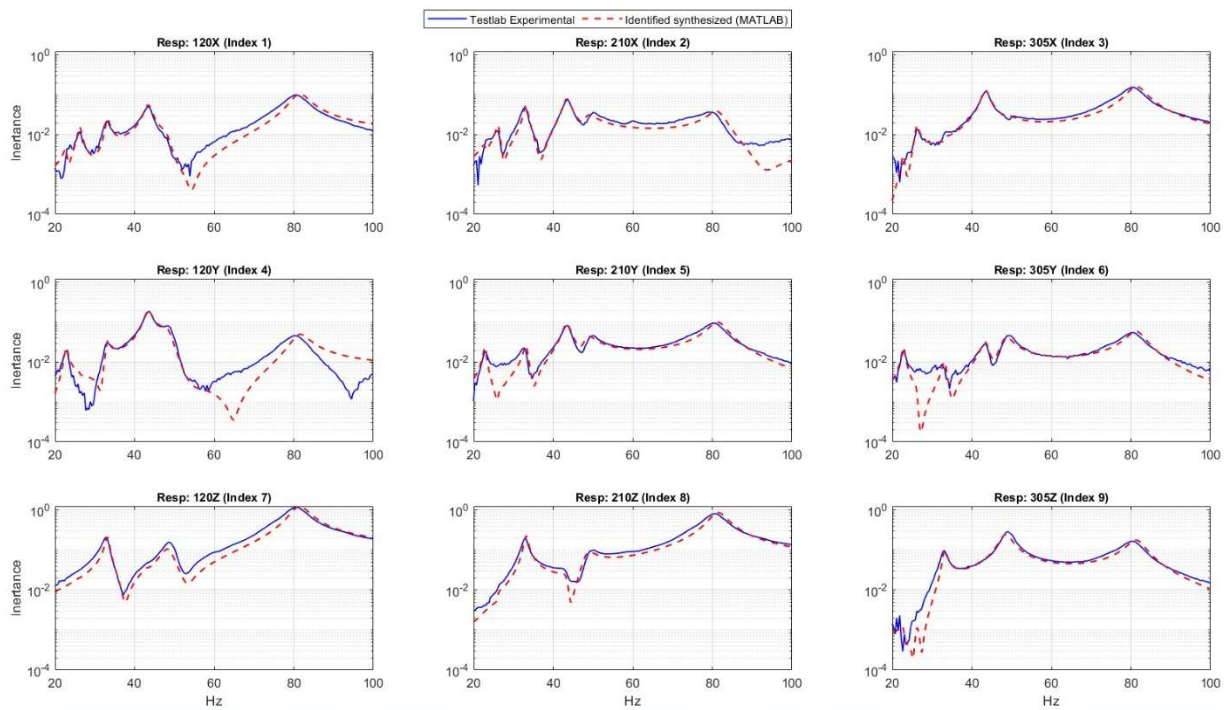

Figure 7.7 :Identified Synthesized MATLAB VS Experimental Testlab FRF comparison the impact is 120Z in low frequency range of interest

7.10 Initial EMA–Romax comparison before model modification

Before modifying the numerical model, the six experimental low-frequency modes were compared with the corresponding Romax modes. This first comparison was used as a diagnostic step to evaluate whether the initial numerical model reproduced the global dynamic behaviour of the mounted powertrain. Differences were observed both in frequency and in the physical similarity of the mode shapes. This indicated that the initial Romax model required further refinement before being used as a reliable representation of the tested assembly. In particular, the low-frequency modes are strongly affected by the stiffness of the rubber mounts, the stiffness of the mounting arms, the boundary condition imposed by the bench, and the mass and inertia distribution of the powertrain. Therefore, the discrepancies observed in the initial comparison were interpreted as an indication that the support system and arm stiffness had to be checked and updated.

Mode	Initial Romax frequency [Hz]	EMA frequency [Hz]	Frequency difference [%]	Interpretation	Initial Romax damping [%]	EMA damping [%]	Dominant motion
1	26.2	22.79	**+14.96%**	Romax too stiff for this motion	30.4	1.80	Translation in Y
2	28.2	26.17	**+7.76%**	Romax slightly stiff	28.2	1.78	Translation in X
3	31.1	33.17	**−6.24%**	Romax slightly flexible	25.6	1.46	Translation in Z
4	33.2	43.40	**−23.50%**	Romax too flexible	24.0	2.05	Rotation around Z
5	43.9	48.48	**−9.45%**	Romax too flexible	18.1	3.08	Rotation around X
6	58.9	81.45	**−27.69%**	Romax too flexible	13.5	2.60	Rotation around Y

Table 7.6 : Initial EMA–Romax comparison before modification

The initial EMA–Romax comparison was performed using the manufacturer's original stiffness set. With this configuration, Romax identified six low-frequency vibration modes, as reported in Table 7.6. However, the frequency agreement with the experimental Testlab results was not satisfactory. The first two numerical modes were higher than the experimental values, while the higher low-frequency modes were generally lower than the corresponding EMA modes. This showed that the model was not simply globally too stiff or globally too flexible. Instead, the discrepancy depended on the direction and physical nature of each mode.

The numerical damping values reported in the preliminary Romax comparison were not used as the primary validation quantity. In this stage, the correlation focused mainly on natural frequencies and mode shapes, because the objective was to validate the stiffness, mass, and support representation of the numerical model. Damping was considered separately as an experimental output and should not be overinterpreted unless the numerical damping model is explicitly defined.

The initial comparison showed that the original stiffness set did not reproduce the experimental low-frequency behaviour with sufficient accuracy. Therefore, the following step was a directional support-stiffness modification, followed by a bearing-stiffness correction when an additional rotor axial-shift mode appeared in the updated numerical model.

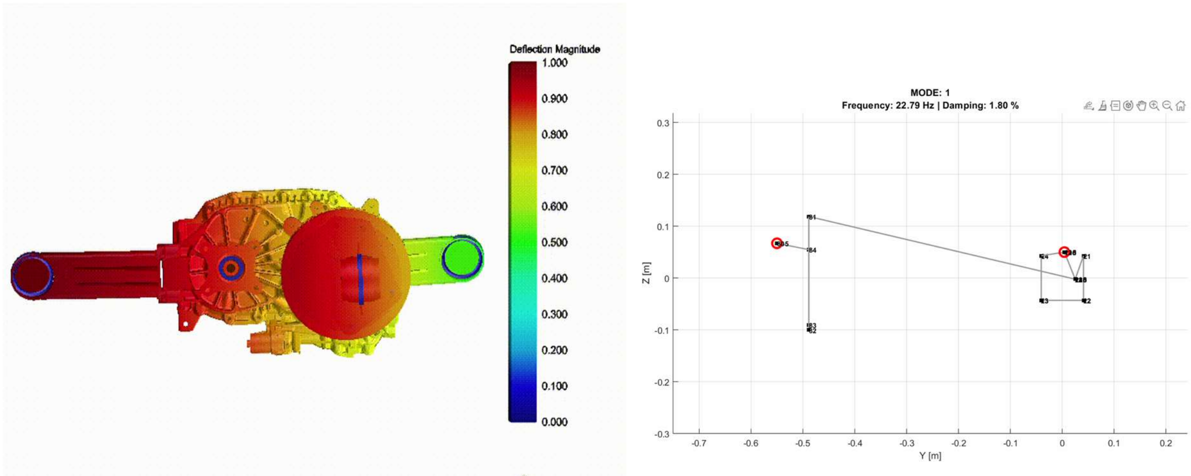

Figure 7.8 : Initial comparison of EMA and Romax mode 1

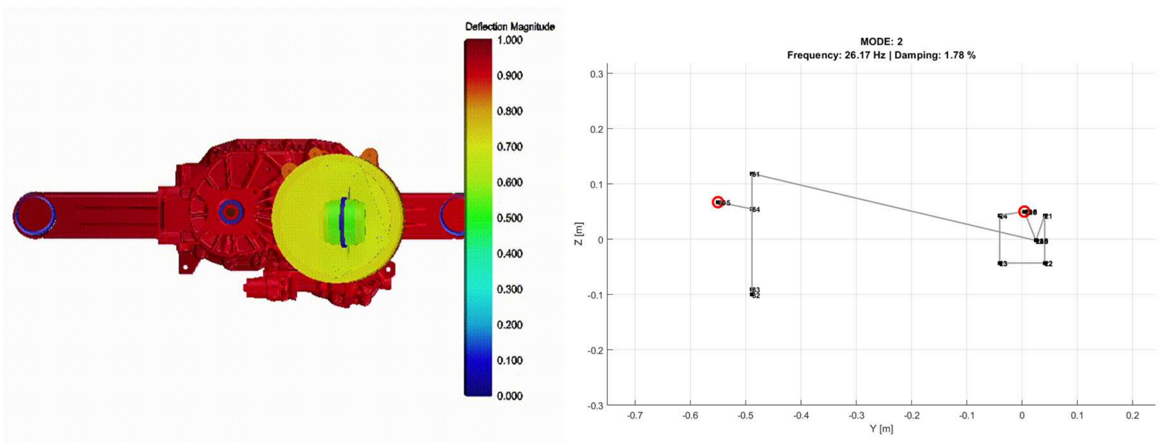

Figure 7.9 : Initial comparison of EMA and Romax mode 2

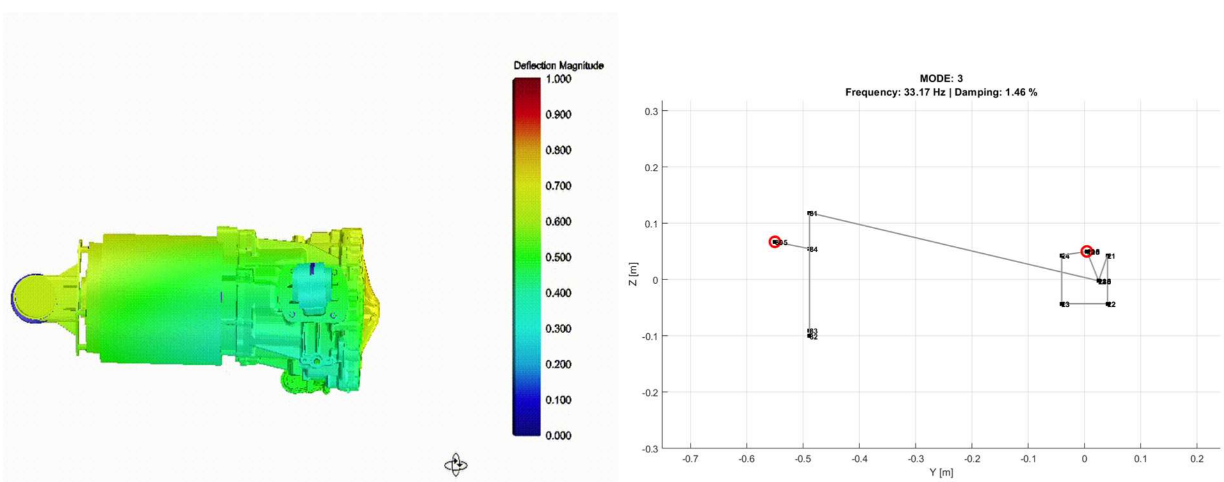

Figure 7.10 : Initial comparison of EMA and Romax mode 3

7.11 Numerical model modification: support-arm, rubber-mount, and bearing stiffness methodology

After the initial EMA–Romax comparison, the numerical model was modified to improve the correlation with the experimental low-frequency modes. The modification focused first on the stiffness representation of the powertrain support system. This was necessary because the low-frequency rigid-body and mount-controlled modes are strongly affected by the stiffness of the rubber mounts, the stiffness of the metallic support arms, and the way these components are represented in Romax.

The purpose of the modification was not simply to force the numerical frequencies to match the experimental ones. The objective was to obtain a model that better reproduced both the frequency values and the deformation patterns observed during the EMA test. For this reason, the updated Romax modes were later evaluated using MAC-based comparison with the experimental mode shapes.

The initial Romax model used the manufacturer's support-stiffness data. However, the manufacturer stiffness values refer to the complete support system, not only to the rubber mount. Each support is composed of a metallic arm and a rubber mount. Therefore, the stiffness reported in the datasheet can be interpreted as the equivalent stiffness of two springs in series: the stiffness of the steel arm and the stiffness of the rubber mount. The stiffness relation is:

$$\frac{1}{k_{support}} = \frac{1}{k_{arm}} + \frac{1}{k_{mount}}$$

where $k_{support}$is the stiffness of the complete support, $k_{arm}$is the stiffness of the metallic arm, and $k_{mount}$is the stiffness of the rubber mount.

This distinction is important for the Romax model. If the steel arm is represented separately in Romax, then the stiffness assigned to the ground connection should represent mainly the rubber mount, not the complete arm–mount system. Otherwise, the compliance of the arm may be counted incorrectly. Therefore, this methodology was used to separate the arm stiffness from the rubber-mount stiffness before defining the support stiffnesses in Romax. In this approach, the FE arm can be imported in Romax, connected to the housing with high-rigidity dummy shafts, and then connected to ground through a dummy shaft with the stiffness of the rubber mount.

The arm stiffness was calculated through finite element analysis. The workflow started from the 2D drawing of the support arm, followed by 3D CAD modelling in SolidWorks, pre-processing and mesh generation, solution in MSC Nastran, and post-processing of the displacement results. The same methodology was applied to the long arm, short arm, and rear arm.

In the FE model, the arm was fixed at the four screw-hole locations. RBE2 elements were used at the centre of the four holes, and all six degrees of freedom were constrained in order to reproduce the clamping condition. At the centre of the rubber-mount hole, an RBE3 element was introduced. This point was used to apply the external unit force. Three unit forces were applied separately in the x, y, and $z$directions because the datasheet provides stiffness values in the three main directions.

For each direction, the solver provides the displacement at the reference point located at the centre of the rubber mount. Since the applied force is equal to 1 N, the static stiffness of the arm can be calculated directly as:

$$k_x = \frac{1}{u_x}$$

$$k_y = \frac{1}{u_y}$$

$$k_z = \frac{1}{u_z}$$

where u_x, u_y, and u_z are the displacements calculated in the corresponding force direction.

After obtaining the arm stiffness, the rubber-mount stiffness was calculated from the series-stiffness relation. This provided the rubber stiffness values that are more suitable for the

Romax ground connections when the metallic arms are represented as structural components. In other words, the support system was separated into two contributions: the metallic arm stiffness and the rubber-mount stiffness.

The stiffness values obtained from this procedure were initially static values. However, the Romax vibration model requires complex stiffness values. Therefore, the static rubber stiffnesses were expressed in complex form by assuming hysteretic damping with a constant loss factor and the corresponding magnitude was evaluated. Loss factor is:

$$\eta = 0.12$$

The modulus of the complex stiffness was written as:

$$k^{*} = k_{static}(1 + ih)$$

and the corresponding magnitude was approximated as:

$$\mid k^{*} \mid = k_{static}\sqrt{1 + h^{2}}$$

This procedure was applied to the rubber stiffnesses of the long arm, short arm, and rear arm. The resulting complex stiffness values were then used as the physical basis for the Romax support-stiffness modification.

The rotational stiffness of the ground connections was treated separately. Since the rotational stiffness values were not specified in the available stiffness datasheets, they were introduced as modelling assumptions. In the initial model, very low rotational stiffness values were assigned in order to avoid imposing an artificially rigid rotational constraint at the support locations. A value of (1000Nmm/rad) was therefore selected as the starting point for the rotational support representation, before the subsequent tuning activity.

Support	Vehicle / Component Directions	Arm stiffness [N/mm]	Complete support stiffness [N/mm]	Calculated rubber mount stiffness [N/mm]
Long arm, front right	Xv / axial	8658.0	296	306.5
Long arm, front right	Zv / radial ver	10062.4	683	732.7
Long arm, front right	Yv / radial hor	189681.3	506	507.4
Short arm, front left	Xv / axial	30048.1	474	481.6
Short arm, front left	Zv / radial vert	29446.4	1063	1102.8
Short arm, front left	Yv / radial hor	345303.9	805	806.9
Rear arm	Xv / radial horizontal	118259.2	805	810.5
Rear arm	Zv / radial vertical	53304.9	1063	1084.6
Rear arm	Yv / axial	19353.6	474	485.9

Table 7.7 : Static arm and rubber-mount stiffness from FE-based methodology

The table shows that the metallic arms are significantly stiffer than the complete support system. Therefore, the global support compliance is mainly governed by the rubber mount rather than by the steel arm. This confirms that separating the rubber stiffness from the arm stiffness is necessary when the arm is represented separately in Romax.

Support	Vehicle / component direction	Rubber complex stiffness [N/mm]
Long arm, front right	Xv / axial	453

Long arm, front right	Yv / radial horizontal	692
Long arm, front right	Zv / radial vertical	935
Short arm, front left	Xv / axial	779
Short arm, front left	Yv / radial horizontal	1284
Short arm, front left	Zv / radial vertical	1779
Rear arm	Xv / radial horizontal	1296
Rear arm	Yv / axial	805
Rear arm	Zv / radial vertical	1754

Table 7.8: Rubber complex stiffness values calculated for Romax

These values represent the rubber complex stiffnesses calculated after separating the steel-arm stiffness from the complete support stiffness. They were used as the physical reference for the support-stiffness update in Romax. However, the final values inserted in Romax were not a simple uniform scaling of these stiffnesses. The final tuning was directional, because the low-frequency modes involve coupled translations and rotations and each mode is affected by a different combination of support directions.

For clarity, the original Romax support-stiffness values and the modified values used after tuning are reported in the following tables.

Support	Axial Xv stiffness [N/mm]	X radial Zv stiffness [N/mm]	Y radial Yv stiffness [N/mm]	Torsional stiffness [Nmm/rad]	X tilt stiffness [Nmm/rad]	Y tilt stiffness [Nmm/rad]
Long arm	455	945	694	1000	1000	1000
Short arm	781	3585	1792	1000	1000	1000
Rear arm	1294	1745	792	1000	1000	1000

Table 7.9: Original Romax support-stiffness values before modification

Support	Axial Xv stiffness [N/mm]	X radial Zv stiffness [N/mm]	Y radial Yv stiffness [N/mm]	Torsional stiffness [Nmm/rad]	X tilt stiffness [Nmm/rad]	Y tilt stiffness [Nmm/rad]
Long arm	200	945	2200	1000	1000	1000
Short arm	400	1285	2200	1000	1000	1000
Rear arm	1294	1745	792	(10^6)	(10^6)	(10^6)

Table 7.10: Modified Romax support-stiffness values used after tuning

Support	Stiffness component	Original value	Modified value	Change
Long arm	Axial stiffness [N/mm]	455	200	−56.0%
Long arm	X radial stiffness [N/mm]	945	945	0.0%
Long arm	Y radial stiffness [N/mm]	694	2200	+217.0%
Long arm	Torsional stiffness [Nmm/rad]	1000	1000	0.0%
Long arm	X tilt stiffness [Nmm/rad]	1000	1000	0.0%
Long arm	Y tilt stiffness [Nmm/rad]	1000	1000	0.0%
Short arm	Axial stiffness [N/mm]	781	400	−48.8%
Short arm	X radial stiffness [N/mm]	3585	1285	−64.2%
Short arm	Y radial stiffness [N/mm]	1792	2200	+22.8%
Short arm	Torsional stiffness [Nmm/rad]	1000	1000	0.0%

Short arm	X tilt stiffness [Nmm/rad]	1000	1000	0.0%
Short arm	Y tilt stiffness [Nmm/rad]	1000	1000	0.0%
Rear arm	Axial stiffness [N/mm]	1294	1294	0.0%
Rear arm	X radial stiffness [N/mm]	1745	1745	0.0%
Rear arm	Y radial stiffness [N/mm]	792	792	0.0%
Rear arm	Torsional stiffness [Nmm/rad]	1000	(10^6)	+10000%
Rear arm	X tilt stiffness [Nmm/rad]	1000	(10^6)	+10000%
Rear arm	Y tilt stiffness [Nmm/rad]	1000	(10^6)	+10000%

Table 7.11: Change from original to modified Romax support stiffness

The comparison shows that the support update was directional. For the long arm, the axial stiffness was reduced from 455 N/mm to 200 N/mm, while the Y radial stiffness was increased from 694 N/mm to 2200 N/mm. For the short arm, the axial stiffness was reduced from 781 N/mm to 400 N/mm, the X radial stiffness was reduced from 3585 N/mm to 1285 N/mm, and the Y radial stiffness was increased from 1792 N/mm to 2200 N/mm. For the rear arm, the translational stiffnesses were kept unchanged, while the rotational stiffnesses were increased from 1000 Nmm/rad to 1.0×10^6Nmm/rad.

This confirms that the modification was not a global stiffness increase or decrease. The changes were introduced component by component and direction by direction in order to improve the low-frequency modal set. The increase of the rear rotational stiffness can be interpreted as a constraint stiffening action, while the changes in the long and short arm translational stiffnesses affect the mount-controlled translational and rotational modes.

The modification of the support stiffness improved the numerical frequency set, but the updated Romax model identified seven low-frequency modes instead of the six modes identified experimentally. According to the later model-checking activity, the additional numerical mode was related to axial shifting of the rotor. This issue was not interpreted as a mounting-arm stiffness problem. Instead, it was corrected separately by increasing the rotor bearing stiffnesses.

Therefore, the final Romax model modification was performed in two main stages. First, the support stiffness representation was updated using the arm–rubber separation methodology described above. Second, the rotor bearing stiffnesses were increased to control the additional axial rotor-shift mode. This distinction is important because the support-stiffness update affects the global mount-controlled modes, while the bearing-stiffness correction mainly affects an internal rotor-related mode.

Step	Model condition	Stiffness set	Result
1	Initial Romax model	Manufacturer/original stiffness values	Six numerical modes identified, but frequency agreement with EMA was not satisfactory
2	Support-stiffness update	Directional modification based on the arm–rubber stiffness separation	Frequency set improved, but seven numerical modes appeared
3	Bearing-stiffness correction	Rotor bearing stiffness increased	Additional axial rotor-shift mode reduced or removed from the low-frequency set
4	Final correlation model	Modified support stiffness + increased bearing stiffness	Six Romax modes selected and compared with six EMA modes using frequency, mode-shape interpretation, and MAC

Table 7.12: Romax model-update sequence

The final stiffness set should therefore be interpreted as a tuned Romax input set based on the physical arm–rubber separation methodology. The mechanical basis for distinguishing the metallic arm stiffness from the rubber-mount stiffness are provided. The final Romax input values were then modified direction by direction during the correlation activity. For this reason, the update is not described as a global increase or decrease of stiffness, but as a directional support-stiffness modification combined with a bearing-stiffness correction.

7.12 Eigenvector extraction and node mapping

To perform a quantitative comparison between EMA and Romax mode shapes, the numerical eigenvectors were extracted at the same physical locations used in the experimental test. The simulation-eigenvector file contains Romax eigenvectors at the accelerometer-reference nodes 120, 210, and 305. These are the same locations used for the low-frequency EMA reference measurements.

Two coordinate representations were prepared. The first one corresponds to the Romax accelerometer reference. The second one corresponds to the EMA reference system. This second representation is required because the experimental accelerometer axes did not always coincide with the numerical axes. In the final MAC calculation, the eigenvectors was compared in a common reference system; otherwise, the MAC values may be artificially reduced or the wrong mode pairing may be selected.

Since three reference frames were involved in the correlation, the EMA reference frame was selected as the common comparison frame. The relationship between the experimental EMA frame, the vehicle frame, and the Romax frame was defined as $X_{EMA} = Y_v = X_{Romax}$, $Y_{EMA} = -X_v = Z_{Romax}$, and $Z_{EMA} = Z_v = Y_{Romax}$. Therefore, before computing the MAC matrix, the Romax eigenvector components were reordered and sign-corrected according to this transformation. This step was necessary to ensure that the EMA and Romax mode-shape vectors described motion in the same physical directions.

For the rigid-body comparison, the translational DOFs used in the MAC calculation were:

$$[120_X, 210_X, 305_X, 120_Y, 210_Y, 305_Y, 120_Z, 210_Z, 305_Z]$$

Rotational components were also extracted for the Romax eigenvectors, but the EMA reference vector was based on translational accelerometer measurements. Therefore, the main MAC calculation for the accelerometer-reference comparison was performed using equivalent translational DOFs only.

The experimental mode-shape vector was constructed from the measured acceleration directions at the selected powertrain nodes. The numerical mode-shape vector was obtained by extracting the Romax eigenvector components at the corresponding nodes and directions. Then the spatial correspondence between the experimental Testlab geometry and the Romax model was defined. The simulation-eigenvectors was then used to assemble the numerical mode-shape matrix.

Before computing MAC, the coordinate systems were checked to ensure that the experimental and numerical directions were consistent.

Data source	Content	Use in correlation
Testlab EMA results	experimental frequencies, damping ratios, mode shapes	experimental reference
Node positions	coordinates of all experimental / comparison nodes	node mapping
Simulation eigenvectors	Romax eigenvectors at selected nodes	numerical mode-shape vectors
MATLAB MAC script	Auto-MAC and Cross-MAC calculation	mode-pair selection
Romax - EMA	modified Romax mode-shape visualization	visual confirmation

Table 7.13: Data used for EMA–Romax mode-shape correlation

DOF group	Experimental source	Numerical source	Used in MAC?
120_X, 120_Y, 120_Z	Accelerometer at long arm	Romax eigenvector at node 120	Yes
210_X, 210_Y, 210_Z	Accelerometer at short arm	Romax eigenvector at node 210	Yes
305_X, 305_Y, 305_Z	Accelerometer at rear arm	Romax eigenvector at node 305	Yes
Rotations ϕx, ϕy, ϕz	Not directly measured by accelerometers	Available in Romax	No, not for translational MAC

Table 7.14: DOFs used for the rigid-body MAC calculation

7.13 MAC-based selection of the final Romax modes

After the modification of the arms and rubber stiffness in the Romax model, seven candidate numerical modes were available in the low-frequency range. These corresponded to 7 Romax modes. However, the EMA procedure identified six relevant low-frequency modes. A direct one-to-one correspondence could therefore not be assumed from the numerical order alone.

The final selection of the Romax modes was performed using the Modal Assurance Criterion. For each EMA mode, the MAC value was computed against the seven modified Romax candidate modes. A high MAC value indicates that experimental and numerical mode shapes have similar spatial deformation patterns. A low MAC value indicates that the modes are not physically equivalent, even if their frequencies are close. The six Romax modes retained in the final comparison were those that showed the best combination of frequency proximity, mode-shape similarity, and MAC value.

This procedure is important because, in a complex mounted assembly, mode order can change after modifying stiffness parameters. A numerical mode may appear close in frequency to an experimental one while representing a different physical motion. For this reason, the final pairing was based primarily on mode-shape similarity and only secondary on frequency order.

The final Romax modes were selected by considering the MAC matrix together with the frequency comparison and the visual interpretation of the mode shapes. This combined approach was necessary because frequency proximity alone can lead to incorrect mode pairing in a complex assembly. In the final selection, six Romax modes were retained because they showed the highest similarity to the six experimental modes. One of the seven modified Romax candidate modes were excluded because it did not provide a sufficiently good correspondence with the EMA mode set.

$$MAC(\phi_{EMA}, \phi_{Romax}) = \frac{|(\phi_{EMA}^{T} . \phi_{Romax})|^2}{(\phi_{EMA}^{T}\phi_{EMA})((\phi_{Romax}^{T}\phi_{Romax})}$$

EMA mode	Romax M1	Romax M2	Romax M3	Romax M4	Romax M5	Romax M6	Romax M7
EMA M1	0.811	0.000	0.243	0.003	0.183	0.043	0.009
EMA M2	0.041	0.713	0.061	0.008	0.008	0.001	0.049
EMA M3	0.015	0.000	0.012	0.897	0.001	0.000	0.048
EMA M4	0.076	0.033	0.113	0.000	0.034	0.002	0.000
EMA M5	0.078	0.003	0.039	0.002	0.005	0.752	0.017
EMA M6	0.009	0.008	0.001	0.000	0.000	0.001	0.960

Table 7.15 : Full MAC matrix between the six EMA low-frequency modes and the seven modified Romax candidate modes

EMA mode	Romax M1	Romax M2	Romax M4	Romax M3	Romax M6	Romax M7	Romax M5
EMA M1	0.811	0.000	0.003	0.243	0.043	0.009	0.183
EMA M2	0.041	0.713	0.008	0.061	0.001	0.049	0.008
EMA M3	0.015	0.000	0.897	0.012	0.000	0.048	0.001
EMA M4	0.076	0.033	0.000	0.113	0.002	0.000	0.034
EMA M5	0.078	0.003	0.002	0.039	0.752	0.017	0.005
EMA M6	0.009	0.008	0.000	0.001	0.001	0.960	0.000

Table 7.16: Sorted MAC matrix after reordering the Romax candidate modes according to the best EMA–Romax correspondence. Romax M5 does not provide the best match for any EMA mode.

EMA mode	Selected Romax M1	Selected Romax M2	Selected Romax M4	Selected Romax M3	Selected Romax M6	Selected Romax M7
EMA M1	0.811	0.000	0.003	0.243	0.043	0.009
EMA M2	0.041	0.713	0.008	0.061	0.001	0.049
EMA M3	0.015	0.000	0.897	0.012	0.000	0.048

EMA M4	0.076	0.033	0.000	0.113	0.002	0.000
EMA M5	0.078	0.003	0.002	0.039	0.752	0.017
EMA M6	0.009	0.008	0.000	0.001	0.001	0.960

Table 7.17 : Final selected MAC matrix after excluding the unmatched Romax candidate mode 5. The diagonal values represent the final EMA–Romax mode pairing used for the low-frequency correlation.

EMA mode	Selected Romax mode	MAC value	Correlation quality	Comment
EMA M1	Romax M1	0.811	Good	Strong similarity; accepted match
EMA M2	Romax M2	0.713	Acceptable / good	Clear best match, but lower than M1 and M3
EMA M3	Romax M4	0.897	Good	Strong similarity; accepted match
EMA M4	Romax M3	0.113	Poor / uncertain	Weak correlation; requires discussion
EMA M5	Romax M6	0.752	Acceptable / good	Clear match with moderate-high MAC
EMA M6	Romax M7	0.960	Excellent	Best-correlated mode

Table 7.18 : Final MAC-based selection of the six Romax modes used for comparison with the six EMA low-frequency modes.

The full MAC matrix shows that six Romax modes were selected from the seven modified Romax candidate modes. The selected numerical modes were Romax M1, M2, M4, M3, M6, and M7. Romax M5 was not retained because it did not provide the highest MAC value for any of the six experimental modes.

The strongest correlation was obtained for EMA M6 and Romax M7, with a MAC value of 0.960. Good correlation was also obtained for EMA M3 with Romax M4 and EMA M1 with Romax M1. EMA M2 and EMA M5 showed acceptable correlation with Romax M2 and Romax M6, respectively.

EMA M4 showed a low maximum MAC value of 0.113, even after sorting the Romax candidate modes. This indicates that the fourth experimental mode is not well represented by the available translational Romax eigenvectors. The low value may be caused by limited spatial resolution, missing rotational information, coordinate-system mismatch, or the presence of a local bending component that is not captured adequately by the selected accelerometer-reference DOFs. Therefore, EMA M4 should be treated as an uncertain mode pair and discussed separately rather than presented as a fully validated match.

7.14 Final low-frequency EMA–Romax correlation

The final low-frequency correlation was obtained after selecting the six Romax modes that best matched the six experimental modes. The correlation was evaluated using three criteria: frequency error, MAC value, and physical interpretation of the mode shape.

The frequency error was computed as:

$$Error[\%] = 100\frac{f_{Romax} - f_{EMA}}{f_{EMA}}$$

A good correlation requires not only a small frequency error, but also a physically consistent mode shape. For this reason, a mode pair was considered reliable only when the deformation pattern observed in Romax was compatible with the experimental mode shape and the MAC value was sufficiently high.

The final comparison confirmed which low-frequency modes were correctly represented by the updated numerical model and which modes still showed discrepancies. Modes with good MAC but frequency error may indicate that the physical deformation pattern is correctly captured but the stiffness or mass level still requires updating. Modes with low MAC indicate a more fundamental mismatch in the mode shape, possibly due to incorrect mode pairing, insufficient spatial resolution, coordinate-system mismatch, or missing flexibility in the numerical model.

EMA mode	EMA frequency [Hz]	EMA damping [%]	Selected Romax mode	Romax frequency [Hz]	Frequency error [%]	MAC	Final interpretation
1	22.79	1.80	Romax M1	20.2	-11.36	0.811	Translation in Y: good shape correlation
2	26.17	1.78	Romax M2	25.0	-4.47	0.713	Translation in X: acceptable/good correlation
3	33.17	1.46	Romax M4	36.0	+8.53	0.897	Translation in Z: good correlation
4	43.40	2.05	Romax M3	29.3	-32.49	0.113	Rotation around Z: poor MAC, uncertain match
5	48.48	3.08	Romax M6	52.5	+8.29	0.752	Rotation around X: acceptable/good correlation
6	81.45	2.60	Romax M7	82.6	+1.41	0.960	Rotation around Y: excellent correlation

Table 7.19 : Final EMA–Romax low-frequency correlation after model modification

The final correlation shows good agreement for most of the low-frequency modes. The strongest correlation is obtained for EMA mode 6 and Romax M7, with a MAC value of 0.960 and a frequency error of only +1.41%. EMA modes 1, 2, 3, and 5 also show acceptable to good mode-shape correlation. EMA mode 4 remains uncertain because its MAC value is only 0.113 and its frequency error is large. Therefore, this mode should not be considered fully validated and requires further investigation, possibly through additional measurement points, verification of coordinate signs, or inclusion of rotational/flexible DOFs in the comparison.

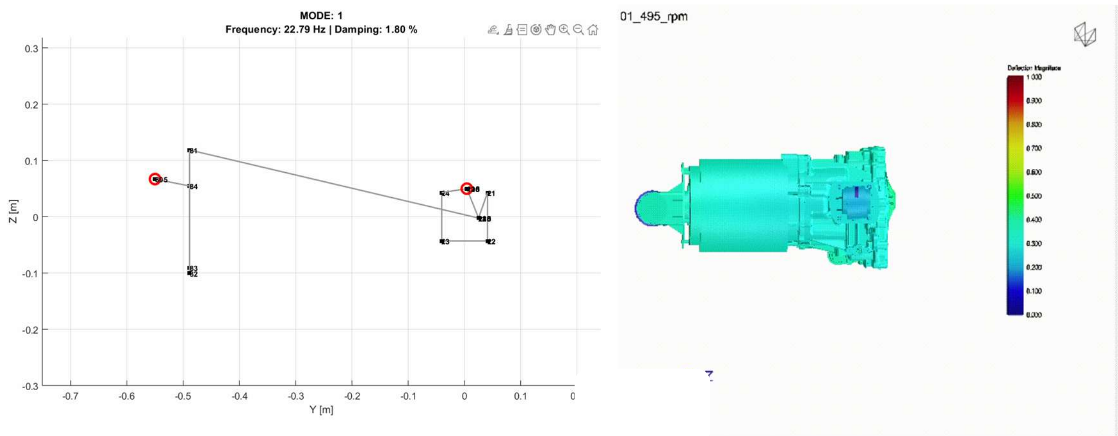

Figure 7.11 : Final EMA mode 1/Romax mode1 -shape comparison

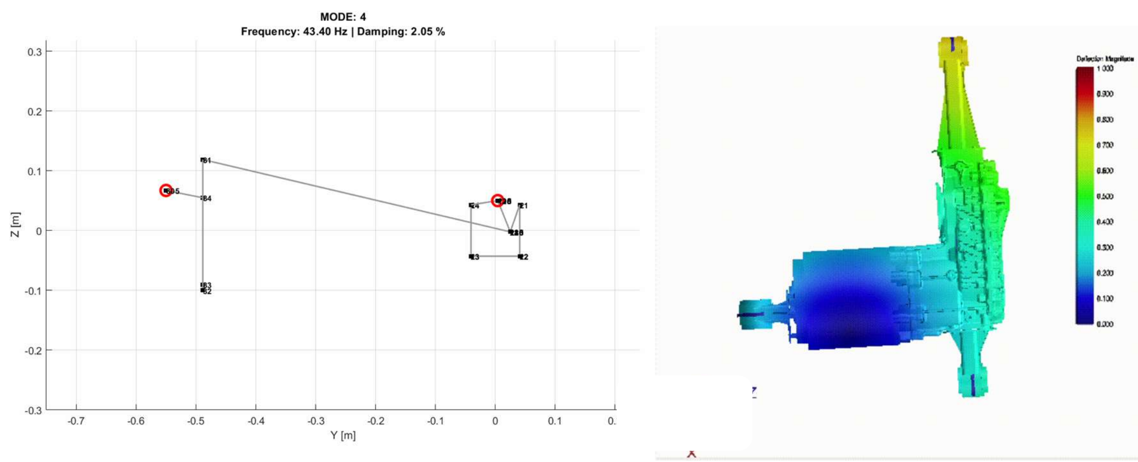

Figure 7.12 : Final EMA mode 4 /Romax mode 3 -shape comparison

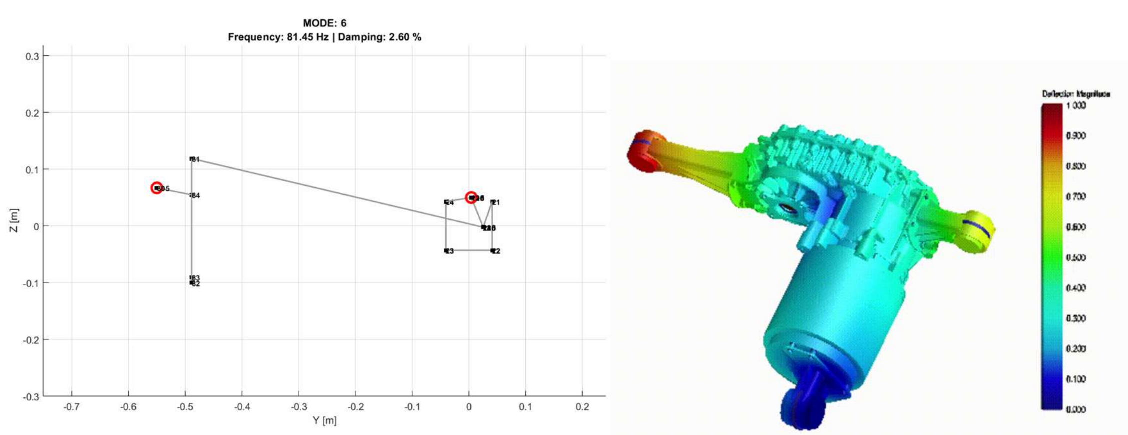

Figure 7.13 : Final EMA mode 6/Romax mode 7 shape comparison

7.15 Discussion of residual discrepancies

Although the modification of the numerical model improved the physical correspondence between EMA and Romax, some discrepancies may remain. These discrepancies must be interpreted by considering both the experimental limitations and the modelling assumptions.

It was recently discovered an error in the datasheet, where some stiffness directions were swapped. This is likely the main reason for the discrepancies observed in the original model and explains why a modification of the initial stiffness values was necessary.

One possible source of discrepancy is the rubber mount stiffness. The low-frequency behaviour of the powertrain is strongly governed by the mount stiffness in the main directions. If the rubber stiffness used in Romax does not correspond to the complex stiffness of the real mounts under the tested preload and frequency range, the predicted rigid-body frequencies will shift.

A second source of discrepancy is mount directionality. Rubber mounts do not generally have the same stiffness in all directions. Incorrect orientation or simplified stiffness representation can modify the coupling between translation and rotation of the powertrain assembly.

A third source is the stiffness of the mounting arms and bolted connections. Even in the low-frequency range, the arms may not behave as perfectly rigid links. If their flexibility is underestimated or overestimated, the bending and torsional mount-controlled modes may not match the experiment.

A fourth source is the boundary condition of the test bench. The bench is designed to be stiff, but it is not an ideal rigid ground. The steel frame, mounting plate, bolted interfaces, and rubber floor isolation can introduce additional compliance that may not be included in the numerical model.

Finally, the experimental mode-shape resolution is limited by the number and location of measurement points. If a mode has local deformation in an area that is not measured, its experimental mode shape may be incomplete. This can reduce the MAC value even when the global motion is physically similar.

7.16 Conclusions of the rigid-body identification chapter

This chapter presented the low-frequency rigid-body and mount-controlled identification of the electric powertrain. Six experimental modes were identified by EMA and classified according to their dominant motion: translation in Y, translation in X, translation in Z, and 3 rotations around Z , X , Y.

An initial comparison with the Romax model was first performed before modifying the simulation parameters. This comparison showed that the numerical model reproduced the general type of low-frequency motions, but the correlation was not sufficient to directly validate the model. Therefore, the numerical model was modified by considering physically meaningful parameters, mainly related to rubber stiffness and mounting-arm stiffness.

After modification, seven Romax candidate modes were available in the low-frequency range. Since the EMA identified six modes, a MAC-based selection was performed to choose the six numerical modes most similar to the experimental ones. The final correlation was therefore based on frequency comparison, visual mode-shape comparison, and MAC values, rather than on mode order alone.

The results of this chapter provide the basis for the next part of the thesis, where the analysis is extended from low-frequency mount-controlled behaviour to the structural modes of the long arm and bulk powertrain.

8 Long Arm and Bulk Powertrain Structural Modes

8.1 Purpose of the structural-mode study

After the low-frequency rigid-body and mount-controlled behaviour was characterized, the analysis was extended to the higher-frequency structural modes of the powertrain assembly. In this range, the response is no longer governed only by the global motion of the powertrain on its rubber mounts. Instead, deformation of the mounting arms, brackets, bolted interfaces, housing, and local structural features become significant.

Long arm is particularly important because it represents one of the main structural paths between the powertrain body and the support system. Its bending stiffness, torsional stiffness, thickness, bolted connections, and boundary conditions can strongly influence the modal behaviour of the complete assembly. For this reason, the long-arm modes and their correlation with the Romax model are central to the structural validation stage of the thesis.

The purpose of this chapter is therefore to identify the experimental structural modes of the powertrain, compare them with the corresponding numerical modes, and evaluate whether discrepancies are related to local flexibility of the long arm or to more global modelling assumptions. This chapter is separated from the rigid-body chapter because the physical mechanisms are different: Chapter 7 focused mainly on rubber-mount and global inertia effects, while this chapter focuses on structural flexibility.

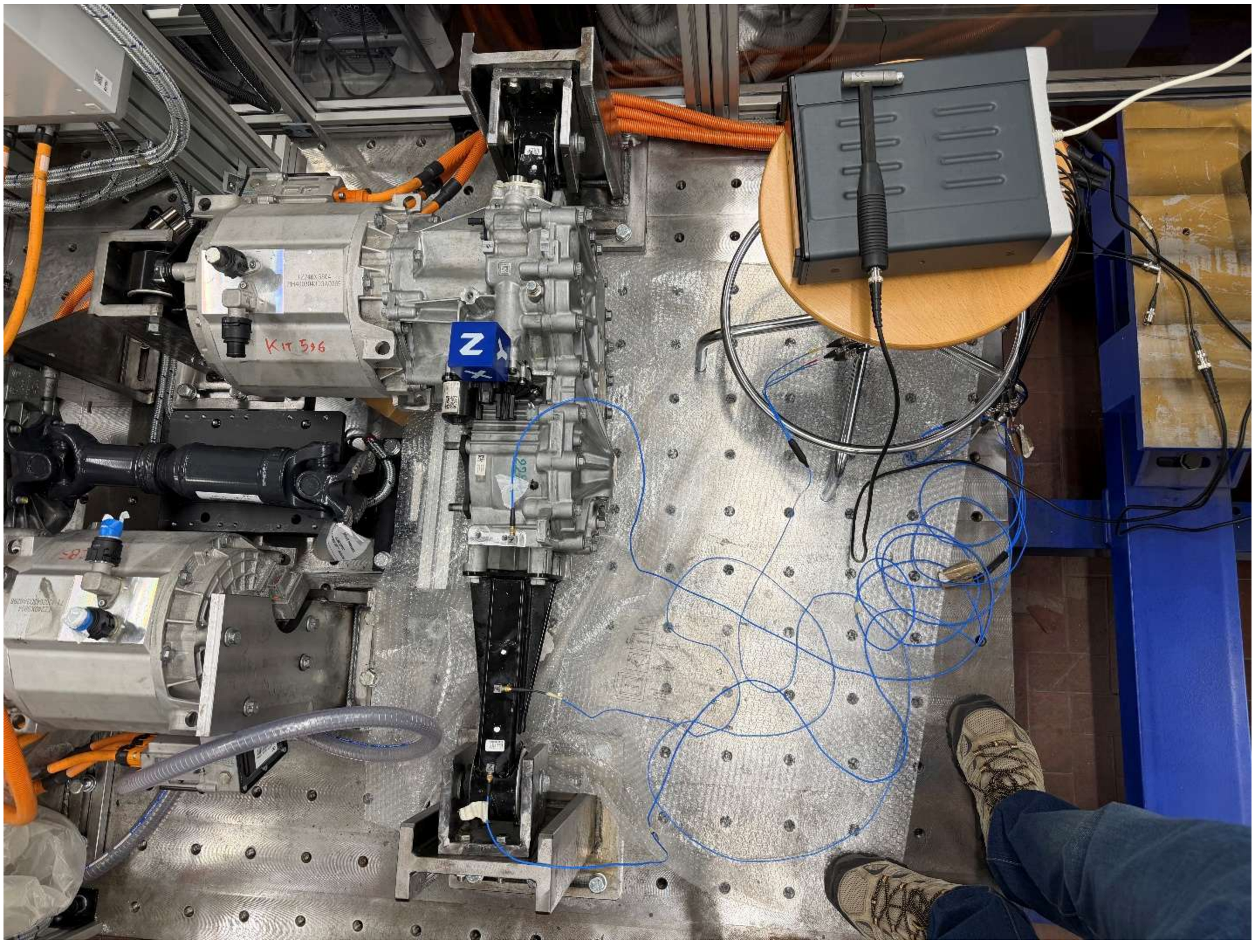

Figure 8.1 : powertrain experimental setup- Long Arm study

8.2 Extended measurement geometry for structural-mode analysis

For the structural-mode analysis, the experimental geometry was extended beyond the three accelerometer-reference nodes used in the rigid-body comparison. The objective was to improve the spatial description of the long arm, short arm, rear arm, and powertrain body so that local deformation patterns could be visualized and compared with the numerical mode shapes.

The extended geometry consisted of 21 nodes distributed over the main structural regions of interest. Several nodes were placed on different faces of the long arm to make bending and torsional deformation visible. Additional nodes were included on the powertrain body to represent the global deformation of the assembly. This 21-node layout is therefore used in the structural-mode chapter, while the rigid-body chapter used only the accelerometer-reference DOFs at nodes 120, 210, and 305 for MAC comparison.

Although some nodes, such as 120, 210, and 305, appear in both chapters, their role is different. In Chapter 7, they were used as reference response coordinates for low-frequency EMA–Romax correlation. In the present chapter, they are part of a larger geometry used to interpret structural deformation of the mounting arms and powertrain body.

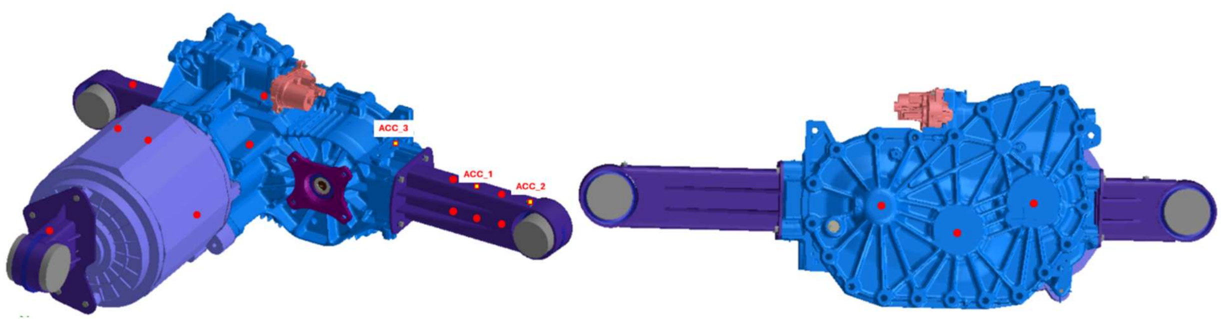

Figure 8.2: Additional nodes for structural-mode analysis showed with red dots

Node	x [m]	y [m]	z [m]	Position
10	-0.039	0.014	0.078	Long arm mount
105	0.100	0.004	0.050	Long arm horizontal face
110	0.150	0.004	0.050	Long arm horizontal face
115	0.200	0.004	0.050	Long arm horizontal face
120	0.250	0.004	0.050	Long arm horizontal face
125	0.100	0.0249	-0.0022	Long arm right face
130	0.150	0.0249	-0.0022	Long arm right face
135	0.200	0.0249	-0.0022	Long arm right face

145	0.100	-0.0249	0.0022	Long arm left face
150	0.150	-0.0249	0.0022	Long arm left face
155	0.200	-0.0249	0.0022	Long arm left face
210	-0.600	0.004	0.050	Short arm horizontal face
305	-0.425	-0.550	0.067	Rear arm horizontal face
40	-0.290	-0.041	0.122	Powertrain body
41	-0.339	-0.269	0.136	Powertrain body
42	-0.417	-0.270	0.149	Powertrain body
43	-0.407	0.106	0.025	Powertrain body
44	-0.289	0.111	-0.025	Powertrain body
45	-0.157	0.137	0.013	Powertrain body
46	-0.277	-0.108	0.042	Powertrain body
47	-0.264	-0.319	0.015	Powertrain body

Table 8.1: Extended 21-node geometry for structural-mode analysis

8.3 Acquisition settings and hammer-tip selection

The long-arm structural test was configured to cover a higher frequency range than the low-frequency rigid-body analysis. For this reason, the acquisition bandwidth was set to 3200 Hz. This value was selected because the structural modes of the long arm and powertrain body were expected to occur at significantly higher frequencies than the mount-controlled modes discussed in Chapter 7.

The number of spectral lines was set to 4096, giving a frequency resolution of 0.78 Hz and an acquisition time of 1.28 s. This configuration provided a suitable compromise between frequency resolution and acquisition duration. The resolution was sufficiently fine to identify the main structural resonances, while the acquisition time was appropriate for an impact-based test in the selected bandwidth.

The input signal was processed using a force-exponential window with a cutoff of 0.4%, while the response signal was processed using an exponential window with 100% decay. These windows were used to reduce leakage effects after the impact and to improve the quality of the frequency-domain FRFs.

The FRF estimator was set to H1, which is commonly used in impact testing when the input force is considered cleaner than the measured response and the response may contain noise. The measurement was performed using three averages with explicit accept, meaning that each impact was checked before being accepted into the averaged FRF.

A roving-hammer strategy was used. The accelerometers remained fixed at selected response locations, while the hammer was moved between the selected excitation points. This strategy avoided changing the sensor mass distribution during the test and allowed several input coordinates to be measured efficiently.

A metal hammer tip was selected for this test. This choice was made because the objective was to excite the higher-frequency structural modes of the long arm and powertrain body. Compared with softer tips, the metal tip produces a shorter contact duration and therefore provides higher-frequency excitation content. This made it more suitable for the long-arm structural-mode study, where the target was not limited to low-frequency rigid-body motion.

Parameter	Value	Reason
Bandwidth	3200 Hz	covers the higher-frequency structural-mode range
Spectral lines	4096	provides detailed frequency discretization
Frequency resolution	0.78 Hz	sufficient for structural resonance identification
Acquisition time	1.28 s	suitable for impact testing in the selected bandwidth
Input window	Force-exponential	reduces leakage after hammer impact
Input cutoff	0.4%	limits the force window after the impulse
Response window	Exponential	improves decay of measured response
Response decay	100%	applied to the response signal
FRF estimator	H1	suitable when response noise is expected
Number of averages	3	improves repeatability
Averaging mode	Explicit accept	allows manual rejection of poor impacts
Increment strategy	Roving hammer	keeps accelerometers fixed and moves excitation point
Hammer tip	Metal tip	increases high-frequency excitation bandwidth

Table 8.2: Acquisition settings for the long-arm structural test

8.4 Data-quality checks: PSD, coherence, and measurement acceptance

During the long-arm experiment, the quality of the measured data was checked before accepting the FRFs for modal identification. This step was necessary because impact testing is sensitive to double hits, insufficient input force, overloads, local disturbances, and poor signal-to-noise ratio. The main quality indicators used during the experiment were the input force signal, response signal, input PSD, response PSD, instantaneous FRF, averaged FRF, coherence, and input level indicators.

Before the measurement, the bandwidth check in Testlab was used to verify that the hammer input provided enough energy over the selected frequency range. The PSD of the hammer force was inspected to ensure that the force spectrum remained useful over most of the 3200 Hz bandwidth. This check was especially important because the long-arm test was focused on structural modes, which occur at higher frequencies than the rigid-body and mount-controlled modes discussed in Chapter 7.

The input spectrum was used to verify the useful excitation bandwidth of the hammer impact. During the test, a practical −6 dB criterion was applied as suggested during the experimental activity. The reference level was taken from the low-frequency part of the force spectrum, where the hammer input had its highest and most stable energy content. A −6 dB drop corresponds approximately to a reduction of the force amplitude to 50% of its reference level:

$$20\log_{10}\left(\frac{F}{F_{\mathrm{ref}}}\right) = -6$$

$$\frac{F}{F_{\mathrm{ref}}} = 10^{-6/20} \approx 0.50$$

Therefore, the frequency at which the force spectrum drops by 6 dB was used as an estimate of the upper limit of useful excitation energy. This check was not used for damping estimation; it was used only to verify whether the hammer impact supplied enough input energy over the identification range.

In the example shown in Figure 8.4, the maximum low-frequency PSD level is approximately −25.78 dB. The −6 dB reference level is therefore:

$$-25.78 - 6 = -31.78\ \mathrm{dB}$$

The intersection between this horizontal level and the force PSD curve occurs at approximately 2958.78 Hz. This value is close to the selected 3200 Hz bandwidth, indicating that the metal hammer tip provided sufficient excitation energy over most of the selected structural-mode frequency range.

The −6 dB bandwidth check was not used alone. It was combined with the coherence check. The useful bandwidth measurement was considered valid only where the input force still contained sufficient energy and the input-output consistency remained high. In practice, coherence values higher than approximately 0.9 were desired over the identification range. The coherence display zoomed between 0.7 and 1.0 to inspect this high-coherence region more clearly. Local coherence drops near antiresonances were interpreted with caution, because the response magnitude is very small in those regions and the signal-to-noise ratio naturally decreases.

During the measurement phase, Testlab displayed several plots simultaneously. The input time signal was checked to verify that the hammer impact had the correct pulse shape and did not contain a double hit. The response time signal was checked to confirm that the accelerometers measured a clear vibration response. The input PSD and response PSD were monitored to verify that the excitation and response contained sufficient frequency content. The instantaneous FRF was used to check the immediate result of each impact, while the averaged FRF and coherence were used to assess the quality of the accepted measurements.

In the long-arm structural test, the time response was checked together with the PSD, FRF, coherence, and input-level indicators. Compared with the low-frequency rigid-body test, the response contains higher-frequency content and decays over a shorter time interval. This behaviour is consistent with the use of a metal hammer tip and the higher acquisition bandwidth selected for the structural-mode analysis.

In general, coherence values close to 1 indicate a reliable linear relationship between the hammer input and the measured acceleration response. However, local drops in coherence were not automatically considered measurement errors. In several cases, coherence drops occurred near antiresonance regions, where the FRF magnitude becomes very small and the signal-to-noise ratio decreases. Therefore, coherence was interpreted together with the FRF magnitude and phase, rather than used alone as a rejection criterion.

The input-level indicators were also checked during the test. The channels were expected to remain in the green region, indicating that the signal level was suitable and that no overload occurred. Measurements were rejected and repeated when abnormal PSD behaviour, double impact, overload, poor input level, or poor coherence outside antiresonance regions was observed.

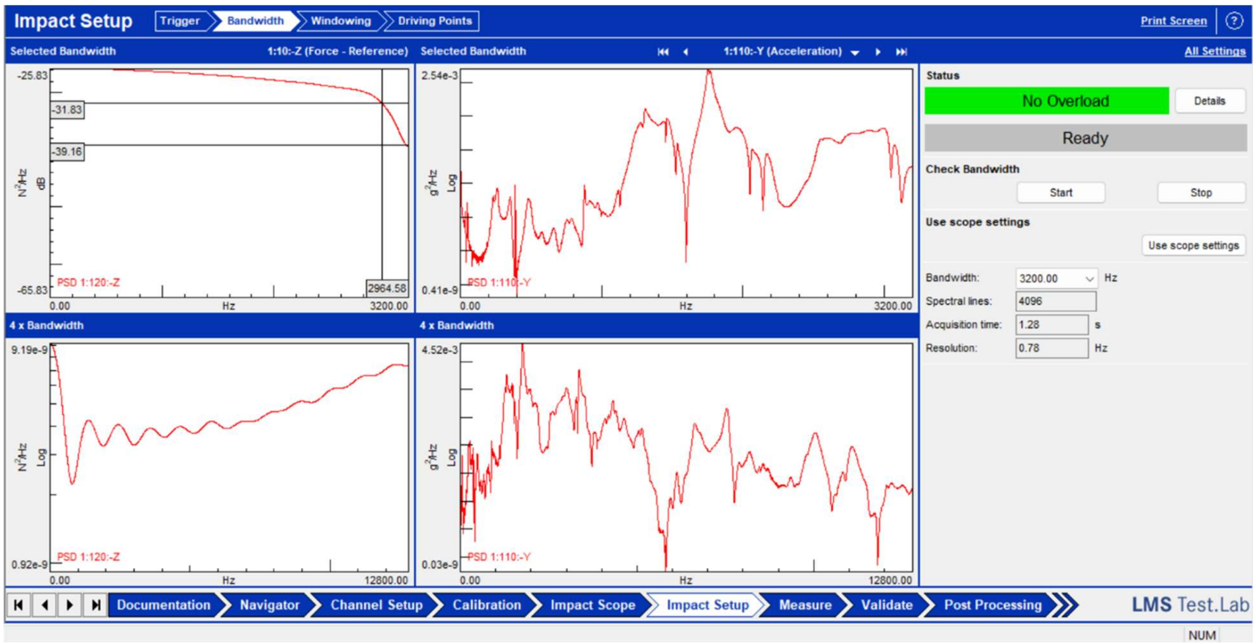

Figure 8.3: Impact setup and PSD bandwidth check

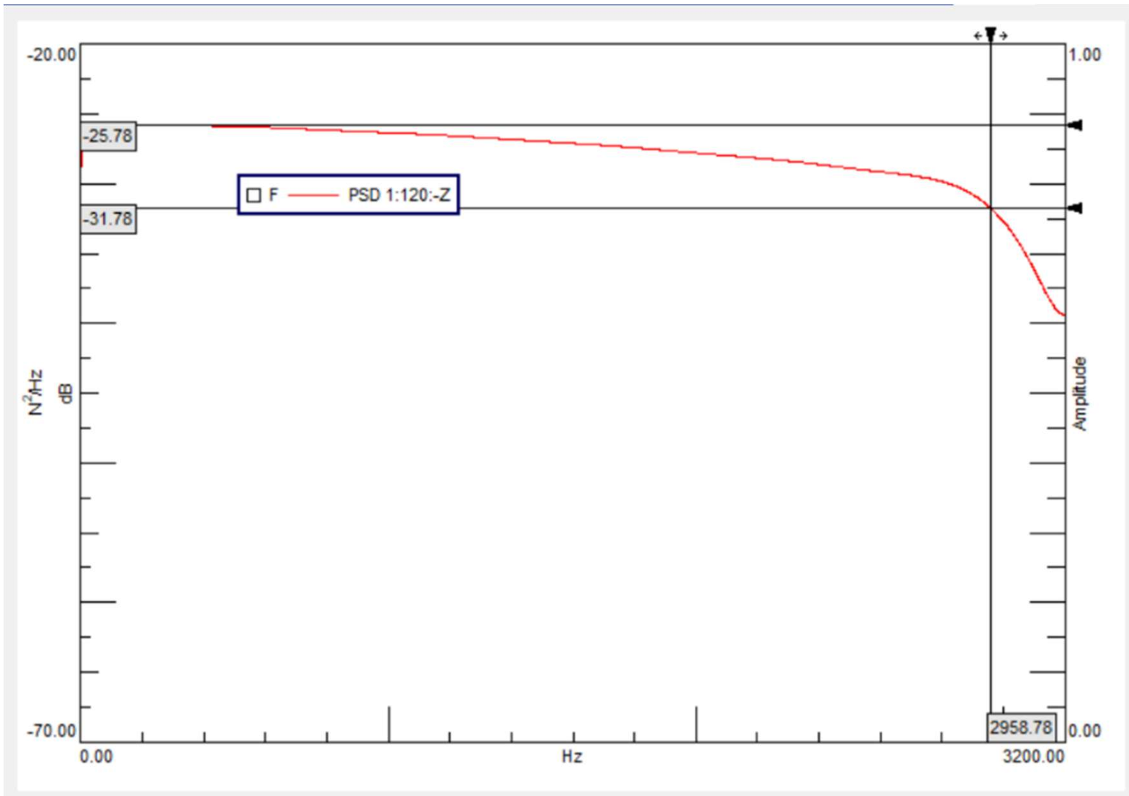

Figure 8.4: PSD-based excitation bandwidth check

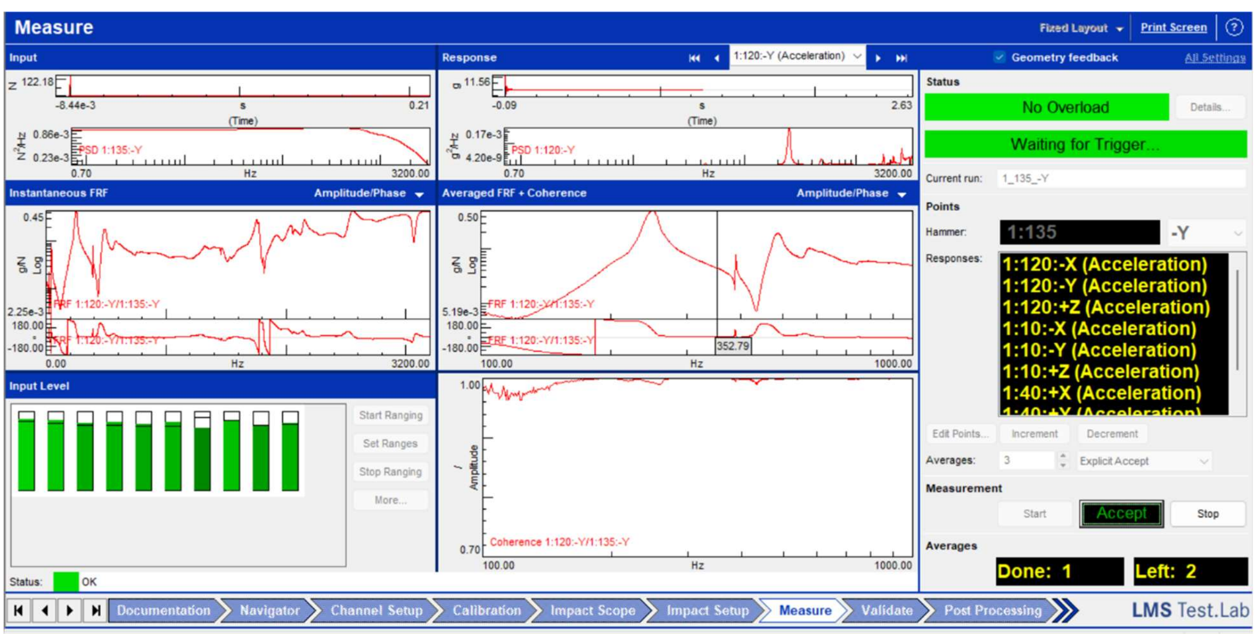

Figure 8.5: Measurement monitoring during the long-arm impact test

Check	Purpose	Acceptance logic
Input force pulse	Detect double impacts or poor hammer strikes	Accept only single, clean impacts
Response time signal	Verify that the structure responded clearly	Reject if response is weak or disturbed
Input PSD / force spectrum	Verify hammer excitation bandwidth	Accept if the input force remains sufficiently high over the identification range
−6 dB force bandwidth	Estimate where force amplitude drops to about 50% of its low-frequency level	Useful bandwidth should cover most of the structural-mode range
Response PSD	Verify response frequency content	Accept if structural response is visible
Instantaneous FRF	Check each individual impact	Reject if the FRF is abnormal
Averaged FRF	Evaluate repeatability after accepted impacts	Accept if peaks are stable and repeatable
Coherence	Verify input-output consistency	Coherence should remain high, preferably above 0.9, except local drops near antiresonances
Input level indicators	Avoid overload or weak signals	Channels should remain in the green range
Measurement status	Verify acquisition condition	Accept only when no overload or double-impact issue is present

Table 8.3: Data-quality criteria used during the long-arm structural test

These quality checks ensured that the structural-mode identification was based on reliable FRFs. The combination of PSD bandwidth verification, coherence monitoring, explicit impact acceptance, and input-level control reduced the risk of including poor measurements in the final averaged FRF dataset.

8.5 FRF validation for the structural-mode range

After the data-quality checks, the identified modal model was validated by comparing the experimental FRFs with the synthesized FRFs generated from the identified modal parameters. This comparison was performed for several Z-direction input-output combinations among nodes 10, 110, and 120 on the long arm.

The purpose of this comparison was to verify whether the selected structural modes were able to reproduce the measured dynamic behaviour. The synthesized FRFs are not expected to match every local irregularity of the experimental curves because the experimental data include noise, local effects, residual contributions, and high-frequency effects not fully captured by the selected modal set. However, the synthesized FRFs should reproduce the main resonance regions and the global trend of the measured FRFs.

Representative comparisons show satisfactory agreement in the main structural resonance regions. This confirms that the identified modal parameters are suitable for mode-shape interpretation and for the subsequent EMA–Romax comparison. The full set of FRF comparisons is reported in the appendix, while only representative cases are included in the main chapter.

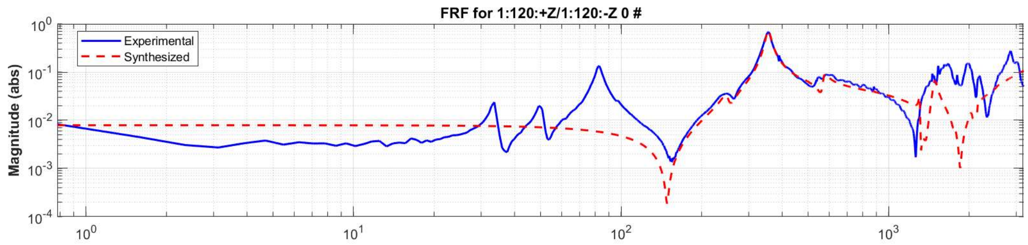

Figure 8.6: Experimental and synthesized FRF comparison 120Z / 120Z

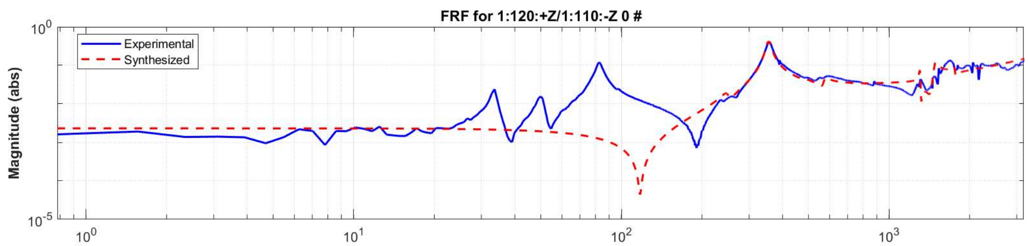

Figure 8.7: Experimental and synthesized FRF comparison for 120Z / 110Z

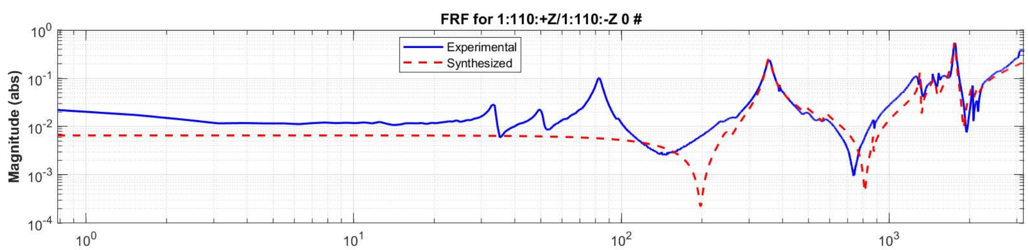

Figure 8.8: Experimental and synthesized FRF comparison for 110Z / 110Z

Figure	Response node / direction	Excitation node / direction	Purpose
Fig. 8.6	120Z	120Z	collocated validation at the long-arm end region
Fig. 8.7	120Z	110Z	cross-FRF along the long arm
Fig. 8.8	110Z	110Z	collocated validation at an intermediate long-arm point

Table 8.4: Representative FRF comparisons used for structural-mode validation

Overall, the FRF comparisons confirm that the synthesized FRFs reproduce the dominant structural resonance regions of the long arm. This supports the reliability of the modal parameters used in the structural-mode analysis. The remaining discrepancies are attributed to measurement noise, residual modal contributions, local flexibility not fully represented by the selected modes, and the complexity of the assembled powertrain structure.

8.6 Experimental structural modal results

The structural modal identification was performed in Testlab using the measured FRF dataset. The stabilization diagram was used to select stable poles, and the final mode list was accepted only after checking the corresponding damping values, FRF contribution, and mode-shape plausibility.

Eleven experimental modes were identified in the structural-mode range. These modes represent a combination of long-arm deformation, powertrain-body motion, and coupled motion between the mounting arms and the main assembly. The first four identified structural modes were observed at 250 Hz, 355 Hz, 482 Hz, and 573 Hz. The complete preliminary frequency comparison with Romax is reported in Table 8.5.

The mode shapes were extracted from Testlab and compared with the corresponding Romax mode shapes. This comparison is necessary because the structural modes cannot be validated by frequency alone. Similar frequencies do not necessarily imply similar deformation patterns, especially in a complex assembled structure such as the electric powertrain.

Mode number	EMA frequency [Hz]	Romax frequency [Hz]	Frequency error [%]
1	250	151	-39.60
2	355	260	-26.76
3	482	392	-18.67
4	573	408	-28.80
5	873	509	-41.70

6	1306	597	-54.29
7	1485	628	-57.71
8	1757	793	-54.87
9	2046	846	-58.65
10	2155	874	-59.44
11	2535	925	-63.51
12	:	990	:

Table 8.5: Preliminary EMA–Romax frequency comparison for structural modes

8.6.1 Experimental modal damping analysis

The damping trend of the long-arm structural modes was also evaluated using a Rayleigh damping representation. This plot was used to check whether the experimentally identified damping ratios followed a reasonable frequency-dependent trend in the structural-mode range.

Compared with the low-frequency rigid-body modes, the long-arm structural modes involve more local deformation of the arm, mounting interfaces, and powertrain body. For this reason, the Rayleigh damping curve should be interpreted as an approximate global damping representation, not as a complete physical damping model of all local dissipation mechanisms. The plot is useful mainly to identify the overall damping trend and to detect possible outlier modes with unusually high or inconsistent damping.

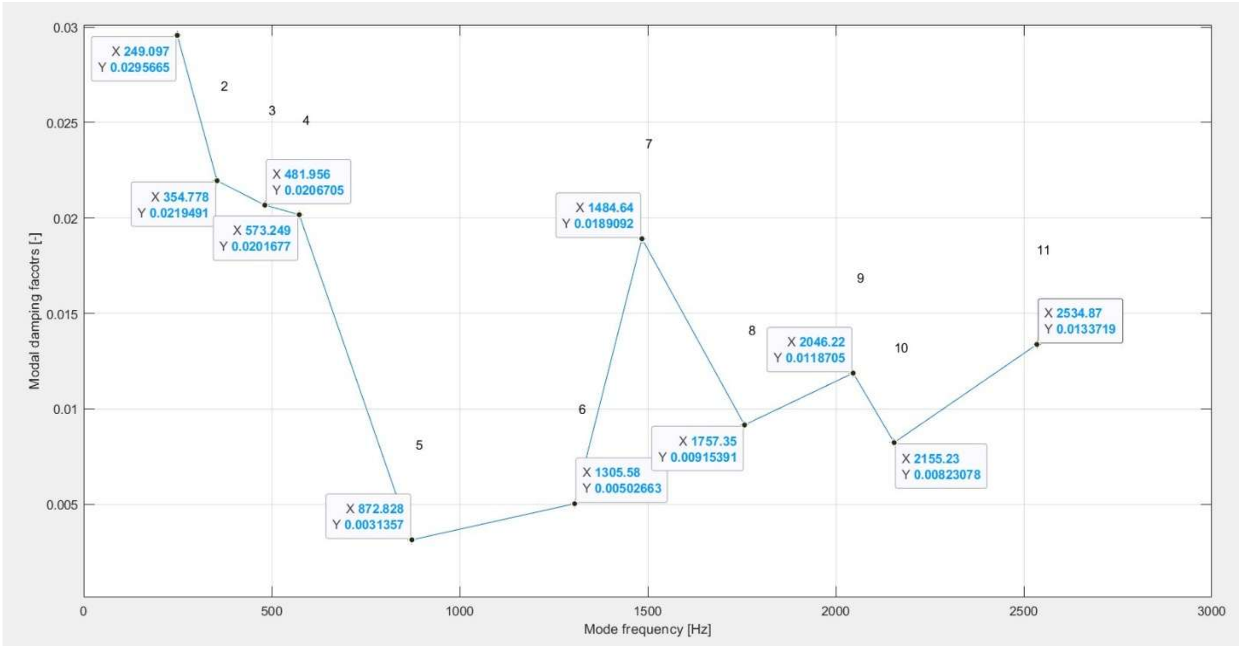

Figure 8.9: Rayleigh Damping with frequency and number of modes for long Arm

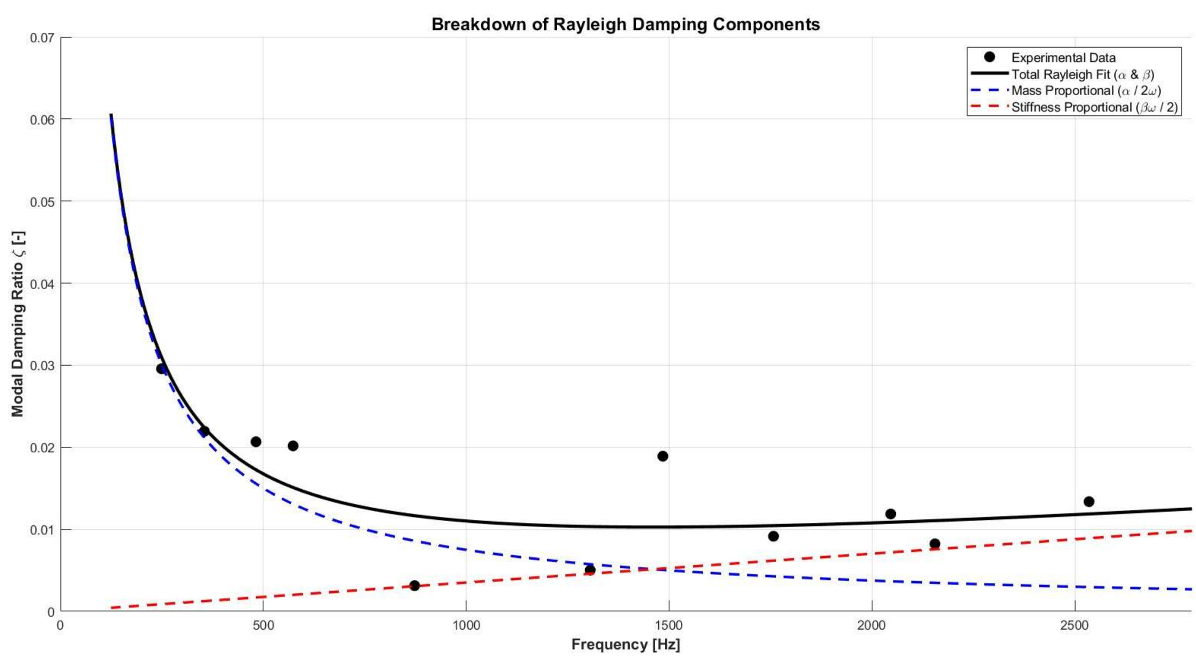

*Figure 8.10: Rayleigh Damping identification curve considering only 1st and 2nd term of the proportional damping equation and the sum of the curves **α**=94.2564 & **β**=1.1191e-6*

The preliminary comparison shows that the Romax model predicts the structural modes at lower frequencies than the experimental results. This indicates that the numerical model may be globally or locally more flexible than the tested structure. However, this conclusion must be treated carefully because modes should not be paired only by order. A reliable correlation requires visual mode-shape comparison and, when possible, MAC-based validation. The current draft already notes that the table is preliminary and that mode pairing cannot be based on frequency order alone.

8.7 EMA–Romax mode-shape comparison

The experimental mode shapes extracted from Testlab were compared with the corresponding Romax mode shapes. The purpose of this comparison was to determine whether the numerical model reproduced the same physical deformation patterns observed experimentally.

The comparison was performed by considering both frequency proximity and visual similarity of the animated mode shapes. In the long-arm structural range, visual comparison is especially important because several modes may involve coupled deformation of the long arm, short arm, rear arm, and powertrain body. Therefore, mode order alone was not considered sufficient for validation.

Representative EMA–Romax mode-shape comparisons are included for the first experimental structural mode at 250 Hz compared with the Romax mode at 151 Hz, and the second experimental mode at 355 Hz compared with the Romax mode at 260 Hz. The remaining mode-shape images are placed in the appendix.

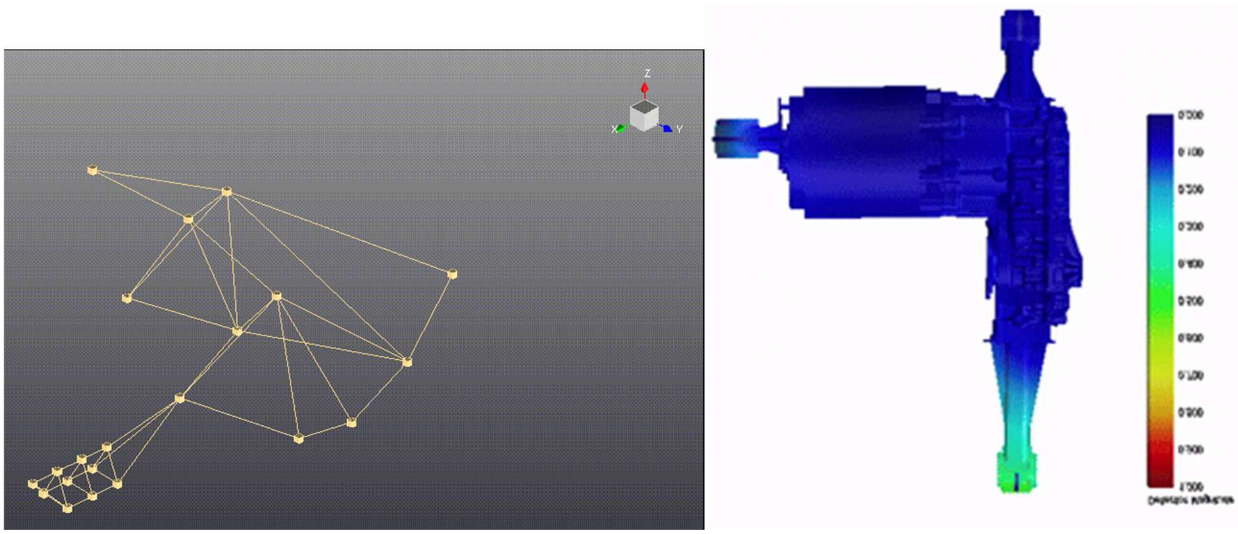

Figure 8.9: EMA mode at 250 Hz versus Romax mode at 151 Hz

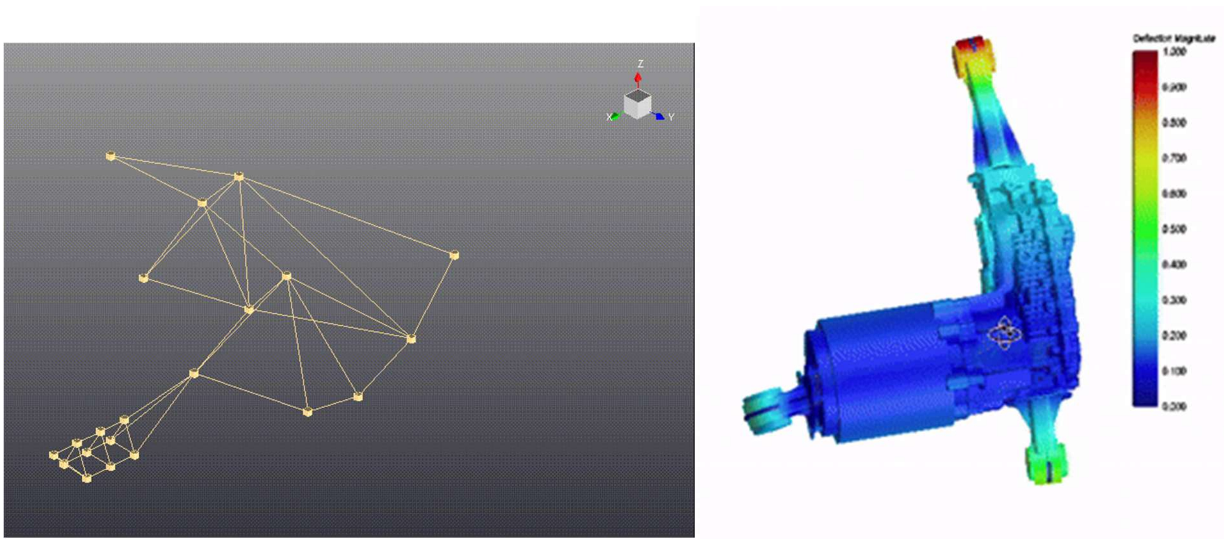

Figure 8.10: EMA mode at 355 Hz versus Romax mode at 260 Hz

8.8 Long-arm thickness sensitivity in Romax and SolidWorks

A long-arm thickness sensitivity study was performed to investigate whether the stiffness of the long arm could explain part of the discrepancy between the experimental and numerical structural modes. Since natural frequencies depend on the ratio between stiffness and mass, changing the thickness of the long-arm plate modifies the bending and torsional stiffness and therefore shifts the modal frequencies.

The thickness effect was studied in both Romax and SolidWorks, but with different modelling assumptions. In SolidWorks, the long arm was isolated from the powertrain and treated as an independent cantilever-like component. The fixed boundary condition was applied at the screw-hole region, because these holes represent the connection points between the long arm and the rest of the assembly. This simplified model was useful for understanding the local stiffness effect of the long arm itself.

In Romax, the long arm was not isolated. It was part of the complete powertrain assembly, so the boundary condition was not equivalent to a fixed cantilever end. The whole assembly can move, and the long arm interacts with the powertrain body, mounts, and other structural components. Therefore, the frequency change caused by modifying the long-arm thickness in Romax represents the effect of thickness variation within the full assembled system.

The comparison between the SolidWorks and Romax thickness studies is important because it shows the difference between local component behaviour and assembled-system behaviour. In SolidWorks, the thickness change mainly affects the isolated bending and torsional stiffness of the arm. In Romax, the same change affects the coupled modes of the complete powertrain. Therefore, the two models are not expected to give identical frequency shifts, but together they help interpret whether the long arm is a dominant contributor to the structural-mode discrepancy.

Aspect	SolidWorks model	Romax model
Modelled structure	isolated long arm	complete powertrain assembly
Boundary condition	fixed at screw-hole region	coupled to full assembly and mounts
Main purpose	evaluate local arm stiffness effect	evaluate assembled-system frequency shift
Physical assumption	cantilever-like simplification	coupled structural dynamics
Expected result	local bending/torsion frequency change	global/coupled mode frequency change

Table 8.6: Difference between SolidWorks and Romax thickness studies

In addition to the full-system Romax analysis, a simplified modal study of the long arm was carried out in SolidWorks in order to investigate the influence of plate thickness on the natural frequencies of the component. In this simplified approach, the long arm was treated as an isolated cantilever-like structure, so that the local structural sensitivity to thickness variation could be studied separately from the global powertrain dynamics.

The SolidWorks model was created using the long-arm geometry shown in Figure 8.11. The component consists of a flange plate, a tubular body, and reinforcing ribs connecting the flange to the cylindrical section. Compared with the Romax model, this simplified model does not represent the interaction with the complete powertrain assembly. Its purpose is therefore not to reproduce the full experimental behaviour, but rather to provide a local structural interpretation of how thickness variation affects the complex stiffness of the long arm.

For the boundary conditions, the long arm was assumed to be fixed at the flange attachment region. More specifically, the fixed boundary condition was applied at the four bolt holes used for the screw connection, as shown in Figure 8.12. This choice was made to represent the constraint introduced by the mounting interface in a simplified but physically meaningful way. In this respect, the SolidWorks model differs from the Romax model. In Romax, the long arm is part of the complete powertrain system, and the entire assembly is free to move according to the mount and structural dynamics. Therefore, in Romax the long arm is not fixed as an isolated component, whereas in SolidWorks the fixed-hole condition was intentionally introduced to obtain a cantilever-type approximation.

The material of the SolidWorks model was defined as linear elastic isotropic steel. The main material properties used in the model were an elastic modulus of $210000\ \mathrm{N/mm^2}$, a Poisson's ratio of 0.3, and a mass density of $7850\ \mathrm{kg/m^3}$. These values were considered sufficient for a first-order structural sensitivity study focused on the variation of natural frequencies with thickness.

The finite element discretization was performed using a solid mesh, as shown in Figure 8.13. A blended curvature-based mesh was adopted in order to capture the geometry of the tubular section, ribs, and flange with sufficient accuracy. In particular, a maximum element size of 8 mm and a minimum element size of 2.66664 mm were used. The final mesh contained 4761 nodes and 13921 elements. The mesh quality was considered acceptable for this preliminary modal study, with 86.8% of the elements having an aspect ratio smaller than 3 and no elements with an aspect ratio greater than 10. After defining the geometry, material, boundary conditions, and mesh, a modal analysis was performed. The first modes predicted by the simplified SolidWorks model are illustrated in table 8.7.

The results of this SolidWorks study were then compared with the Romax thickness-sensitivity trend. The comparison is useful because it highlights the difference between a local isolated-component model and a full-system model. In SolidWorks, the frequency variation is mainly driven by the local stiffness and mass distribution of the long arm itself, whereas in Romax the same variation is influenced by the coupling with the surrounding powertrain structure and by the global system dynamics.

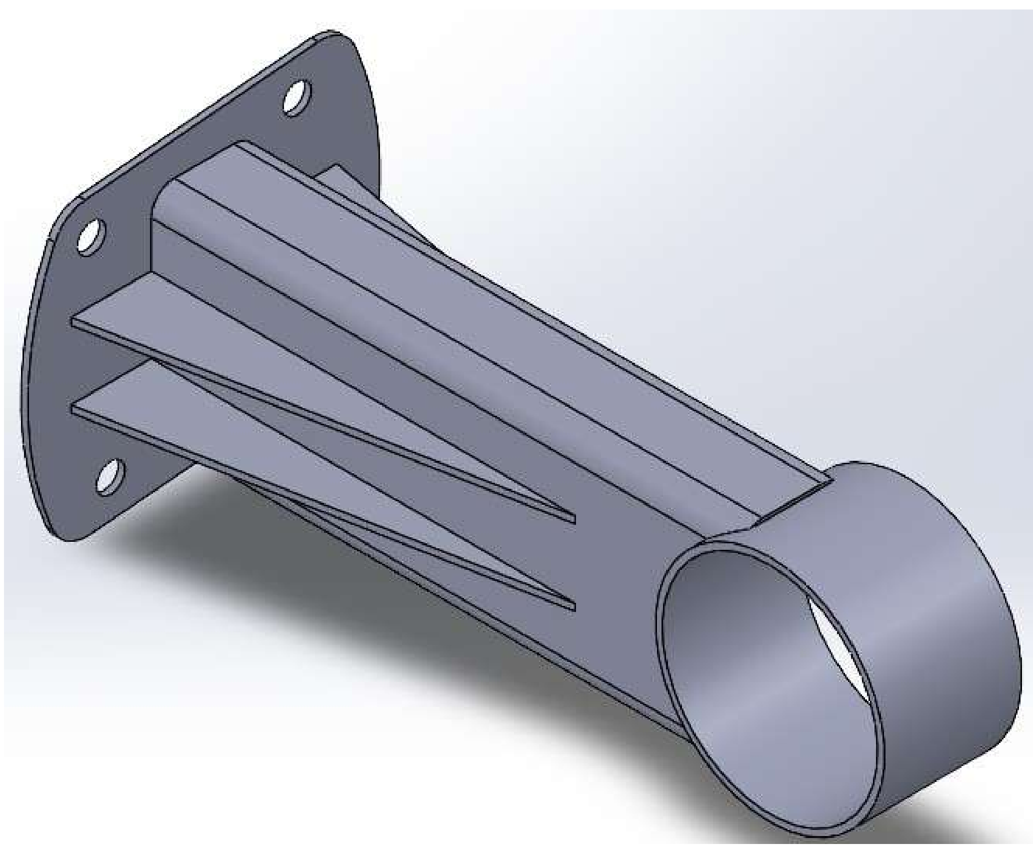

Figure 8.11: Geometry of the isolated long arm used in SolidWorks modal study.

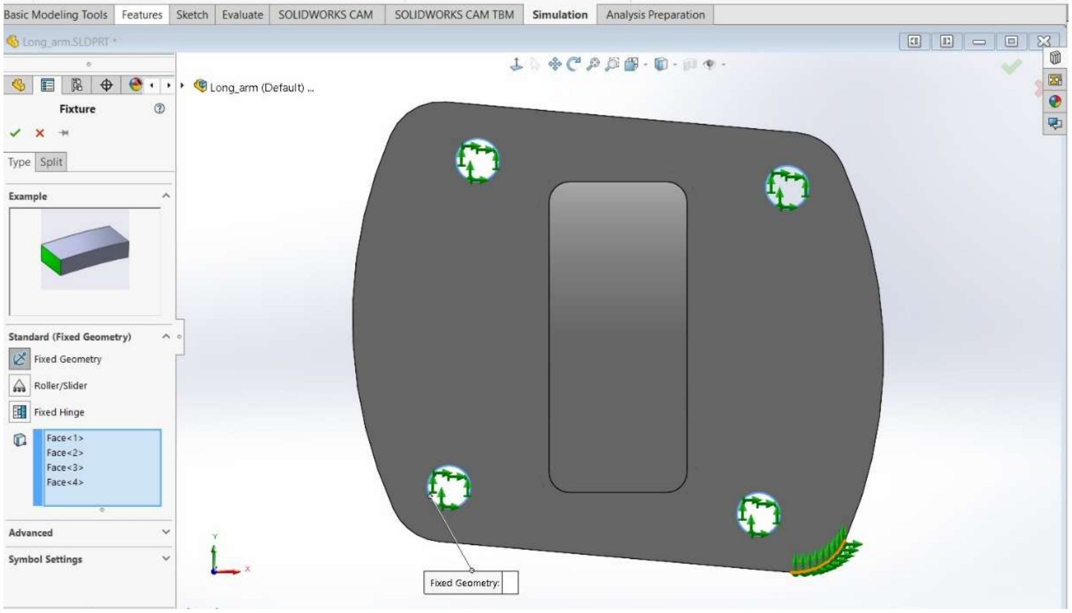

Figure 8.12: Fixed boundary condition applied at the four flange bolt holes in the SolidWorks model.

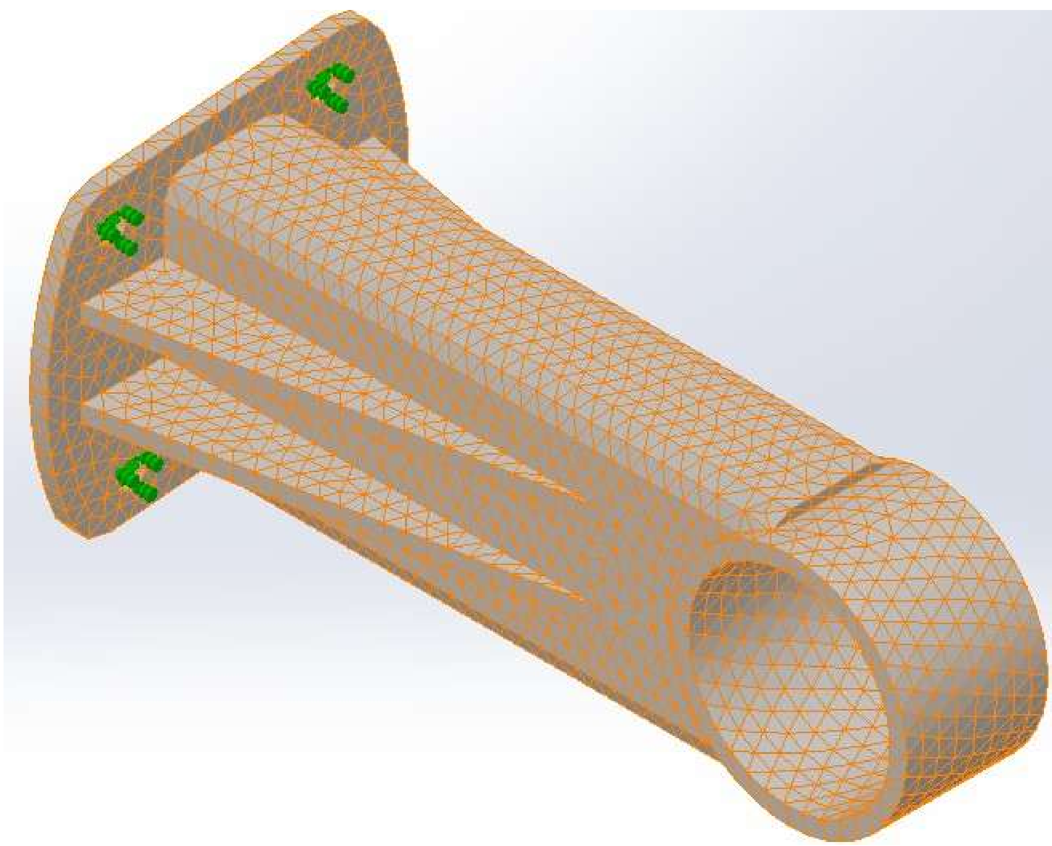

Figure 8.13: Finite element mesh of the simplified SolidWorks long-arm model.

Mode/Width	5mm (Nom.)	4mm (-10%)	3mm (-20%)	6mm (+10%)	7mm (+20%)
1	500.74 Hz	454.36 Hz	413.93 Hz	542.73 Hz	574.05 Hz
2	545.03 Hz	488.10 Hz	441.04 Hz	591.44 Hz	627.06 Hz
3	2055.6 Hz	1851.4 Hz	1723.3 Hz	2117.1 Hz	2167.9 Hz
4	2096.8 Hz	1992.2 Hz	1872 Hz	2257.2 Hz	2352.4 Hz
5	2130.0 Hz	1997 Hz	1911.6 Hz	2379.8 Hz	2588.7 Hz

Table 8.7: Isolated long-arm thickness modification in SolidWorks

Mode / Width	5mm (NOM.)	7mm (+20%)
9 (Long Arm 1st)	150.9 Hz	155.7 Hz
10 (Long Arm 2nd)	155.2 Hz	160.3 Hz

Table 8.8: Long-arm thickness modification in Romax for 5mm and 7 mm respectively

8.9 Discussion

The long-arm structural analysis shows that the discrepancy between EMA and Romax cannot be interpreted only through frequency values. The experimental and numerical mode shapes must also be compared because the same frequency range may contain different deformation patterns. The FRF validation confirmed that the experimental modal model reproduces the main measured dynamic behaviour. The PSD and coherence checks also supported the quality of the measured dataset. Therefore, the observed EMA–Romax discrepancies are more likely related to modelling assumptions than to poor experimental data.

The long-arm thickness sensitivity suggests that the stiffness of the long arm does not have a visible effect on the predicted structural frequencies. However, the effect depends strongly on the modelling boundary condition. In the isolated SolidWorks model, the arm behaves similarly to a cantilever beam fixed at the screw-hole region. In Romax, the long arm is part of the complete powertrain assembly, and its deformation is coupled with the rest of the system.

This means that the long arm cannot be updated only as an isolated component without considering the assembled boundary conditions. A physically meaningful model update should consider the long-arm thickness or stiffness together with bolted-joint stiffness, mount stiffness, mass distribution, and the compliance of the powertrain support system.

9 Conclusions and Future Work

9.1 Conclusions

This thesis developed and applied a roving-hammer Experimental Modal Analysis workflow for the modal characterization and numerical validation of an electric powertrain. The objective was to obtain reliable experimental modal data and use it to evaluate and improve the correlation of the Romax numerical model, especially for the low-frequency mount-controlled behaviour and the higher-frequency structural response.

The workflow was first verified on a cantilever beam. This preliminary test allowed the complete measurement and post-processing procedure to be checked on a simple structure before applying it to the powertrain. The beam study confirmed the reliability of the roving-hammer acquisition, FRF estimation, PolyMAX modal identification, FRF synthesis, reciprocity verification, frequency comparison, and MAC-based validation. It also showed the importance of practical experimental effects such as accelerometer mass loading, finite clamp stiffness, and fixture compliance. After model updating, the beam average frequency error was reduced from $9.60\%$to 2.11%, confirming that physically meaningful parameter adjustment can improve experimental–numerical correlation.

The validated workflow was then applied to the electric powertrain. In the low-frequency range, six experimental modes were identified between 22.79 Hzand 81.45 Hz. These modes represented the main rigid-body and mount-controlled translations and rotations of the assembly. The initial comparison with Romax showed that the discrepancy was not caused by a simple global stiffness error; instead, the differences were direction-dependent and related to the representation of the support system.

For this reason, the Romax model was updated through a physically based support-stiffness methodology. The metallic mounting arms and rubber mounts were treated as stiffnesses in series, and the calculated rubber stiffness values were converted into complex stiffness values using a hysteretic loss factor. The final update also included a bearing-stiffness correction to reduce the influence of an additional axial rotor-shift mode. The updated model gave a better correlation for several low-frequency modes. The best agreement was obtained for EMA mode 6 and Romax M7, with $MAC = 0.960$and a frequency error of $+1.41\%$. EMA mode 3 also showed strong correlation with $MAC = 0.897$. However, EMA mode 4 remained weakly correlated, showing that some rotational or coupled behaviour still requires further modelling improvement.

The thesis also investigated the higher-frequency structural behaviour of the long arm and the bulk powertrain. In this range, eleven experimental modes were identified between approximately 250 Hzand 2535 Hz. The preliminary comparison showed that Romax generally predicted the structural modes at lower frequencies than the experiment. This indicates that the structural-frequency range is more sensitive to local flexibility, bolted interfaces, assembled boundary conditions, and long-arm modelling assumptions.

Overall, the thesis achieved its main objective by establishing a complete experimental–numerical validation procedure for an electric powertrain. The results show that reliable validation cannot be based only on frequency comparison. FRF quality, coherence, synthesized FRF agreement, reciprocity, mode-shape visualization, MAC values, and physical interpretation must be considered together. The final outcome is a repeatable EMA-based methodology that can support future Romax model refinement and electric powertrain NVH development.

9.4 Future work

Future work should focus on improving the spatial resolution of the experimental mode shapes by increasing the number of accelerometers and measuring points. This would allow local deformation, rotational behaviour, and coupled modes to be identified more accurately, especially in the powertrain housing and support regions. The experimental campaign could also be extended to investigate the local structural modes of the short arm and rear arm, and also complete the long arm analysis.

9.5 Final remark

The thesis confirms that roving-hammer EMA is a powerful tool for validating the modal behaviour of an assembled electric powertrain. The method provides direct experimental information about natural frequencies, damping ratios, FRFs, and mode shapes. When combined with MATLAB post-processing and MAC-based comparison, it becomes an effective framework for evaluating and improving numerical models such as Romax.

The final low-frequency results show that the updated Romax model captures several important mount-controlled modes with acceptable or good correlation, while the remaining discrepancies identify where future modelling improvements should focus. The structural-mode study further shows that higher-frequency discrepancies require careful interpretation of local flexibility and assembled boundary conditions. Therefore, the main outcome of the work is not only a set of experimental modal results, but a complete validation methodology that can support future electric powertrain model refinement and NVH development.

10 Appendix A - MATLAB code structure

MATLAB scripts:

```
%%  Data Reading
if exist('./github_repo', 'dir')
    addpath('./github_repo');
else
    warning('Directory github_repo not found. Please ensure readuff.m is added to the system path.');
end
file_unv = 'Real_modes_powertrain_LF.unv';
if exist(file_unv, 'file')
    data = readuff(file_unv);
else
    error('File %s not found!', file_unv);
end
```

```
%% Geometry Plot
node_names = data{1, 3}.nodeN;
node_coord_x = data{1, 3}.x;
node_coord_y = data{1, 3}.y;
node_coord_z = data{1, 3}.z;

figure;
plot3(node_coord_x,node_coord_y,node_coord_z,'sq-');
text(node_coord_x,node_coord_y,node_coord_z,num2str(node_names))
title('Geometry'); grid on
```

```
% Modal Properties
PhiX = []; PhiY = []; PhiZ = [];
fn_vet = []; zita_vet = [];
for count_idx = 1:numel(data)
    if data{count_idx}.dsType == 55 && isfield(data{count_idx}, 'modeFreq')
        % Save frequency and Damping Ratio
        fn_vet = [fn_vet; data{count_idx}.modeFreq];
        zita_vet = [zita_vet; data{count_idx}.mode_v_damping_ratio];

        PhiX = [PhiX, data{count_idx}.r1(:)];
        PhiY = [PhiY, data{count_idx}.r2(:)];
        PhiZ = [PhiZ, data{count_idx}.r3(:)];
    end
end
```

```matlab
%% Proportional Damping Identification
% Formula: zeta_r = a * (1 / (2*wr)) + b * (wr / 2)

wr = 2 * pi * fn_vet; % Natural frequencies in rad/s
zeta = zita_vet;      % Damping ratios from Testlab

% 1. Set up the A matrix (12x2) and b vector (12x1)
% Column 1: coefficients for alpha (a) -> 1 / (2*wr)
% Column 2: coefficients for beta (b)  -> wr / 2
A = [1./(2*wr), wr./2];
B = zeta;

% 2. Solve the overdetermined system using pinv (Pseudo-inverse)
% x_sol = [a; b]
x_sol = pinv(A) * B;
% x_sol= A \ B;
alpha_LS = x_sol(1); % Mass proportional coefficient (a)
beta_LS = x_sol(2);  % Stiffness proportional coefficient (b)
```

```matlab
% 2. Calculate Auto MAC Formula
for i = 1:num_modes
    for j = 1:num_modes
        v1 = Phi(:, i);
        v2 = Phi(:, j);

        % MAC Formula: |(v1^H * v2)|^2 / ((v1^H * v1) * (v2^H * v2))
        num = abs(v1' * v2)^2;
        den = (v1' * v1) * (v2' * v2);

        MAC_matrix(i, j) = num / den;
    end
end
```

11 Appendix B - Additional experimental plots

Beam additional reciprocity FRFs

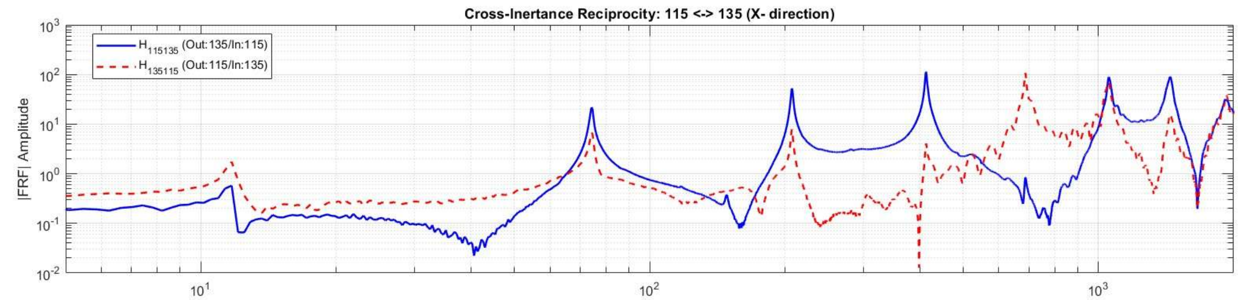

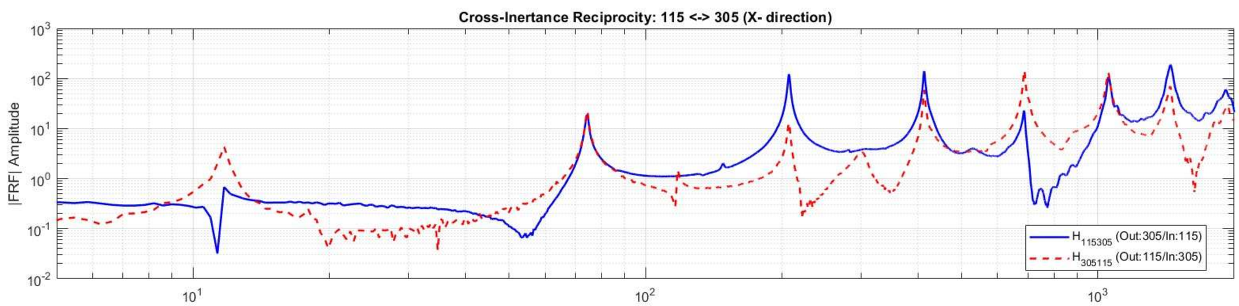

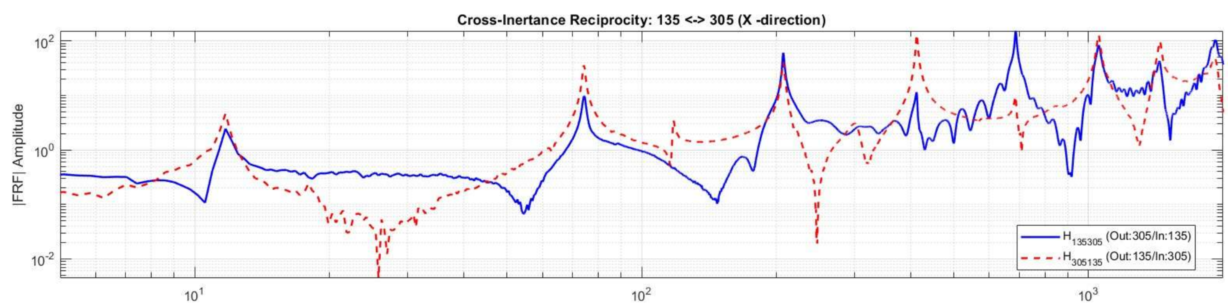

Remaining Romax mode shapes of the beam after mass modification of the sensors

3rd mode

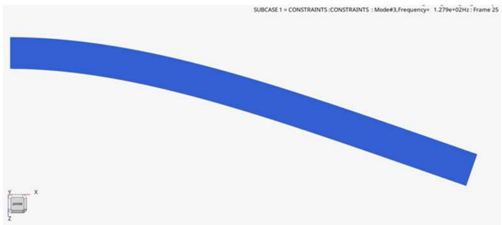

5th mode

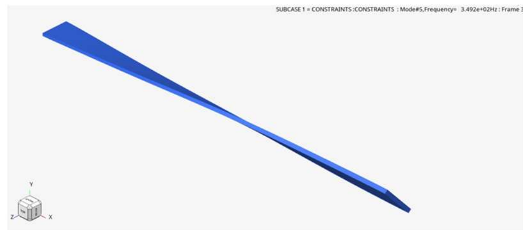

6th mode

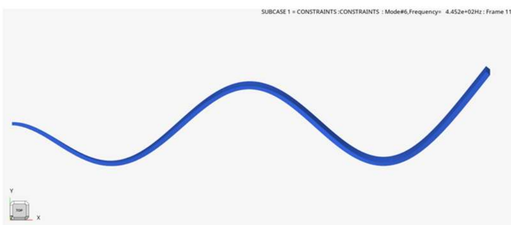

7th mode

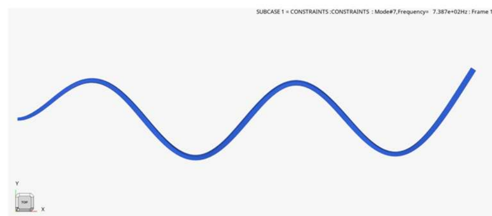

8th mode

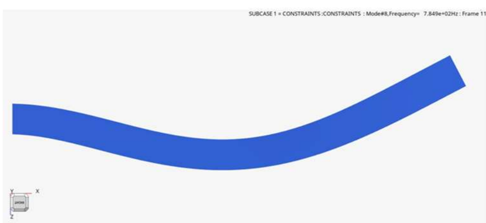

9th mode

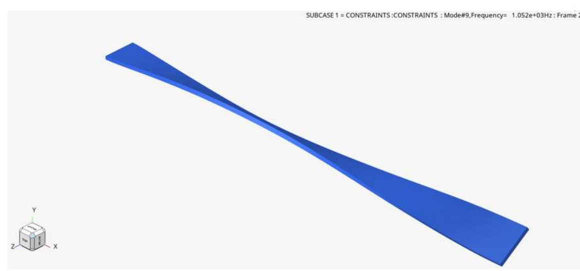

10th mode

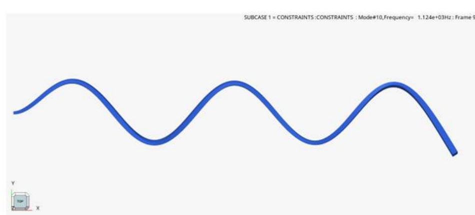

12 References

[1] Hua, X., Thomas, A., and Shultis, K. "Recent progress in battery electric vehicle noise, vibration and harshness." Science Progress, 104(1), 2021. DOI: 10.1177/00368504211005224.

[2] Horváth, K., and Zelei, A. "Simulating Noise, Vibration, and Harshness Advances in Electric Vehicle Powertrains: Strategies and Challenges." World Electric Vehicle Journal, 15(8), 367, 2024.

[3] Masri, J., Amer, M., Salman, S., Ismail, M., and Elsisi, M. "A survey of modern vehicle noise, vibration, and harshness: A state-of-the-art." Ain Shams Engineering Journal, 15(10), 102957, 2024. DOI: 10.1016/j.asej.2024.102957.

[4] Holehouse, R., et al. "Integrated approach to NVH analysis in electric vehicle powertrains." The Journal of Engineering, 2019.

[5] Ewins, D. J. Modal Testing: Theory, Practice and Application. Research Studies Press / Wiley, 2000.

[6] Allemang, R. J. "The Modal Assurance Criterion - Twenty Years of Use and Abuse." Sound and Vibration, 37(8), 14–23, 2003.

[7] Mottershead, J. E., and Friswell, M. I. "Model Updating in Structural Dynamics: A Survey." Journal of Sound and Vibration, 167(2), 347–375, 1993.

[8] Peeters, B., Van der Auweraer, H., Guillaume, P., and Leuridan, J. "The PolyMAX frequency-domain method: a new standard for modal parameter estimation?" Shock and Vibration, 11, 395–409, 2004.

[9] Oktav, A. "Experimental and numerical modal analysis of a passenger vehicle." International Journal of Vehicle Noise and Vibration, 12(4), 302–313, 2016.

[10] Zhao, Q. H., Chen, X. K., Wang, L., et al. “Simulation and experimental validation of powertrain mounting bracket design obtained from multi-objective topology optimization.” Advances in Mechanical Engineering, 2015.

[11] Li, X.-Q., Pang, J., Yang, L., Jia, X.-L., Lu, G., Yin, Z.-H., and Shangguan, W.-B. “Finite Element Model refinement of powertrain mount brackets for estimating natural frequencies.” Proceedings of the Institution of Mechanical Engineers, Part D: Journal of Automobile Engineering, 238(1), 2024.

[12] PCB Piezotronics. “Model 356A45 Triaxial ICP Accelerometer - product specifications.” Official manufacturer documentation, accessed May 2026.

[13] PCB Piezotronics. “Model 086C03 Instrumented Impact Hammer - product specifications.” Official manufacturer documentation, accessed May 2026.

[14] Siemens Digital Industries Software. “Simcenter SCADAS hardware - official product information.” Official manufacturer documentation, accessed May 2026.

[15] Siemens Digital Industries Software. “Simcenter Testlab Impact Testing - official documentation and support article.” Official manufacturer documentation, accessed May 2026.

[16] Internal lab report. “Experimental Modal Analysis and Model Updating of a Cantilever Beam.” Politecnico di Torino, draft report, 2025–2026.

[17] Internal lab report. “Dynamic modeling of electric powertrains and relative experimental validation - Experimental activity description.” Politecnico di Torino, draft report, 2026.